INPUT DESIGN AND DATA-DRIVEN APPROACHES BASED ON CONVEX OPTIMIZATION FOR FAULT DIAGNOSIS IN LINEAR SYSTEMS

INPUT DESIGN AND DATA-DRIVEN APPROACHES BASED ON CONVEX OPTIMIZATION FOR FAULT DIAGNOSIS IN LINEAR SYSTEMS

Dissertation

for the purpose of obtaining the degree of doctor
at Delft University of Technology
by the authority of the Rector Magnificus, prof. dr. ir. T.H.J.J. van der Hagen,
chair of the Board for Doctorates
to be defended publicly on
Thursday 18 April 2024 at 12:30 o'clock

by

Jacques NOOM

Master of Science in Systems and Control, Delft University of Technology, The Netherlands
born in Beverwijk, The Netherlands

This dissertation has been approved by the promotors.

Composition of the doctoral committee:

Rector Magnificus	chairperson
Prof. dr. ir. M. Verhaegen	Delft University of Technology, *promotor*
Dr. O.A. Soloviev	Delft University of Technology, *copromotor*
Dr. C.S. Smith	Delft University of Technology, *copromotor*

Independent members:

Prof. dr. T. Keviczky	Delft University of Technology
Dr. A. Mesbah	University of California, Berkeley
Dr. L. Travé-Massuyès	Université de Toulouse, France
Dr. ir. C.C. de Visser	Delft University of Technology
Prof. dr. ir. J.W. van Wingerden	Delft University of Technology, reserve member

CONTENTS

SUMMARY

The complexity of automated systems has grown considerably during the past decades. This convolutes the observation of possible faults in these systems. If not being revealed timely, such faults can lead to catastrophic failures. As a result, there is a continuous interest in sophisticated fault diagnosis techniques. Since it is generally desired to diagnose faults in the earliest possible stages, computational challenges are imposed on the algorithms. Whereas the field of fault diagnosis comprises of a large variety of techniques in various categories, these computational challenges appear to emerge wide-ranging.

At the same time, convex optimization has developed as a valuable tool to solve a large variety of mathematical problems with computational efficiency. This computational efficiency is achieved by exploiting favorable structures of the problem. Depending on the specific problem, these structures vary in difficulty to be recognized or arranged. Moreover, some problems lead to a convex optimization problem naturally, while other problems first need some kind of relaxation or sequential process in order to employ convex optimization.

This thesis explores how convex optimization can be utilized in order to solve fault diagnosis problems with computational efficiency. The state-of-the-art is studied for multiple computationally challenging categories of fault diagnosis: online input design approaches, diagnosis of many concurrent faults, and data-driven approaches. First, online input design approaches facilitate fault diagnosis by computing discriminating input sequences during system operation. Since the input is calculated in real-time those approaches allow only limited computational effort, whereas adequate input determination typically appears to be nontrivial. In this contribution it is shown that an established upper bound on the error probability for linear candidate models with Gaussian noise is concave in the most challenging discrimination conditions. This finding allows to use sequential convex programs for online determination of a discriminating input with low computational effort.

The second contribution in this thesis regards the cantilever dynamics in high-speed atomic force microscopy. Due to the oscillatory behavior above the scrutinized sample, the cantilever typically has intermittent physical contact with the sample. This leads to a large number of (dynamically dependent) impulsive faults. Instead of performing an intractable explicit examination of all (combinations of) hypotheses, this contribution applies sparse estimation as a convex optimization method in order to diagnose these concurrent faults. In a simulation study, the resulting effect on the sample height reconstruction is discernible both qualitatively and quantitatively with respect to the conventional approach to sample height reconstruction in atomic force microscopy.

The third contribution introduces a novel problem formulation for model-free data-driven fault diagnosis. Instead of separate time periods for system identification and fault diagnosis in typical data-driven approaches, model-free data-driven fault diagnosis

aims for the simultaneous system identification and fault diagnosis from one single data set. Whereas this is originally a non-convex bilinear problem, a proposed solution reformulates it as a convex optimization problem using a so-called lifting technique. Furthermore, online evaluation of this optimization problem is facilitated by a developed recursive implementation. The proposed methodology is tested both on simulation data and real-life flight test data.

By demonstrating the potential of convex optimization to a deliberate selection of fault diagnosis problems, this thesis serves as a source of inspiration for solving a wider variety of fault diagnosis problems efficiently. Furthermore, various elements related to convex optimization and its recursive implementation presented in this thesis have additional relevance to the general field of control science beyond fault diagnosis. Future applications of the presented methodology can arise for instance in the data-driven control in the presence of disturbances, or recursive blind deconvolution of real-time image sequences.

SAMENVATTING

Gedurende de laatste decennia worden geautomatiseerde systemen aanzienlijk geavanceerder. Dat bemoeilijkt het waarnemen van mogelijke fouten in deze systemen. Zulke fouten kunnen op den duur catastrofale gevolgen hebben. Daarom is er een aanhoudende interesse in hoogstaande technieken voor foutdiagnose. Aangezien het over het algemeen wenselijk is om fouten zo vroeg mogelijk te herkennen, zijn er rekenkundige uitdagingen voor de algoritmen. Hoewel het veld van foutdiagnose een verscheidenheid aan technieken in diverse categorieën kent, lijken de rekenkundige uitdagingen breed voor te komen.

Tegelijkertijd heeft convexe optimalisatie zich ontwikkeld als een nuttige tool om een breed scala aan wiskundige problemen op te lossen met rekenkundige efficiëntie. Deze efficiëntie wordt behaald door middel van het benutten van gunstige probleemstructuren. Afhankelijk per specifiek probleem is het meer of minder moeilijk om de structuur te herkennen of te vormen. Sommige problemen leiden natuurlijkerwijs tot een convex optimalisatieprobleem, terwijl andere problemen een vorm van relaxatie of sequentiële werkwijze vereisen om te profiteren van convexe optimalisatie.

Dit proefschrift verkent hoe convexe optimalisatie toegepast kan worden om foutdiagnoseproblemen op te lossen met rekenkundige efficiëntie. De state-of-the-art is bestudeerd voor meerdere rekenkundig uitdagende categorieën voor foutdiagnose: werkwijzen voor online bepaling van de systeeminput, diagnose van meerdere van elkaar afhankelijke fouten, en datagedreven methoden. Om te beginnen, werkwijzen voor online bepaling van de systeeminput faciliteren foutdiagnose door middel van het berekenen van uiteendrijvende inputreeksen tijdens de systeemoperatie. Omdat de input in realtime berekend moet worden, is de toegestane rekenkundige inspanning begrensd, terwijl adequate inputbepaling niet triviaal is. In deze bijdrage wordt aangetoond dat een (al bestaande) bovengrens van de kans op onjuiste diagnose, voor lineaire kandidaatmodellen met Gaussische ruis concaaf is in de meest uitdagende omstandigheden voor discriminatie. Deze bevinding impliceert dat sequentiële convexe optimalisatie toegepast kan worden voor online bepaling van uiteendrijvende inputs met lage rekenkundige inspanning.

De tweede bijdrage in dit proefschrift heeft te maken met de dynamica van de sonde in hogesnelheids-atoomkrachtmicroscopie. Door het oscillerende gedrag van de sonde, maakt het onderbroken contact met het specimen. Dit leidt tot een groot aantal (dynamisch afhankelijke) impulsieve fouten. In plaats van het uitvoeren van een rekenkundig hardnekkige expliciete toetsing van alle (combinaties van) hypothesen, past deze bijdrage *sparse estimation* toe als een convexe optimalisatiemethode om deze fouten te diagnosticeren. In een simulatie is het resulterende effect op de hoogtereconstructie van het specimen kwalitatief en kwantitatief waarneembaar ten opzichte van de conventionele methode voor hoogtereconstructie in atoomkrachtmicroscopie.

De derde bijdrage introduceert een nieuwe probleemformulering voor modelvrije datagedreven foutdiagnose. In plaats van gescheiden tijdsperiodes voor systeemidentificatie en foutdiagnose in conventionele datagedreven methoden, richt modelvrije datagedreven foutdiagnose zich op gelijktijdige systeemidentificatie en foutdiagnose uit één dataset. Hoewel dit normaliter een niet-convex bilineair probleem is, wordt het met behulp van een zogenoemde *lifting*-techniek geherformuleerd naar een convex optimalisatieprobleem. Verder wordt online evaluatie van dit optimalisatieprobleem gefaciliteerd door een uitgewerkte recursieve implementatie. De voorgestelde methodologie is getest op zowel simulatiedata als in de praktijk gemeten vluchttestgegevens.

Door middel van het demonstreren van de potentie van convexe optimalisatie op een weloverwogen selectie van foutdiagnoseproblemen, dient dit proefschrift als inspiratiebron om een grotere variëteit van zulke problemen efficiënt op te lossen. Bovendien, diverse elementen gerelateerd aan convexe optimalisatie en de recursieve implementatie gepresenteerd in dit proefschrift hebben aanvullende relevantie in het algemene onderzoeksveld van regeltechniek dat verder gaat dan foutdiagnose. Toekomstige toepassingen van de gepresenteerde methodologie kunnen zich onder andere voordoen in datagedreven regeltechniek in de aanwezigheid van verstoringen, of recursieve blinde deconvolutie van realtime afbeeldingsequenties.

PREFACE

On this cold but sunny day I am in the stage of finalizing the dissertation. That is something I could not imagine a year ago. This achievement would not have been possible without the substantial support of the people around me.

I would like to thank Michel Verhaegen for generously sharing his affinity with control science and providing plentiful valuable feedback to my work. I am thankful to Oleg Soloviev for giving me the opportunity to do this research and for stimulating independence. I thank Carlas Smith for providing valuable background knowledge and references to the literature, as well as sharing his teaching experience. My appreciation also goes to Gerard Verbiest for the fruitful collaboration and for his remarkable approachability. In addition to the members already mentioned, all other members of the doctoral committee are commended for giving me the opportunity to defend my work.

The working days at the university were highly enjoyable with my office and floor mates Edoardo, Pascal, Yu-Chen, Roger, Léonore, Paul-Louis, Meenakshi, Coen, Hamed, Shahzeb, Maria, Sreeshma, Sander, Lars, Pieter, Shrinivas, Vinod and Thao. It has also been a pleasure to have lunch, drink coffee, travel and do fun activities with the many other colleagues and friends from DCSC (including the people from the second and third floor!). My further gratitude goes to the support team Erica, Sandra, Francy, Heleen, Marieke, Bo and Anna.

I profoundly thank Lynn, my parents and my sister for their invaluable support in the past, present and future. I would like to thank Oma Gretha for her genuine warmth and sincere interest. Furthermore, I am pleased to honor my late grandparents Oma Noom and Opa Nic. Finally, thank you to all of my dear friends with whom I greatly enjoyed life outside of the research environment, whether it was road cycling, playing music or just hanging around.

Jacques Noom
Delft, December 2023

1

INTRODUCTION

This chapter introduces the reader to the general concepts and categories of fault diagnosis. It also highlights the current challenges and the possible exploration directions in order to overcome these challenges and to extend the state-of-the-art. The final section identifies the directions that offer opportunities for a comprehensive study. Hereby it outlines the contributions of the remaining chapters in this dissertation.

1

On October 29, 2018, the Lion Air Flight 610 (JT610) crashed shortly after departing from Jakarta, Indonesia [1]. Only five months later, on March 10, 2019, a similar accident happened to the Ethiopian Airlines Flight 302 (ET302) after taking-off in Addis Ababa, Ethiopia. The tragedies, both involving Boeing 737 MAX aircraft, have claimed the lives of 346 people [1]. Journalists speculate as to whether the cause is incompetence of the engineers involved in the design of the aircraft, or ethical shortcomings of these engineers [2]. Moreover, the competition with Airbus raised financial pressure on Boeing to rapidly introduce a new aircraft with a competitive performance, but also a low price and minimal additional training requirements for pilots [3]. The competitive performance – in terms of fuel consumption and flight range – was achieved by introducing a larger engine in the design. The time for development, price and training requirements for pilots were minimized by making slight modifications to the existing frame design of the well-established Boeing 737, rather than designing an entirely new frame in order to fit the larger engines. As a side-effect of these slight modifications, the aircraft tended to pitch upwards under certain flying conditions [3]. A new software system was intended to prevent the aircraft from pitching upwards with an excessive angle of attack. However, the software was unable to automatically diagnose a fault in the sensor it was relying on, in order to avoid the failures of JT610 and ET302. The pilots were not informed about the existence of the new software system, hindering them from taking appropriate corrective actions in order to prevent the subsequent crashes.

A study on the ethical aspects related to the accidents concludes there "seem to be clear violations of engineering codes of ethics" [4]. Even though the engineers at Boeing were constrained by the financial concerns of their employer, they should have prioritized public safety and welfare. Besides the engineers, also the managers violated the generally accepted ethical standard of *informed consent*. Boeing had at least "an obligation to inform airlines and pilots of the significant design changes" [4], so that for instance the pilots would have been able to recognize malfunctioning of the software system.

Contemporary codes of ethics state (among other things) that engineers should be truthful about and critical toward their own and other's technical work. For example, the American Institute of Aeronautics and Astronautics (AIAA) prescribes engineers to "issue statements or present information in an objective and truthful manner, based on available data" [5]. The Institute of Electrical and Electronics Engineers (IEEE) further specifies the instruction by writing "to seek, accept, and offer honest criticism of technical work, to acknowledge and correct errors, to be honest and realistic in stating claims or estimates based on available data" [6]. In order to be able to be objective, to acknowledge errors and to correct those, engineers may opt to include automatic fault diagnosis algorithms in the design of a dynamical system. In the first place, a system should be designed such that the probability of (critical) faults is minimized. But whenever a fault occurs, it should be diagnosed in time in order to minimize the potentially disastrous consequences. Depending on the type of system and possible faults, the diagnostic results can be communicated to the system operators and/or to the engineers themselves. For example, if the pilots of the Boeing 737 MAX aircraft were properly informed about the new software

system, an error message to them during the flight could possibly have prevented the crashes. From a higher perspective, the data of preceding 737 MAX flights (e.g. [7]) may have contained information that could have increased the engineer's awareness of the vulnerabilities of the software system. A fault diagnosis algorithm can assist engineers and system operators in providing crucial information timely and accurately.

1.1. Fault diagnosis

Fault diagnosis is a well-established field within the science of control engineering. In the early survey from 1976, Willsky [8] mentioned that sophisticated computational approaches may be a good alternative to high levels of hardware redundancy, without substantially losing system reliability. Since then, the following key definitions in the field are developed. An overview of more definitions can be found in [9].

Definition 1.1 (Fault). *An unpermitted deviation of at least one characteristic property or parameter of the system from the acceptable/usual/standard condition.*

Definition 1.2 (Failure). *A permanent interruption of a system's ability to perform a required function under specified operating conditions.*

Definition 1.3 (Fault detection). *Determination of the faults present in a system and the time of detection.*

Definition 1.4 (Fault diagnosis). *Determination of the kind, size, location and time of detection of a fault. Follows fault detection.*

One or multiple faults can lead to a failure of the system. It is therefore important that the faults are detected and diagnosed correctly in time. The aim of fault detection is only to notice abnormal input/output behavior timely. Afterwards, the objective of fault diagnosis is to gain more information of the specific fault, so that appropriate action can be taken subsequently.

1.1.1. Model-based

More recent surveys [10, 11] categorize fault diagnosis approaches as model-based, signal-based or knowledge-based. These approaches use different sources of information, as illustrated in Figure 1.1. Model-based approaches utilize candidate models from physical principles composed by an expert. Such a candidate model can generally describe the system characteristics as

$$M^{[i]} : y = g^{[i]}(x, u, w) \tag{1.1}$$

with the candidate model $g^{[i]}(x, u, w)$ with state x, input u and noise w corresponding to hypothesis $M^{[i]}$, and output y. From these candidate models, the algorithm for fault diagnosis should select the correct model under which the system is operating.

One way to accomplish this is to use a deterministic method, in which the system output trajectory y can ultimately be linked to a single hypothesis $M^{[i]}$. This

1
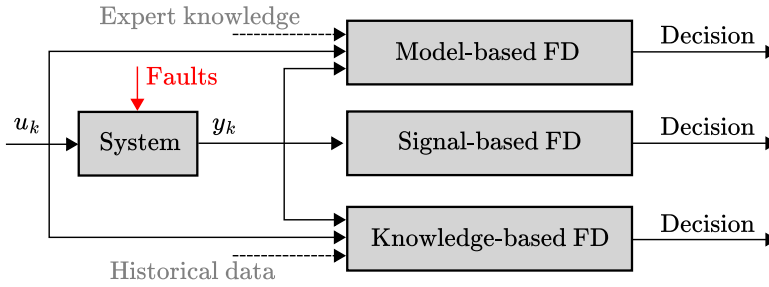
Figure 1.1: Model-based, signal-based and knowledge-based approaches use different sources of information in order to diagnose the fault(s).

generally requires the assumption that the noise contribution w is bounded, that is to say the limits of the model uncertainties are known. Accordingly, a deterministic approach to fault diagnosis accounts for the worst-case scenario and can usually only select a hypothesis when an output sequence is measured that is uniquely linked to that hypothesis.

Alternatively, a probabilistic method employs probabilities of the hypotheses in order to make a decision. A decision threshold can be set manually (e.g. [12, 13]) to compromise on the expected number of correct and incorrect decisions. In contrast to deterministic methods, probabilistic methods require knowledge of the probability distributions of the noise w rather than its limits. Moreover, the uncertainties may be unbounded if using a probabilistic approach. It is in general less conservative than a deterministic approach, since it regards the probabilities instead of unique system behavior.

1.1.2. SIGNAL-BASED

Signal-based approaches use only measured (output) signals to diagnose faults. A diagnostic decision is made based on the symptom analysis of these signals and prior knowledge of the normal system behavior [10]. These symptoms can for instance be observed in the time domain or in the frequency spectrum. A signal-based approach is specifically applicable to systems of which the input is unknown and unavailable for measurement. This dissertation however focuses on systems of which the input and output signals are accessible.

1.1.3. KNOWLEDGE-BASED

A knowledge-based approach to fault diagnosis does not use an explicit model composed by an expert. It rather uses past input/output data in order to predict future outputs corresponding to hypothesized fault conditions. If the measured output sequence correlates sufficiently to one of the predicted output sequences, then the corresponding fault is diagnosed. A knowledge-based approach typically requires large amounts of historical data for a training phase. That is why it is often referred to as *data-driven* [11, 14–17]. It is in general however not *model-free*, since

a model is implicitly built (or: identified) during the training phase.

1.1.4. Active methods

Whereas signal-based and knowledge-based approaches are generally passive, model-based approaches support active techniques [18, 19]. Active fault diagnosis applies an auxiliary input to the system in order to improve the discrimination performance. This auxiliary input may be designed either offline before executing the discrimination experiment, or online while taking into account the real-time measurements of the system. This is illustrated in Figure 1.2. Although online input design leads to better discrimination performance by using all possible real-time information, it is limited by its computational complexity. Nevertheless, the increasing capability of digital computers motivates contemporary research to enhance exploration of these online input design methods and how they can be conducted with computational efficiency.
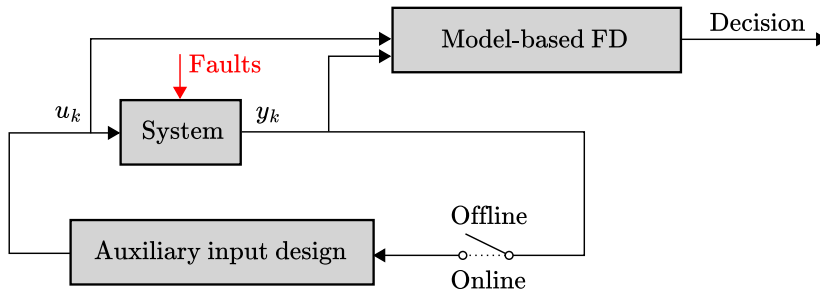
Figure 1.2: Active fault diagnosis. Offline approaches design a complete auxiliary input sequence before executing the discrimination experiment. Online approaches take into account real-time measurements while designing the auxiliary input.

1.2. Current challenges for fault diagnosis

As automated systems continually increase in complexity, approaches to fault diagnosis for these systems become more sophisticated. At the same time, it remains to be desired to diagnose faults in their earliest possible stages. Especially if the diagnosis should be performed during system operation, this imposes computational challenges on the fault diagnosis algorithms. The current main challenges are outlined as follows.

1.2.1. Computational complexity of online input design

The design of an input for diagnosing faults online involves a trade-off of three factors. First, the accuracy of diagnosis should be maximized while adhering to the imposed limits on the system input and output. That is to say, the ratio of correct diagnoses versus incorrect diagnoses should be maximized in order to establish a

1

reliable fault diagnosis procedure. Second, the fault should be diagnosed within a minimized number of measurements. This demand encourages diagnosis of the fault in the earliest possible stage. Since the auxiliary input should be calculated online, the third trade-off factor is fast computation, such that it can be applied to the system without delay. Regarding the first two trade-off factors imposing nonlinear optimization problem formulations, fast computation is currently a major challenge.

Both deterministic and probabilistic approaches to active fault diagnosis suffer from their computational complexities. Moreover, a deterministic problem setting imposes nonconvex constraints on the system input in order to induce a unique output sequence [20]. A probabilistic problem setting for active fault diagnosis computes an input sequence such that the probability of misdiagnosis is minimized. That involves the burdensome evaluation of multidimensional probability integrals, which becomes particularly problematic for real-time applications and/or large-scale systems.

1.2.2. CURSE OF DIMENSIONALITY FOR FAULT DIAGNOSIS

A *curse of dimensionality* generally refers to loss of computational tractability when the dimensions of the problem are increased. This applies to fault diagnosis in the case that faults can be active simultaneously. This is often the case, regarding dependence of faults in typical practical applications [21]. Suppose there are 30 possible faults of which up to three may be active simultaneously, then there are 4525 possible fault combinations [21]. Using a conventional fault diagnosis approach, for each individual fault combination a separate hypothesis is defined explicitly. In general, the number of hypotheses will grow with

$$N_H = \sum_{i=1}^{n_a} \frac{n_f!}{(n_f - n_a)! \, n_a!},$$

where n_f is the number of possible faults, and n_a the number of faults which can be active simultaneously. The explicit examination of each possible hypothesis will be intractable for moderate values of n_f and n_a already.

1.2.3. DATA AVAILABILITY FOR KNOWLEDGE-BASED APPROACHES

Knowledge-based approaches to fault diagnosis overcome the challenges of expert modeling of the system with possible faults. They are however known to require large amounts of historical data for a training phase. Moreover, it is preferred to obtain data for every (faulty) operating condition, of which this condition is exactly known. In practical applications these labeled data are not always available. For example, complex industrial systems typically involve substantial (financial) stakes, implying that it could be very expensive to run the system intentionally under faulty conditions solely for data acquisition. In addition, the exact condition of a complex system is often difficult (or even impossible) to examine a priori, complicating labeling of the data. Lastly, the system characteristics typically change slowly over time, for example due to wear (which is not necessarily a fault). With changed

1

system characteristics, the historical data may lose its relevance over time, so the expensive data acquisition needs to be carried out again.

1.3. Possible exploration directions

The current challenges for fault diagnosis outlined in previous section mainly involve high computational complexity and expensive data acquisition. The strategies presented in Sections 1.3.1 to 1.3.3 are possible solutions to the computational issues, whereas that in Section 1.3.4 is intended to relieve the data requirements.

1.3.1. Linearization

A well-known technique to facilitate computational tractability is to linearize a nonlinear problem around an operating point. A convenient representation is so-called continuous-time *state-space* [22]:

$$\begin{aligned} \dot{x}(t) &= Ax(t) + Bu(t) + w(t) \\ y(t) &= Cx(t) + Du(t) + v(t) \end{aligned}$$
(1.2)

with (A, B, C, D) the state-space matrices, $(u(t), x(t), y(t))$ the system input, state and output as function of time t, and $(w(t), v(t))$ the process and measurement noise. For example, continuous-time state-space models of various aircraft around various operating points are provided in [23]. To further increase the computational efficiency when implementing in a digital computer, it is straightforward to transform a continuous-time state-space model (1.2) to discrete-time [24]:

$$\begin{aligned} x(k+1) &= \Phi x(k) + \Gamma u(k) + w(k) \\ y(k) &= Cx(k) + Du(k) + v(k) \end{aligned}$$
(1.3)

where the matrices Φ and Γ are functions of the matrices A and B and of the sampling time[1]. Many fault diagnosis approaches in literature use linear(-ized) models [10, 18] in order to show the proof-of-principles of new developments. Nevertheless, active approaches are still a computational burden [18] and fault diagnosis approaches using linearized models still suffer from the curse of dimensionality explained in Section 1.2.2.

1.3.2. Probabilistic divergence measures

When using a probabilistic approach, one typically runs into computationally demanding evaluation of multidimensional integrals. Especially when using an active fault diagnosis approach, it pays off to use a divergence measure instead. A divergence measure compares two probability distributions in such a way that it outputs a positive scalar indicating how similar (or: different) these are. By exploiting noise characteristics of the system, it is often straightforward to compute

---

[1]Note that throughout literature and also this thesis, the discrete-time state transition matrix Φ and input matrix Γ are also indicated with A and B, despite the differences with their continuous-time counterparts.

1

the divergence of two distributions. Examples of divergence measures include the Kullback-Leibler divergence, the J-divergence and the Bhattacharyya coefficient [25, 26].

Whereas conventional divergence measures typically only consider two hypotheses, it appears to be easily extendable to multiple hypotheses using the sum of pairwise divergences [27]. Care should be taken not to oversimplify the problem and to lose a connection with the actual error probability. That could lead to unpredictable behavior of the fault diagnosis approach. For some divergence measures, such as the Bhattacharyya coefficient, a theoretical upper bound on the error probability does exist [27].

Even though divergence measures reduce the computational complexity considerably, it leads in general still to nonconvex problems for active approaches to fault diagnosis [18]. Further simplifications could decrease the computational effort to acceptable levels. However, such simplifications may degrade the diagnosis performance substantially. The trade-off between these aspects is currently still intractable.

1.3.3. SPARSE ESTIMATION METHODS

Recent stochastic methods use sparse regression in order to diagnose faults [21]. Sparse regression aims to estimate the few nonzero entries of an optimization variable [28]. Convex techniques (e.g. *lasso* [29]) facilitate computational efficiency. Particularly in the case of large numbers of possible (combinations of) active faults, sparse regression is suitable for diagnosis. Explicit hypothesis testing for each possible fault combination is circumvented, which would be a computational burden using conventional approaches.

1.3.4. UNSUPERVISED KNOWLEDGE-BASED APPROACHES

Knowledge-based approaches to fault diagnosis usually require labeled data to train on. Contrarily, unsupervised approaches are able to separate data autonomously without requiring labels to the training data. Often unsupervised knowledge-based approaches only train on nominal data [11], after which a fault is detected as being a deviation from the nominal data. It is however also possible to train on unlabeled data from multiple (possibly faulty) operating conditions [30].

Even though unsupervised approaches to knowledge-based fault diagnosis alleviate the requirement of labels, these retain the demand for large amounts of historical data. These data are utilized at least to build knowledge on the nominal operating conditions. In other words, a certain model of the system is identified prior to executing the diagnosis experiment. Collecting sufficient data for identifying this model may not always be feasible, for example due to unforeseen (possibly catastrophic) faults occurring in the initial operating period already. This enhances the interest for approaches in which the required amounts of historical data are reduced or even circumvented.

1.4. Dissertation contributions

The main challenges suppressing the development of fault diagnosis algorithms remain to be captured by their computational complexity. In order to reduce this computational complexity, this dissertation focuses on finding solutions based on convex optimization. With this in consideration, (most of) the methods presented in this thesis are developed for linear(-ized) discrete-time models. More specifically, the remaining chapters of the dissertation have the following contributions. These can be read independently of each other with the corresponding references listed after each respective chapter. This also entails the variables to be defined in each chapter separately. The interested reader can find the corresponding code in [31–34].

Chapter 2: Online input design for fault diagnosis

In this chapter we will develop a computationally attractive approach to design auxiliary inputs online in order to improve the discrimination performance. The Bhattacharyya coefficient is utilized as a probabilistic divergence measure preserving a theoretical upper bound on the error probability. As a result of its favorable properties especially in the most challenging discrimination conditions, the computational effort for optimizing the error bound remains low. The methodology is validated on both open-loop and feedback controlled systems. Besides, it is demonstrated on an object recognition application in which the input illumination pattern is controllable.

This chapter is based on the following publications:

- J. Noom, O. Soloviev, C. Smith, and M. Verhaegen. *Online input design for discrimination of linear models using concave minimization.* 2024. arXiv: 2401.05782 [eess.SY]

- J. Noom, O. Soloviev, C. Smith, and M. Verhaegen. "Closed-loop active object recognition with constrained illumination power". In: *Real-Time Image Processing and Deep Learning 2022.* Ed. by N. Kehtarnavaz and M. F. Carlsohn. Vol. 12102. International Society for Optics and Photonics. SPIE, 2022, pp. 9–14. DOI: 10.1117/12.2618750

Chapter 3: Sparse fault diagnosis for high-speed atomic force microscopy

High-speed atomic force microscopy typically employs an oscillating cantilever in order to determine the sample height over a certain area. The oscillating cantilever behavior results in intermittent contact with the sample, which can be regarded as faults with respect to the nominal free oscillation. Because of the typical high cantilever oscillation frequencies, large numbers of faults can occur. In this chapter we will study the implementation of a sparse estimation method for diagnosing these faults. Simulation experiments demonstrate the resulting effect on the sample height reconstruction.

This chapter is based on the following publication:

- J. Noom, C. Smith, G. J. Verbiest, A. J. Katan, O. Soloviev, and M. Verhaegen. "High-Speed Tapping Mode AFM Utilizing Recovery of Tip-Sample Interaction". In: *IEEE Transactions on Nanotechnology* 22 (2023), pp. 273–279. DOI: 10.1109/TNANO.2023.3284654

CHAPTER 4: ONLINE MODEL-FREE DATA-DRIVEN FAULT DIAGNOSIS

This chapter introduces a novel problem formulation for model-free data-driven fault diagnosis. Instead of dividing the training (or: identification) and diagnosis experiment in two separate steps, model-free data-driven fault diagnosis aims to both identify the system and diagnose the faults simultaneously. This circumvents the requirement of large amounts of historical data in state-of-the-art approaches to data-driven fault diagnosis. The proposed solution to the novel problem formulation uses convex optimization. The resulting optimization problem can be solved online using the introduced recursive implementation of a proximal algorithm.

This chapter is based on the following publications:

- J. Noom, O. Soloviev, and M. Verhaegen. "Proximal-based recursive implementation for model-free data-driven fault diagnosis". Accepted for publication in Automatica.

- J. Noom, O. Soloviev, and M. Verhaegen. "Data-driven fault diagnosis under sparseness assumption for LTI systems". In: *IFAC-PapersOnLine* 56.2 (2023), pp. 7722–7727. DOI: 10.1016/j.ifacol.2023.10.1176

CHAPTER 5: MODEL-FREE DATA-DRIVEN APPROACH TO DIAGNOSIS OF AIR DATA SENSOR FAULTS

The model-free data-driven fault diagnosis approach introduced in Chapter 4 is useful in situations where the system dynamics are unknown (precisely). This is a typical situation in the control of aircraft, in which the specific flight conditions alter the aircraft dynamics. The correct operation of air data sensors is critical to a safe flight. These sensors are however sensitive to faults due to icing, for instance. This chapter applies a novel model-free data-driven approach to diagnose these air data sensor faults without requiring knowledge of a model.

This chapter is based on the following publication:

- J. Noom, C. C. de Visser, N. S. Ramesh, and M. Verhaegen. "Simultaneously identifying the system dynamics and fault isolation for air data sensor failures: a convex approach". Accepted for presentation at IFAC Safe Process 2024.

REFERENCES

[1] Federal Aviation Administration (FAA). *Summary of the FAA's Review of the Boeing 737 MAX*. Nov. 2018. URL: https://www.faa.gov/sites/faa.gov/files/2022-08/737_RTS_Summary.pdf.

[2] G. Leopold. "Software won't fix Boeing's 'faulty' airframe". In: *EE|Times* (Mar. 2019). URL: https://www.eetimes.com/software-wont-fix-boeings-faulty-airframe/.

[3] D. Gelles, N. Kitroeff, J. Nicas, and R. R. Ruiz. "Boeing was 'go, go, go' to beat Airbus with the 737 MAX". In: *The New York Times* (Mar. 2019). URL: https://www.nytimes.com/2019/03/23/business/boeing-737-max-crash.html.

[4] J. Herkert, J. Borenstein, and K. Miller. "The Boeing 737 MAX: Lessons for Engineering Ethics". In: *Science and Engineering Ethics* 26.6 (July 2020), pp. 2957–2974. DOI: 10.1007/s11948-020-00252-y.

[5] American Institute of Aeronautics and Astronautics (AIAA). *Code of Ethics*. May 2013. URL: https://www.aiaa.org/about/Governance/Code-of-Ethics.

[6] Institute of Electrical and Electronics Engineers (IEEE). *IEEE Code of Ethics*. Accessed on 12 Oct. 2023. URL: https://www.ieee.org/about/corporate/governance/p7-8.html.

[7] M. Jamaluddin, H. Regan, and J. Guy. "Extra pilot averted disaster on previous Boeing 737 Max 8 flight - report". In: *CNN* (Mar. 2019). URL: https://edition.cnn.com/2019/03/20/asia/lion-air-third-pilot-intl/index.html.

[8] A. S. Willsky. "A survey of design methods for failure detection in dynamic systems". In: *Automatica* 12.6 (1976), pp. 601–611. ISSN: 0005-1098. DOI: 10.1016/0005-1098(76)90041-8.

[9] R. Isermann and P. Ballé. "Trends in the application of model-based fault detection and diagnosis of technical processes". In: *Control Engineering Practice* 5.5 (1997), pp. 709–719. ISSN: 0967-6661. DOI: 10.1016/S0967-0661(97)00053-1.

[10] Z. Gao, C. Cecati, and S. X. Ding. "A survey of fault diagnosis and fault-tolerant techniques – Part I: Fault diagnosis with model-based and signal-based approaches". In: *IEEE Transactions on Industrial Electronics* 62.6 (2015), pp. 3757–3767. DOI: 10.1109/TIE.2015.2417501.

1

[11]   Z. Gao, C. Cecati, and S. X. Ding. "A survey of fault diagnosis and fault-tolerant techniques – Part II: Fault diagnosis with knowledge-based and hybrid/active approaches". In: *IEEE Transactions on Industrial Electronics* 62.6 (2015), pp. 3768–3774. DOI: 10.1109/TIE.2015.2419013.

[12]   S. M. Kay. *Fundamentals of Statistical Signal Processing: Detection Theory.* Upper Saddle River, New Jersey: Prentice-Hall, Inc., 1998. ISBN: 978-0135041352.

[13]   Y. Benjamini and Y. Hochberg. "Controlling the False Discovery Rate: A Practical and Powerful Approach to Multiple Testing". In: *Journal of the Royal Statistical Society. Series B (Methodological)* 57.1 (1995), pp. 289–300. DOI: 10.1111/j.2517-6161.1995.tb02031.x.

[14]   X. Dai and Z. Gao. "From Model, Signal to Knowledge: A Data-Driven Perspective of Fault Detection and Diagnosis". In: *IEEE Transactions on Industrial Informatics* 9.4 (2013), pp. 2226–2238. DOI: 10.1109/TII.2013.2243743.

[15]   S. Yin, S. X. Ding, X. Xie, and H. Luo. "A Review on Basic Data-Driven Approaches for Industrial Process Monitoring". In: *IEEE Transactions on Industrial Electronics* 61.11 (2014), pp. 6418–6428. DOI: 10.1109/TIE.2014.2301773.

[16]   S. X. Ding. *Data-driven design of fault diagnosis and fault-tolerant control systems.* Springer-Verlag London, 2014. DOI: 10.1007/978-1-4471-6410-4.

[17]   S. Simani. "Data-Driven Methods for Fault Diagnosis". In: *Diagnosis and Fault-tolerant Control 1: Data-driven and Model-based Fault Diagnosis Techniques.* Ed. by V. Puig and S. Simani. ISTE Ltd and John Wiley & Sons, Inc., 2021. Chap. 5, pp. 131–195. DOI: 10.1002/9781119882329.ch5.

[18]   T. A. N. Heirung and A. Mesbah. "Input design for active fault diagnosis". In: *Annual Reviews in Control* 47 (2019), pp. 35–50. DOI: 10.1016/j.arcontrol.2019.03.002.

[19]   I. Punčochář and J. Škach. "A Survey of Active Fault Diagnosis Methods". In: *IFAC-PapersOnLine* 51.24 (2018), pp. 1091–1098. DOI: 10.1016/j.ifacol.2018.09.726.

[20]   D. M. Raimondo, G. Roberto Marseglia, R. D. Braatz, and J. K. Scott. "Closed-loop input design for guaranteed fault diagnosis using set-valued observers". In: *Automatica* 74 (2016), pp. 107–117. DOI: 10.1016/j.automatica.2016.07.033.

[21]   Q. Zhang. "Dynamic System Fault Diagnosis Under Sparseness Assumption". In: *IEEE Transactions on Signal Processing* 69 (2021), pp. 2499–2508. DOI: 10.1109/TSP.2021.3072004.

[22]   B. Friedland. *Control system design: An introduction to state-space methods.* Mineola, NY, USA: Dover Publications, 2005. ISBN: 978-0486442785.

[23]   A. E. J. Bryson. *Control of Spacecraft and Aircraft.* Princeton University Press, 1994. ISBN: 978-0691087825.

[24] K. J. Åström and B. Wittenmark. *Computer-controlled systems: Theory and design*. 3rd ed. Mineola, NY, USA: Dover Publications, 2011. ISBN: 978-0486486130.

[25] L. Pardo. *Statistical Inference Based on Divergence Measures*. Statistics: A Series of Textbooks and Monographs. Boca Raton, FL, USA: CRC Press, 2006. ISBN: 9781420034813.

[26] J. Lin. "Divergence Measures Based on the Shannon Entropy". In: *IEEE Transactions on Information Theory* 37.1 (1991), pp. 145–151. DOI: 10.1109/18.61115.

[27] D. E. Boekee and J. C. van der Lubbe. "Some aspects of error bounds in feature selection". In: *Pattern Recognition* 11.5 (1979), pp. 353–360. DOI: 10.1016/0031-3203(79)90047-5.

[28] T. Hastie, R. Tibshirani, and M. Wainwright. *Statistical Learning with Sparsity*. Chapman and Hall/CRC, May 2015. DOI: 10.1201/b18401.

[29] R. Tibshirani. "Regression Shrinkage and Selection Via the Lasso". In: *Journal of the Royal Statistical Society: Series B (Methodological)* 58.1 (1996), pp. 267–288. DOI: 10.1111/j.2517-6161.1996.tb02080.x.

[30] Y. Lei, F. Jia, J. Lin, S. Xing, and S. X. Ding. "An Intelligent Fault Diagnosis Method Using Unsupervised Feature Learning Towards Mechanical Big Data". In: *IEEE Transactions on Industrial Electronics* 63.5 (2016), pp. 3137–3147. DOI: 10.1109/TIE.2016.2519325.

[31] J. Noom. *Matlab code for online input design for discrimination of linear models using concave minimisation*. 2024. DOI: 10.5281/zenodo.6642321.

[32] J. Noom. *Matlab code for HS-AFM utilizing recovery of tip-sample interaction*. 2024. DOI: 10.5281/zenodo.10454091.

[33] J. Noom. *Matlab code for model-free data-driven fault diagnosis*. 2024. DOI: 10.5281/zenodo.10454000.

[34] J. Noom. *Matlab code for simultaneous identification of the system dynamics and fault isolation for air data sensor failures*. 2024. DOI: 10.5281/zenodo.10454343.

[35] J. Noom, O. Soloviev, C. Smith, and M. Verhaegen. *Online input design for discrimination of linear models using concave minimization*. 2024. arXiv: 2401.05782 [eess.SY].

[36] J. Noom, O. Soloviev, C. Smith, and M. Verhaegen. "Closed-loop active object recognition with constrained illumination power". In: *Real-Time Image Processing and Deep Learning 2022*. Ed. by N. Kehtarnavaz and M. F. Carlsohn. Vol. 12102. International Society for Optics and Photonics. SPIE, 2022, pp. 9–14. DOI: 10.1117/12.2618750.

[37] J. Noom, C. Smith, G. J. Verbiest, A. J. Katan, O. Soloviev, and M. Verhaegen. "High-Speed Tapping Mode AFM Utilizing Recovery of Tip-Sample Interaction". In: *IEEE Transactions on Nanotechnology* 22 (2023), pp. 273–279. DOI: 10.1109/TNANO.2023.3284654.

1

[38]   J. Noom, O. Soloviev, and M. Verhaegen. "Proximal-based recursive implemen-
       tation for model-free data-driven fault diagnosis". Accepted for publication in
       Automatica.

[39]   J. Noom, O. Soloviev, and M. Verhaegen. "Data-driven fault diagnosis under
       sparseness assumption for LTI systems". In: *IFAC-PapersOnLine* 56.2 (2023),
       pp. 7722–7727. DOI: 10.1016/j.ifacol.2023.10.1176.

[40]   J. Noom, C. C. de Visser, N. S. Ramesh, and M. Verhaegen. "Simultaneously
       identifying the system dynamics and fault isolation for air data sensor failures:
       a convex approach". Accepted for presentation at IFAC Safe Process 2024.

2

ONLINE INPUT DESIGN FOR FAULT DIAGNOSIS

Stochastic Closed-Loop Active Fault Diagnosis (CLAFD) aims to select the input sequentially in order to improve the discrimination of different models by minimizing the predicted error probability. As computation of these error probabilities encompasses the evaluation of multidimensional probability integrals, relaxation methods are of interest. This chapter presents a new method that allows to make an improved trade-off between three factors – namely maximized accuracy of diagnosis, minimized number of consecutive measurements to achieve that accuracy, and minimized computational effort per time step – with respect to the state-of-the-art. It relies on minimizing an upper bound on the error probability, which is in the case of linear models with Gaussian noise proven to be concave in the most challenging discrimination conditions. A simulation study is conducted both for open-loop and feedback controlled candidate models. The results demonstrate the favorable trade-off using the new contributions in this chapter.

2.1. INTRODUCTION

Fault diagnosis is crucial for automation. Widespread applications rise from recognizing faults in dynamical systems [4] to automatic classification of images [2, 5]. Moreover, Industry 4.0 aims at fully automated, smart factories where (among other things) ample data are turned into automatic actions and decisions. The motivation of such actions and decisions lies in model diagnosis. It is therefore critical that the diagnosis is efficient and reliable.

Passive approaches of fault diagnosis have the potential to overlook faults, as complex or feedback-controlled systems may generate nominal input-output data while not being fault-free [6]. Active fault diagnosis overcomes the shortcomings of passive diagnosis by applying an input designed such that complex models can still be discriminated. Online computation of the discriminating inputs further increases the efficiency by considering most recent measurements. Such closed-loop implementations receive increased interest for their decreased conservatism and accelerated diagnosis, yet are not widespread use in automation [6].

Although the idea of Closed-Loop Active Fault Diagnosis (CLAFD) exists for several decades in static [7, 8] and dynamical systems [9], the developments were held back due to its computational challenges [6]. Moreover, the trade-off consists of three factors. First, the accuracy of diagnosis should be maximized. Second, the system should be diagnosed within a minimized number of consecutive measurements. Third, the inputs should be calculated fast enough so they can be applied to the system without delay. This implication between performance (first two factors) and computational efficiency (third factor) is still a major bottleneck.

Existing efforts can be separated in deterministic and stochastic approaches [10], which are both computationally challenging. Assuming bounded uncertainties, a deterministic approach facilitates guaranteed diagnosis of the correct model [e.g. 11]. This problem is computationally challenging due to the nonconvex constraints on the input such that the system output is exclusive [12]. Alternatively, stochastic approaches assume known Probability Density Functions (PDFs) for unbounded uncertainties. Instead of anticipating the worst-case scenario for guaranteed diagnosis, the goal of stochastic approaches is to minimize the probability of misdiagnosis. This is computationally challenging because of the (online) evaluation of multidimensional probability integrals to determine the error probability. An illustration of the enormous computational challenge here is reported in [13], where even when restricting the input to a small discrete set of three elements and three second order candidate models, the computational time for determining the input policy was 7.5 hours [13]. Yet, stochastic approaches are generally less intrusive than deterministic approaches [14]. Besides, it is in practice often difficult to define explicit bounds on signals, which makes it more natural to formulate CLAFD as a stochastic optimization problem [15, 16].

To overcome the tremendous computational burden of stochastic approaches, a widely accepted solution is to optimize an upper bound, such as the sum of weighted Bhattacharyya coefficients [17]. Using sequential quadratic programming and restricting to open-loop (batch-wise) input determination, this has been studied in [18]. Due to the remaining high computational complexity, closed-loop

(receding-horizon) implementation is still unattractive. [16] restricted to polytopic constraints on the input in an attempt to implement it efficiently in closed-loop. This approach however could not guarantee a solution that is optimal with respect to the upper bound.

As an alternative for overcoming the real-time bottleneck, a further simplification is proposed in [15], where just the convex part of the Bhattacharyya coefficient is employed. The so-called Bhattacharyya *distance* was maximized in an attempt to discriminate the candidate models. Although this resulted in a fast computational solution, serious drawbacks are introduced. First, the function used in [15] is by no means an approximation to the upper bound on the error probability. Consequently, there exist conditions where the performance degrades substantially, such as the case of multiple groups of close candidate models. Second, [15] only considered polytopic constraints on the input in order to determine the maximum of the simplified function.

The main contribution of this chapter is as follows. First, for linear systems with Gaussian disturbances it is shown that the upper bound on the error probability is concave in a subdomain of the input space. That subdomain is characterized by the interesting case when discrimination between candidate models is challenging in terms of noise and proximity of the candidate models. Second, a real-time online check for being in this subdomain is formulated both for the case of a polytopic and quadratic constraint set. Third, we propose to solve the minimization problem using Disciplined Convex-Concave Programming (DCCP) [19], extending the ability to implement the closed-loop diagnosis procedure to a broad spectrum of convex constraints on the input. Altogether, this overcomes the two main drawbacks of the approach in [15]. For further speedup of the computations without unnecessarily sacrificing the performance, a quadratic Taylor approximation of the upper bound on the error probability is proposed. The differences of the proposed approaches with that in [15] are verified in a first Monte-Carlo simulation, after which a second Monte-Carlo simulation aims at comparing the performances of the approaches extended by DCCP. The final simulation shows the applicability of the proposed approaches to feedback controlled systems.

The chapter is organized as follows. First, the stochastic diagnosis problem is defined in Sect. 2.2. Then, the practical implementation is presented in Sect. 2.3, together with the derivation of domain of concavity and the quadratic Taylor approximation. Sect. 2.4 presents simulation results for the proposed closed-loop methods, along with the state-of-the-art closed-loop method based on Bhattacharyya distances and an open-loop approach. Lastly, Sect. 2.6 states the conclusions.

2.2. PROBLEM FORMULATION

2.2.1. NOTATION

In consistency with [15, 16], we will use the following notation. The expression $x|y$ denotes the random variable x conditioned on y, $\hat{x}_{k|k-n}$ is the estimate of x_k based on knowledge up until time step $k-n$, the notation $x_{k:k+n} = \begin{bmatrix} x_k^\top & x_{k+1}^\top & \dots & x_{k+n}^\top \end{bmatrix}^\top$, and we define boldface $\mathbf{x}_k = x_{k+1:k+N}$ with N the horizon length. The notation

$P_k(\text{event}) = \mathbb{P}(\text{event at time step } k)$ with $\mathbb{P}$ the probability operator, and the expectation operator $\mathbb{E}[\cdot]$ works on the stochastic output data y_k.

2.2.2. BAYESIAN FORMULATION

Regard the linear candidate models of a system:

$$M^{[i]} : \begin{cases} x_{k+1} & = A^{[i]} x_k + B^{[i]} u_k + w_k \\ y_k & = C^{[i]} x_k + v_k \end{cases} \tag{2.1}$$

with $i = \{0, 1, \ldots, n_m - 1\}$ the model indicator, $A^{[i]}, B^{[i]}, C^{[i]}$ the state space matrices and $x_k \in \mathbb{R}^{n_x}$, $u_k \in \mathbb{R}^{n_u}$, $y_k \in \mathbb{R}^{n_y}$ the state, input and output. Given the joint covariance matrix of the process noise w_k and measurement noise v_k

$$\mathbb{E}\left[\begin{bmatrix} v_k \\ w_k \end{bmatrix} \begin{bmatrix} v_\ell^\top & w_\ell^\top \end{bmatrix}\right] = \begin{cases} \begin{bmatrix} R & S^\top \\ S & Q \end{bmatrix} & \text{if } k = \ell, \\ 0 & \text{otherwise}, \end{cases} \tag{2.2}$$

the optimal state prediction $\hat{x}_{k+1|k}^{[i]}$ can be obtained together with its corresponding covariance matrix $\Xi_{k+1|k}^{[i]}$ using the Kalman filter as described in for instance [20]. Stability of the candidate models is not required. Nevertheless, feedback controlled systems can be captured in (2.1) and (2.2) as described in Appendix 2.A.

The hypothesis probabilities evolve according to the Bayesian update rule

$$\begin{aligned} P_{k+N}&\left(M^{[i]} \big| P_k(M^{[i]}), \hat{x}_{k+1|k}^{[0:n_m-1]}, \mathbf{y}_k, \mathbf{u}_k\right) \\ &= \frac{p\left(\mathbf{y}_k \big| M^{[i]}, \hat{x}_{k+1|k}^{[i]}, \mathbf{u}_k\right) P_k(M^{[i]})}{p\left(\mathbf{y}_k \big| \hat{x}_{k+1|k}^{[0:n_m-1]}, \mathbf{u}_k\right)}, \end{aligned} \tag{2.3}$$

where $p\left(\mathbf{y}_k \big| M^{[i]}, \hat{x}_{k+1|k}^{[i]}, \mathbf{u}_k\right) \in \mathbb{R}_+$ is the probability density function (PDF) of output $\mathbf{y}_k$, conditioned on hypothesis $M^{[i]}$, state estimate $\hat{x}_{k+1|k}^{[i]}$ and input $\mathbf{u}_k$. The initial conditions $P_0(M^{[i]})$ can be set to any prior probabilities. Observe that in this notation the left-hand side of (2.3) is conditioned on another probability, which is convenient for the reason that the model probabilities $P_k(M^{[0:n_m-1]})$ combined with system state estimates $\hat{x}_{k+1|k}^{[0:n_m-1]}$ fully describe the so-called belief state of the partially observable Markov decision process.

If one chooses the most likely model

$$M^{[i]} : i = \arg\max_i \left(P_k(M^{[i]})\right) \tag{2.4}$$

based on all knowledge up until time step k, then the probability of misdiagnosis would be

$$P_k\left(\text{error} \big| P_k(M^{[0:n_m-1]})\right) = 1 - \max_i \left(P_k(M^{[i]})\right). \tag{2.5}$$

The *future* (unknown) probability of misdiagnosis after next measurements $\mathbf{y}_k$ also depends on future inputs and outputs:

$$
\begin{aligned}
&P_{k+N}\big(\text{error}\big|P_{k+N}(M^{[0:n_m-1]})\big)\\
&= P_{k+N}\Big(\text{error}\big|P_k(M^{[0:n_m-1]}),\hat{x}_{k+1|k}^{[0:n_m-1]},\mathbf{y}_k,\mathbf{u}_k\Big)\\
&= 1-\max_i\Big(P_{k+N}\Big(M^{[i]}\big|P_k(M^{[i]}),\hat{x}_{k+1|k}^{[0:n_m-1]},\mathbf{y}_k,\mathbf{u}_k\Big)\Big).
\end{aligned}
\tag{2.6}
$$

Obviously, it is desirable to minimize this future error probability. For that purpose, the stochastic problem of CLAFD is based on the expected value of the error probability. Besides, one could imagine that the optimal input sequence for minimizing the error probability changes when more measurements become available. This is covered in the general stochastic formulation of the CLAFD problem, as presented in next section.

2.2.3. INFINITE HORIZON STOCHASTIC CONTROL PROBLEM

In accordance with [21], the stochastic control problem of CLAFD is generally formulated as

$$
\begin{aligned}
\min_{\pi}\ &\lim_{N\to\infty}\sum_{k=0}^{N-1}\mathbb{E}\Big[P_k\big(\text{error}\big|s_k\big)\Big|s_0\Big]\\
\text{s.t.}\ &\pi\in\Pi\\
&s_{k+1}=f[s_k,\mu_k(s_k),\mathbf{w}_k].
\end{aligned}
\tag{2.7}
$$

Here, the input policy $\pi=(\mu_0,\dots,\mu_{N-1})$ defines the input with the functions

$$
u_k=\mu_k(s_k),
$$

constrained to the set Π. The function $f[s_k,\mu_k(s_k),\mathbf{w}_k]$ describes the system dynamics as function of state s_k, input function $\mu_k(s_k)$ and $\mathbf{w}_k$ the stochastic disturbance. Similarly to [13], the hyperstate s_k should consist of the state estimates for each candidate model $\hat{x}_{k+1|k}^{[i]}$ and the model probabilities $P_k(M^{[i]})$. The variable $\mathbf{w}_k$ consists of the noise contributions w_k and v_k.

The expected value of the error probability in (2.7) is also known as the *risk* in a Bayes classifier [see e.g. 22]. When considering for the case in this chapter that the estimated states and covariance matrices are available from (2.1), the expected value acts as a predictor of the error probability in (2.6). In other words,

$$
\begin{aligned}
&\hat{P}_{k+N|k}\big(\text{error}\big|\mathbf{u}_k\big)\\
&= \mathbb{E}\Big[P_{k+N}\Big(\text{error}\big|P_k(M^{[0:n_m-1]}),\hat{x}_{k+1|k}^{[0:n_m-1]},\mathbf{y}_k,\mathbf{u}_k\Big)\Big]\\
&= P_{k+N}\Big(\text{error}\big|P_k(M^{[0:n_m-1]}),\hat{x}_{k+1|k}^{[0:n_m-1]},\mathbf{u}_k\Big).
\end{aligned}
\tag{2.8}
$$

Note that all sides of this equation are independent of the future system outputs $\mathbf{y}_k$, and therefore it is a deterministic function of $\mathbf{u}_k$ only.

2

2.3. METHODOLOGY

2.3.1. MODEL PREDICTIVE CONTROL

A generally accepted strategy for solving an infinite horizon stochastic control problem is to make use of a receding horizon approach, most commonly known as Model Predictive Control (MPC) [23]. This technique solves a finite horizon control problem each time step, and applies only the first input to the system. The N-step receding-horizon approximation of (2.7) is

$$\mathbf{u}_k^* = \arg\min_{\mathbf{u}_k \in \mathcal{U}} \sum_{\ell=k+2}^{k+N} \hat{P}_{\ell|k}\left(\text{error}\middle|u_{k+1:\ell-1}\right) \tag{2.9}$$

with $\mathcal{U}$ the constraint set on vectorised inputs $\mathbf{u}_k$.

2.3.2. BOUND ON PREDICTED ERROR PROBABILITY

Since the prediction of the error probability requires large computational effort, a divergence measure will be used instead. The Bhattacharyya coefficient is a symmetric measure which provides an upper bound on the predicted error probability [17]:

$$\hat{P}_{k+N|k}\left(\text{error}\middle|\mathbf{u}_k\right) \leq \sum_i \sum_{j>i} \sqrt{P_k(M^{[i]})P_k(M^{[j]})}\,\mathfrak{B}^{[ij]}(\mathbf{u}_k) \tag{2.10}$$

with the Bhattacharyya coefficient in case of Gaussian process and measurement noise

$$\mathfrak{B}^{[ij]}(\mathbf{u}_k) = \exp(-d^{[ij]}(\mathbf{u}_k)). \tag{2.11}$$

The Bhattacharyya distance

$$d^{[ij]}(\mathbf{u}_k) = \mathbf{u}_k^\top H^{[ij]}\mathbf{u}_k + \mathbf{u}_k^\top c^{[ij]} + h^{[ij]} \tag{2.12}$$

is a convex quadratic function where [15]:

$$\begin{aligned}
H^{[ij]} &= \frac{1}{4}(\Gamma^{[ij]})^\top (\Omega^{[ij]})^{-1}\Gamma^{[ij]} \\
c^{[ij]} &= \frac{1}{2}(\Gamma^{[ij]})^\top (\Omega^{[ij]})^{-1}\zeta^{[ij]}
\end{aligned} \tag{2.13}$$

and

$$\begin{aligned}
\Omega^{[ij]} &= \Sigma_{k|k}^{[i]} + \Sigma_{k|k}^{[j]} \\
\Gamma^{[ij]} &= \mathbf{C}^{[i]}\mathcal{T}_{A^{[i]}}\mathbf{B}^{[i]} - \mathbf{C}^{[j]}\mathcal{T}_{A^{[j]}}\mathbf{B}^{[j]} \\
\zeta^{[ij]} &= \mathbf{C}^{[i]}\mathbf{A}^{[i]}\hat{x}_{k+1|k}^{[i]} - \mathbf{C}^{[j]}\mathbf{A}^{[j]}\hat{x}_{k+1|k}^{[j]}
\end{aligned} \tag{2.14}$$

with the matrices $\mathbf{A}^{[i]}, \mathbf{B}^{[i]}, \mathbf{C}^{[i]}$ and Toeplitz matrix $\mathcal{T}_{A^{[i]}}$ constructed from the state-space matrices in (2.1), and $\Sigma_{k|k}^{[i]}$ are the covariance matrices of the estimates of the output $\hat{\mathbf{y}}_{k|k}^{[i]}$. The full definitions together with that of $h^{[ij]}$ are given in Appendix 2.B.

Given the bound in (2.10), the relaxed MPC problem reads

$$\mathbf{u}_k^* = \underset{\mathbf{u}_k \in \mathcal{U}}{\arg\min} \sum_{\ell=k+2}^{k+N} \sum_i \sum_{j>i} \sqrt{P_k(M^{[i]}) P_k(M^{[j]})} \mathfrak{B}^{[ij]}(u_{k+1:\ell-1}). \tag{2.15}$$

Since the objective function (2.15) is still non-convex, efforts have been made to simplify it further. The approach in [16] aims to solve

$$\mathbf{u}_k^* = \arg\min_{\mathbf{u}_k \in \mathcal{U}} \sum_i \sum_{j>i} \sqrt{P_k(M^{[i]}) P_k(M^{[j]})} \mathfrak{B}^{[ij]}(\mathbf{u}_k) \tag{2.16}$$

instead, using only the error bound for time step $k+N$. Furthermore, [15] simplifies problem (2.16) to

$$\mathbf{u}_k^* = \arg\min_{\mathbf{u}_k \in \mathcal{U}} \sum_i \sum_{j>i} -d^{[ij]}(\mathbf{u}_k) \tag{2.17}$$

in which only the Bhattacharyya distances $d^{[ij]}(\mathbf{u}_k)$ are considered. Its performance is demonstrated on a problem with a polytopic constraint set, such that the minimum of this concave function lies at one of the vertices of this set. Although the computational effort is relatively small, the solution can differ significantly from the optimum of (2.16). To improve the optimization outcome, [16] proposes to evaluate the objective function in (2.16) only at the vertices of the constraint set. Still, the global optimum of (2.16) is not guaranteed using this approach.

The current chapter follows the observation that (2.15) is in closed-loop diagnosis – with challenging discrimination conditions – often concave within the given constraint set. The next sections elaborate on verification of concavity and show how this concave problem can be minimized for polytopic constraints and energy constraints. Besides, Sect. 2.3.5 presents an improved quadratic approximation w.r.t. (2.17), which can be used if regular concave minimization is still too demanding with respect to quadratic concave minimization.

2.3.3. DOMAIN OF CONCAVITY OF THE BHATTACHARYYA COEFFICIENT

Note that in case of Gaussian process and measurement noise, the Bhattacharyya coefficient is a Gaussian function

$$\mathfrak{B}(\mathbf{u}_k) = \exp\left(-\mathbf{u}_k^\top H \mathbf{u}_k - c^\top \mathbf{u}_k - h\right) \tag{2.18}$$

with H a positive semi-definite, symmetric matrix (the indices ij are omitted for clarity) which can be partitioned using the singular value decomposition (SVD)

$$H = \begin{bmatrix} U_1 & U_2 \end{bmatrix} \begin{bmatrix} \Lambda_1 & 0 \\ 0 & 0 \end{bmatrix} \begin{bmatrix} U_1^\top \\ U_2^\top \end{bmatrix}. \tag{2.19}$$

The domain where the Bhattacharyya coefficient is concave, is provided in the following lemma.

2

Lemma 2.1 (Domain of concavity of a multivariate Gaussian)**.** *Expression* (2.18) *is concave in the domain where*

$$\mathbf{u}_k^\top H \mathbf{u}_k + c^\top \mathbf{u}_k + \frac{1}{4} c^\top U_1 \Lambda_1^{-1} U_1^\top c \le \frac{1}{2} \tag{2.20}$$

is satisfied.

Proof. The Bhattacharyya coefficient can be represented as

$$\mathfrak{B}(\mathbf{u}_k) = a \exp(-\rho^2) \tag{2.21}$$

with

$$
\begin{aligned}
\rho^2 &= g^\top g \\
g &= \Lambda_1^{\frac{1}{2}} U_1^\top \mathbf{u}_k + \frac{1}{2} \Lambda_1^{-\frac{1}{2}} U_1^\top c \\
a &= \exp\left(\frac{1}{4} c^\top U_1 \Lambda_1^{-1} U_1^\top c - h\right).
\end{aligned}
\tag{2.22}
$$

The second derivative of (2.21) with respect to the radius ρ is non-positive for $\rho^2 \le \frac{1}{2}$, implying that the concave part of (2.18) is the domain where (2.20) is satisfied. □

As illustrated in Fig. 2.1, Lemma 2.1 implies that concavity is likely in the challenging conditions when the model differences indicated by $\Gamma^{[01]}$ in (2.14) are small and the noise contribution indicated by R is large. The term c grows with differences in state estimates per model. As long as the input remains small enough, and the candidate models do not differ significantly in resonance frequencies, the term c will remain small and the optimization problem is likely to be completely in the domain of concavity. Note that these conditions are again the most challenging for discrimination of models, whereas minimization of the Bhattacharyya coefficient is a concave problem for these conditions, which is computationally tractable for multiple types of constraints.

2.3.4. ONLINE CHECK FOR CONCAVITY OF (2.15)

FOR POLYTOPIC CONSTRAINTS

To see whether (2.15) is concave in the case of polytopic constraints, it is sufficient to check whether all vertices of the constraint set satisfy (2.20), for each model combination ij.

FOR ENERGY CONSTRAINTS

The input energy constraint set has the form

$$\mathcal{U} = \left\{ \mathbf{u}_k \,\middle|\, \|u_\ell\|_2^2 \le \varepsilon, \quad k+1 \le \ell \le k+N \right\}. \tag{2.23}$$

If the input sequence $\mathbf{u}_k = 0$ satisfies (2.20), it can be deduced that any point $\mathbf{u}_k$ for which $\|\mathbf{u}_k\|_2 \le \|z^*\|_2$, with

$$
\begin{aligned}
z^* &= \arg\min_z z^\top z \\
&\text{s.t. } z^\top H z + c^\top z + \frac{1}{4} c^\top U_1 \Lambda_1^{-1} U_1^\top c = \frac{1}{2}
\end{aligned}
\tag{2.24}
$$
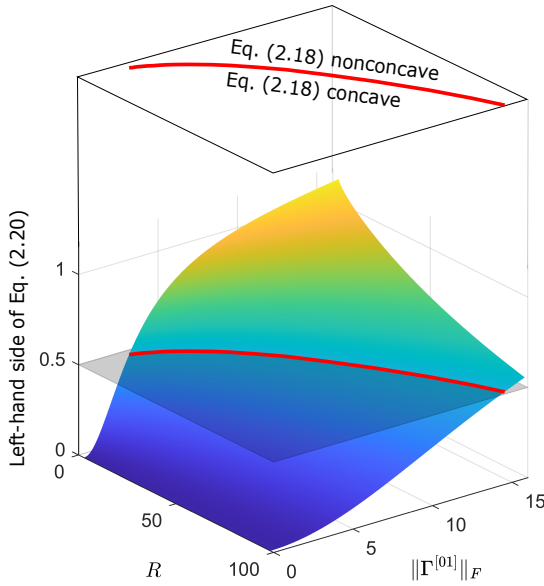
Figure 2.1: The compliance of (2.20) against measurement noise variance R and model differences $\left\|\Gamma^{[01]}\right\|_F$, generated with initial conditions, horizon N and model $M^{[0]}$ as in Sect. 2.4.1, $C^{[1]} = \text{constant} \cdot C^{[0]}$, and with inputs $\mathbf{u}_k = [-1, -1, -1, -1, 1, 1, -1, -1, 0, 0]^\top$. Large noise contribution and small model differences are favorable for satisfying (2.20).

is within the concave domain of (2.18). This optimization can be solved using only small computational effort as is shown in Appendix 2.C. Since there is an input energy constraint for each time step in the horizon,

$$\|u_{k+1}\|_2^2 + \|u_{k+2}\|_2^2 + \ldots + \|u_{k+N}\|_2^2 \le \varepsilon N$$

holds and therefore the optimization problem will be in the domain of concavity of (2.15) if $\sqrt{\varepsilon N} \le \|z^*\|_2$ is satisfied for each model combination ij.

These tests for concavity are performed each time step before the input determination. The assessment of concavity prior to the full closed-loop discrimination experiment requires closer investigation in future research. This deficiency however does not prevent the closed-loop approach from diagnosing the true candidate model. Instead, it is only uncertain whether the solution found each time step is the actual optimum of (2.15).

2.3.5. Quadratic Taylor approximation of (2.15)

The quadratic Taylor approximation of the Bhattacharyya coefficient around $\mathbf{u}_k = 0$ is

$$T_{\mathfrak{B}}(\mathbf{u}_k|0) = \mathfrak{B}(0)\left(\frac{1}{2}\mathbf{u}_k^\top\left(cc^\top - 2H\right)\mathbf{u}_k - c^\top\mathbf{u}_k + 1\right). \tag{2.25}$$

2

The Taylor approximation of the sum of weighted coefficients, such as the right-hand side of (2.10), can be obtained by taking the weighted sum of individual Taylor approximations. This means that minimization (2.15) is approximated by

$$\mathbf{u}_k^* = \arg\min_{\mathbf{u}_k \in \mathcal{U}} \sum_{\ell=k+1}^{k+N} \sum_i \sum_{j>i} \sqrt{P_k(M^{[i]})P_k(M^{[j]})} T_{\mathfrak{B}}(u_{k+1:\ell}|0). \tag{2.26}$$

Note that this quadratic approximation is significantly different from simply taking the sum of Bhattacharyya distances as in (2.17). It is more reasonable, since the error bound in (2.10) is now appropriately approximated, rather than only disregarding the model probabilities and base of exponentials as is done in (2.17).

2.3.6. Summary of approaches

Four MPC-based approximations and one open-loop (OL) approach of (2.7) will be compared. The Bhattacharyya Distance (BD) approach is reproduced from [15] and solves (2.17) in a receding horizon manner. The Bhattacharyya Coefficient (BC) approach solves (2.16) instead, given that the problem is within the domain of concavity. The validity of the optimum can be checked as described in Sect. 2.3.4. The Summed Bhattacharyya Coefficient (ΣBC) takes multiple time steps into account by solving (2.15), again while considering the domain of concavity. Next, the Quadratic Taylor Approximation (QTA) approach solves (2.26), yet only considering the error bound at time step $k+N$ in order to make a fair comparison with BD and BC. Lastly, the OL approach minimizes (2.16) offline (i.e., only at time step $k=0$) with very large horizon N.

2.4. Simulation Experiment

The proposed approaches are first tested in a setting with a polytopic constraint set on the inputs, as is done in [15]. Moreover, a Monte-Carlo simulation is conducted in order to assess the performance more generally. Additionally, they will be tested in a case with quadratic input constraints, aided by the DCCP toolbox [19]. A final simulation in Sect. 2.4.2 demonstrates how the methodology can be applied to a feedback controlled system.

The approaches were tested on the simulation setup given in [15]. The performances of the approaches were very similar to each other due to the chosen set of candidate models and small noise contribution, such that a well-designed input was not crucial for discrimination. In this section, we therefore created a more challenging case study, namely with multiple groups of close candidate models and large noise contribution.

2.4.1. Closed-loop diagnosis of an uncontrolled system

The candidate models in the simulation are constructed from a continuous-time harmonic oscillator with resonance $\pi/2$, damping 0.1 and discretized with sampling

time 1, such that the matrices[1]

$$A^{[i]} = \begin{bmatrix} -0.0792 + \Delta^{[i]} & -0.6746 \\ 1.0936 & 0.0926 \end{bmatrix},$$

$$B^{[i]} = \begin{bmatrix} 0.2734 & 1.5700 - \delta^{[i]} \\ 0.3677 & 0 \end{bmatrix}$$

$$\Delta = \{0, 0.2, 0.4, 1.0, 1.1\}$$

$$\delta = \{0, 0.1660, 0.3319, 0.8297, 0.9127\}$$

(2.27)

variable per model, and

$$C^{[i]} = C = \begin{bmatrix} 0 & 1 \\ 0.1 & 0.5 \end{bmatrix}$$

(2.28)

equivalent for each model, with in total five models $M^{[i]}$ constructed from taking $i = \{0,1,2,3,4\}$. The Gaussian noise contribution is relatively high with $Q = 0.2I_2$, $R = 80I_2$ and $S = 0$. Given these quantities, a Kalman filter [20] is constructed for online estimation of the system state and output, which are normally distributed. The initial state is $\hat{x}_{0|-1} = \begin{bmatrix} 0 & 1 \end{bmatrix}^\top$ with covariance $\Xi_{0|-1} = 0.5I_2$, and the initial probabilities are $P_0(M^{[i]}) = 0.2$ for each candidate model. For online determination of a separating input, the BD, QTA, BC and ΣBC approaches are implemented with receding horizon of length 5. Either if a model probability exceeds $1 - \epsilon = 0.98$, or if the number of measurements exceeds its maximum of 400, the discrimination experiment stops and the algorithm makes a decision about the underlying model of the system.

The OL approach uses a horizon of 200 time steps. The optimum is found as in [18] using sequential quadratic programming with 20 initializations. If a decision cannot be made after 200 time steps, the open-loop input is repeated.

For each experiment setting, the number of Monte-Carlo (MC) runs is 1000, with 200 per true candidate model, performed on an Intel i7-9750H CPU.

PARAMETERS FOR POLYTOPIC CONSTRAINT SET

For the experiment with polytopic constraint set, the input is restricted to

$$\mathcal{U} = \Big\{ \mathbf{u}_k \,\Big|\, \|u_\ell\|_\infty \le 2,$$

$$\|u_\ell - u_{\ell-1}\|_\infty \le 1, \quad k+1 \le \ell \le k+N \Big\}$$

After a check of concavity as described in Sect. 2.3.4, the optima for problems (2.15), (2.16), (2.17) and (2.26) (for the ΣBC, BC, BD and QTA approach, respectively) are found using an exhaustive search over the vertices.

---

[1]Note that these values are rounded. Simulation results using rounded values may differ from the results presented in this chapter. Besides, note that extension of the presented methodology to time-variant state-space matrices and model-dependent noise characteristics is straightforward.

PARAMETERS FOR QUADRATIC CONSTRAINT SET

The experiment with quadratic constraint set has restriction (2.23) with $\varepsilon = 2$. With a positive check for concavity as explained in Sect. 2.3.4, the minimization problems (2.15), (2.16), (2.17) and (2.26) are solved using DCCP [19].

RESULTS

The results for the polytopic and quadratic constraint set are presented as violin plots [24, 25] in Figs. 2.2 and 2.3, respectively. According to the online check as described in Sect. 2.3.4, all computations were done in the domain of concavity of (2.15) for BC and ΣBC in the experiment with polytopic constraint set. With the quadratic constraint set, at least 59.9% of the measurements yielded a domain where (2.16) (or (2.15) for ΣBC) is concave. In the other cases, a discriminating input will still be found, but without the guarantees of DCCP. As explained in Sect. 2.3.3, in these cases it is less crucial for the input to be optimally discriminating.

Figs. 2.2 and 2.3 show that in both cases with polytopic or quadratic constraints, the QTA, BC and ΣBC approaches require fewer measurements for diagnosis with confidence $1 - \epsilon$ than OL and BD. The OL approach shows in both experiments a bimodal distribution for the required number of measurements. This is caused by the composition of candidate models, of which three models $M^{[0]}$, $M^{[1]}$ and $M^{[2]}$ have high resonance frequency, whereas the other two models $M^{[3]}$ and $M^{[4]}$ have relatively low resonance frequency. This implies that the input frequency should be either low or high to separate these respective models. Since the OL approach has a predetermined input sequence for discriminating all candidate models within a certain time span, it will invariably first start with one frequency for a fixed amount of time, after which it applies the other frequency for another fixed period. Therefore, depending on the resonance frequency of the true system, the diagnosis will be either early or late.

Fig. 2.4 presents one realization of the closed-loop diagnosis approaches in the quadratic constraint set. The upper plot illustrates the latter phenomenon for the OL approach. As the black vertical bar indicates, the input frequency only increases after about 100 time steps, no matter what the system output is. In this realization, the true candidate model is a low-frequency model. Therefore the OL approach diagnoses it relatively quickly. Contrarily, the diagnosis in this experiment will be slower if the true model has high resonance frequency.

As opposed to open-loop, the closed-loop approaches do consider online measurements for updating the system inputs. Therefore, the QTA, BC and ΣBC approaches change the main input frequency as soon as the model probabilities 'suggest' this, as can be seen in the bottom plots in Fig. 2.4. Although the distributions between QTA, BC and ΣBC do not differ significantly in Fig. 2.3, the bottom plot in Fig. 2.4 shows that individual realizations of these approaches can actually differ.

Interestingly, in many cases the BD approach fails to diagnose with $1 - \epsilon$ confidence, even after 400 time steps. This is mainly due to disregarding the model probabilities in the optimization problem. As a result, it keeps trying to separate all five models simultaneously, while at some point several candidate models may become
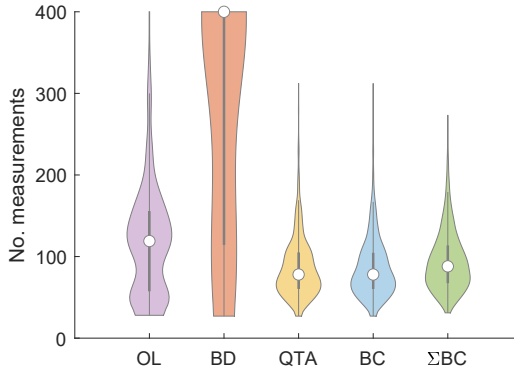
Figure 2.2: Number of measurements before decision in experiment with polytopic constraints for the four closed-loop methods, compared to open-loop. The medians are from left to right $\{119, 400, 78, 78, 88\}$ and the distributions of all methods differ significantly with MWW approximated p-value < 0.001, except the distribution pair (QTA, BC). The average computational time per measurement for the closed-loop methods was $\{10.8, 12.4, 26.1, 89.1\}$ milliseconds for BD, QTA, BC and ΣBC, respectively.
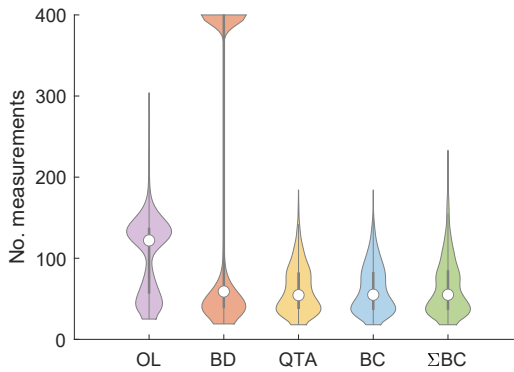
Figure 2.3: Number of measurements before decision in experiment with quadratic constraints for the four closed-loop methods, compared to open-loop. The medians are from left to right $\{122, 59, 54.5, 55, 55\}$. Although the distributions of QTA, BC and ΣBC do not differ significantly from each other, they do differ significantly from OL and BD with MWW approximated p-value < 0.001. The average computational time per measurement for the closed-loop methods was $\{223, 175, 310, 928\}$ milliseconds for BD, QTA, BC and ΣBC, respectively.
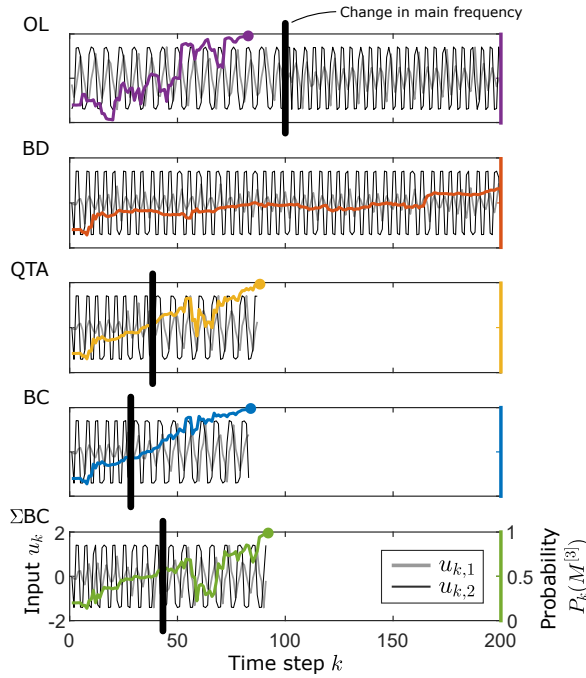
Figure 2.4: Applied inputs $u_k = [u_{k,1}, u_{k,2}]^\top$ for one realization of the approaches summarized in Sect. 2.3.6 in quadratic constraint set, with corresponding probability of true model $\mathbb{M}^{[3]}$. The black vertical bars indicate time instances at which the input pattern changes significantly in main frequency. The colored circles indicate time instances when the final decision is made. The BD approach did not present the change in main frequency and failed to decide after 200 time steps.

irrelevant due to low probability of being the true model. Another reason is that, even with equal model probabilities, optimization problem (2.17) is by no means an approximation to minimization of the original error bound (2.16) for the fact that minimizing the sum of exponents produces a different result than minimizing the sum of exponentials.

In terms of computational time, BD, QTA and BC are comparable. However, there seems to be a preference to BD and QTA, which have quadratic objective functions. The ΣBC approach generally uses more computational time, which is reasonable since it has more terms in the summation in the objective function.

2.4.2. CLOSED-LOOP DIAGNOSIS OF A FEEDBACK CONTROLLED SYSTEM

The closed-loop procedure for diagnosing faults can also be applied to feedback controlled systems as illustrated in Fig. 2.5 and described in Appendix 2.A. For this simulation experiment, the structure of the open-loop candidate models $\tilde{A}^{[i]}, \tilde{B}^{[i]}, \tilde{C}^{[i]}$

are chosen similar to (2.27) and (2.28) with

$$\Delta = \{2, 2.01, 2.02, 2.03, 2.04\}$$
$$\delta = \{1.6594, 1.6677, 1.6760, 1.6843, 1.6926\}$$

(2.29)

and

$$\tilde{Q} = I_2 \times 10^{-4}, \qquad \tilde{R} = I_2 \times 10^{-2}, \qquad \tilde{S} = 0.$$

(2.30)

These candidate models are stabilized by designing a controller for the nominal system with observer gain $K^{[0]}$ the Kalman gain and with feedback gain $F^{[0]}$ such that $\tilde{A}^{[0]} - \tilde{B}^{[0]} F^{[0]}$ has eigenvalues at 0.94 and 0.95. The feedforward gain $G^{[0]}$ is chosen such that the input u_k to the feedback controlled system acts as a reference for the system output.

In this proof-of-concept demonstration we regard a quadratic constraint set

$$\mathscr{U} = \left\{ \mathbf{u}_k \;\middle|\; \|u_\ell - r_\ell\|_2^2 \le \varepsilon, \quad k+1 \le \ell \le k+N \right\}.$$

(2.31)

such that the input u_k is bounded around a given reference signal $r_k = [3,5]^\top \; \forall k$ with $\varepsilon = 2.5 \times 10^{-3}$. With the straightforward translation $\mathbf{u}'_k = \mathbf{u}_k - \mathbf{r}_k$ this constraint set is equivalent to (2.23) such that the methodology presented in Sect. 2.3 is still applicable to this case. The closed-loop approach BC is implemented with a horizon of $N = 5$.

The results are presented in Fig. 2.6. According to the online check presented in Sect. 2.3.4, all computations were done in the concave domain of the Bhattacharyya coefficients. From Fig. 2.6 it can be concluded that it is impossible to reliably diagnose the model without using an auxiliary input. With the closed-loop approach BC however, an input is computed with a user-defined energy limit so that the system is minimally disturbed while still being able to diagnose the correct model after 400 time steps.
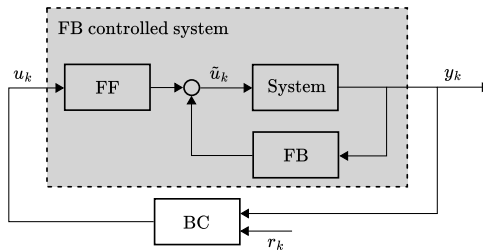

Figure 2.5: Online input design for discrimination of models for a feedback (FB) controlled system with observer, feedforward (FF) and feedback gains $K^{[0]}$, $G^{[0]}$ and $F^{[0]}$, respectively. The online input design method BC can also be replaced with one of the other methods proposed in this chapter ΣBC or QTA.

2
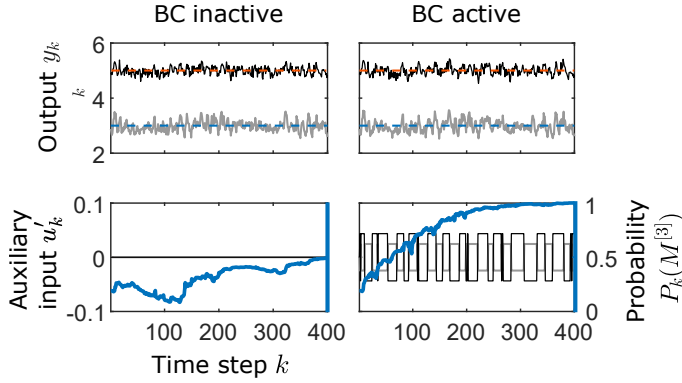
Figure 2.6: A feedback controlled system with and without auxiliary input generated by BC (right and left, respectively). The system outputs y_k (top) approximately track a reference $r_k = [3, 5]^\top$ (blue and red dashed, respectively) even though the auxiliary input $u'_k = u_k - r_k$ is applied. However, the correct model could be diagnosed with probability $P_{400}(M^{[3]}) \approx 1$ using BC, whereas this is not possible with $u'_k = 0 \; \forall k$.

2.5. APPLICATION TO ACTIVE OBJECT RECOGNITION

This section uses CLAFD for high-performance object recognition with minimal phototoxicity. The proposed closed-loop imaging scheme consists of a neural network cluster for diagnosing the object with a certain confidence, and of a controller for determination of the next minimally invasive yet discriminating illumination input. The vast majority of the computations can be done offline, such that fast online execution is ensured. Simulation experiments test the procedure on the MNIST handwritten digit dataset [26], after which the results can be compared to an open-loop approach.

2.5.1. PROBLEM REFORMULATION

Consider the objects to be imaged x_k for each time step k. The objects x_k can represent one of the N_M classes, therefore N_M hypotheses are defined:

$$M_i : x_k \in \mathcal{X}_i \quad \forall k \tag{2.32}$$

with $i \in \{0, 1, \ldots, N_M - 1\}$ and $\mathcal{X}_i$ the set of images corresponding to class i. The images are formed using

$$y_k = x_k \cdot u_k + v_k, \tag{2.33}$$

with $u_k \in \mathbb{R}_+^{m \times m}$ the illumination input, $y_k \in \mathbb{R}_+^{m \times m}$ the output intensity, $v_k \in \mathbb{R}^{m \times m}$ the noise at time step k, and the symbol $\cdot$ represents element-wise multiplication. With all measurements available up to (and including) y_{k-1}, the hypothesis probabilities $P_{k-1}(M_i)$ evolve according to the Bayesian update rule

$$P_{k-1}(M_i) = \frac{p(y_{k-1}|M_i, u_{k-1})P_{k-2}(M_i)}{p(y_{k-1}|u_{k-1})}, \tag{2.34}$$

where $p(y_{k-1}|M_i, u_{k-1}) \in \mathbb{R}_+$ is the probability density function (PDF) of output image y_{k-1}, conditioned on hypothesis M_i and input u_{k-1}. The initial conditions $P_0(M_i)$ can be set to any prior probabilities.

The goal is to minimize the probability misdiagnosis after the next measurement y_k, which is defined as [18]

$$P_{\mathrm{e}}(u_k) = \sum_i \sum_{j \neq i} \int_{\mathfrak{R}_j} p(y_k|M_i, u_k) P_{k-1}(M_i) \, \mathrm{d}y_k \tag{2.35}$$

where

$$\mathfrak{R}_j = \left\{ y_k \quad | \quad p(y_k|M_j, u_k) P_{k-1}(M_j) > p(y_k|M_i, u_k) P_{k-1}(M_i) \quad \forall i \neq j \right\}.$$

In the current application we limit the so-called input energy

$$\mathrm{vec}(u_k)^\top \mathrm{vec}(u_k) \leq \varepsilon. \tag{2.36}$$

This input will be evaluated in the "Controller"-block in Figure 2.7. The closed-loop procedure has the purpose of reducing phototoxicity while increasing the reliability of diagnosis. One can for instance limit the total energy $\sum_k \varepsilon$ by limiting the number of measurements, or alternatively predefine a desired probability of misdiagnosis and iterate the scheme until this confidence is achieved.

2.5.2. MULTIPLE-INPUT INFERENCE IMPLEMENTATION

For simplification of the problem, the images are split up in n^2 subimages with uniform input $u_{k,\ell} \in \mathbb{R}$ for $\ell \in \{1, 2, \ldots, n^2\}$. For each subimage, s neural networks are trained with varying prospected inputs. As depicted in Figure 2.8, the relative probabilities of the neural network outputs are evaluated using the accompanying PDFs for each hypothesis M_i. These PDFs were constructed by fitting Gaussian kernel density estimates to the neural network output distributions. Since multiple neural networks with different uniform illumination intensities are used for one single subimage, the outcome of the PDFs are linearly interpolated with respect to the actual illumination input. For combining the outcomes all subimages, the Bayesian update rule (2.34) is applied repetitively and for each hypothesis.

CLOSED-LOOP INPUT DETERMINATION

The probability of misdiagnosis in (2.35) is bounded by [18]

$$P_{\mathrm{e}}(u_k) \leq \sum_i \sum_{j > i} \sqrt{P_{k-1}(M_i) P_{k-1}(M_j)} \mathfrak{B}_{ij}(u_k) \tag{2.37}$$

for which the Bhattacharyya coefficient is defined as

$$\mathfrak{B}_{ij}(u_k) = \int \sqrt{p(y_k|M_i, u_k) p(y_k|M_j, u_k)} \, \mathrm{d}y_k. \tag{2.38}$$
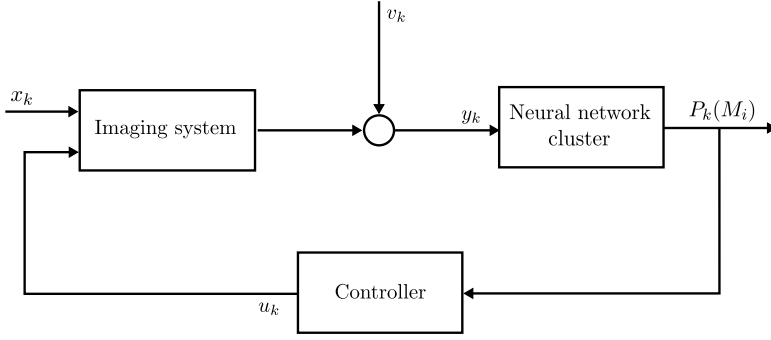
Figure 2.7:   Control scheme. The (unknown) object x_k is fed to the imaging system together with illumination input u_k. Its output is corrupted with noise v_k, after which y_k is measured. The neural network cluster updates the probabilities of each hypothesis, after which the controller determines the input for next measurement.
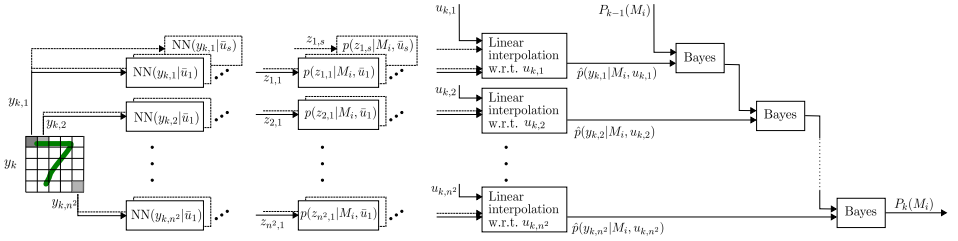
Figure 2.8:   Neural network cluster from Figure 2.7 unfolded. The images y_k are split up in n^2 subimages. Each subimage is fed to s different neural networks which are trained for varying prospected inputs $\bar{u}$. The neural network scalar outputs z are converted to their corresponding relative likelihood $p(z|M_i, \bar{u})$, using the probability density functions obtained in the training phase of the neural networks. Regarding the actual input u_k which was fed to the system to obtain y_k, the relative likelihoods are then linearly interpolated. Finally, the results of the n^2 estimated relative likelihoods are combined by successive Bayesian updates as in (2.34).

Furthermore, this inequality also holds for the subimages:

$$P_{\mathrm{e},\ell}(u_{k,\ell}) \leq \sum_i \sum_{j>i} \sqrt{P_{k-1}(M_i)P_{k-1}(M_j)} \mathfrak{B}_{ij,\ell}(u_{k,\ell}). \tag{2.39}$$

The total error probability is then obtained by applying the Bayesian update rule (2.34) to the hypothesis probabilities of all individual subimages, assumed

independence of the measurements. The task now is to distribute the inputs $u_{k,\ell}$ such that the total error probability is minimized. The next step approximates the Bhattacharyya coefficient with an affine function.

LEAST-SQUARES APPROXIMATION OF BHATTACHARYYA COEFFICIENT

A least-squares fit to the Bhattacharyya coefficient can be performed by fitting the function

$$\hat{\mathfrak{B}}_{ij,\ell}(u_{k,\ell}) = 1 + a_{ij,\ell} u_{k,\ell} \tag{2.40}$$

to the data gathered with the s training instances. Its solution is

$$a_{ij,\ell} = \frac{\mathfrak{B}_{ij}(\bar{u}_\ell)^\top \bar{u}_\ell - \|\bar{u}_\ell\|_1}{\bar{u}_\ell^\top \bar{u}_\ell} \tag{2.41}$$

with $\bar{u}_\ell = [\bar{u}_{\ell,1}^\top, \ldots, \bar{u}_{\ell,s}^\top]^\top$ the inputs for which the neural networks are trained.

INPUT DETERMINATION USING LEAST-SQUARES FIT

Using approximation (2.40), the double sum in (2.39) can be simplified to

$$\sum_i \sum_{j>i} \sqrt{P_{k-1}(M_i)P_{k-1}(M_j)}\,\mathfrak{B}_{ij,\ell_1}(u_{k,\ell}) \approx c_k - b_{k,\ell}u_{k,\ell} \tag{2.42}$$

with

$$b_{k,\ell} = -\sum_i \sum_{j>i} a_{ij,\ell}\sqrt{P_{k-1}(M_i)P_{k-1}(M_j)} \tag{2.43}$$

$$c_k = \sum_i \sum_{j>i} \sqrt{P_{k-1}(M_i)P_{k-1}(M_j)}. \tag{2.44}$$

Now, one can see that a large coefficient $b_{k,\ell}$ implies a high degree of distinction between relevant models with high belief states $P_{k-1}(M_i)$, at subimage ℓ. This reasoning suggests that

$$b_{k,\ell_1} > b_{k,\ell_2} \quad \Longrightarrow \quad u_{k,\ell_1} > u_{k,\ell_2} \tag{2.45}$$

(with $\ell_1 \neq \ell_2$ two different realizations of ℓ) is a sound rule for approximately minimizing the right-hand side of (2.37), and therefore for minimizing the error probability.

With the energy constraint in (2.36), a possible input choice is

$$u_{k,\ell} = \frac{n}{m}\sqrt{\frac{b_{k,\ell}}{\sum_{i=1}^{n^2} b_{k,i}}\varepsilon}. \tag{2.46}$$

This solution will not lead to an overall minimum error probability, yet requires low computational effort. Moreover, the Bhattacharyya coefficients and their least-squares approximations can be calculated offline, implying that only Equations (2.43) and (2.46) need to be determined online. The next section validates the improvement in recognition performance as compared to using a constant uniform input.

2.5.3. SIMULATION RESULTS

For the objects x_k, we used the MNIST handwritten digit dataset [26], normalized to the segment $[0, 1]$. The noise v_k is Gaussian with zero mean and variance $R_v = 0.04$ and the input energy for each measurement k is limited to $\varepsilon = 64$. The images are split into $n^2 = 49$ subimages. For each subimage, $s = 5$ neural networks are trained using inputs $\bar{u}_\ell = [0.2, 0.4, 0.6, 0.8, 1.0]^\top$. The neural network internal architecture is similar to a previous contribution[16], having three layers with 128, 10 and 1 neurons, respectively, with the first two layers a rectified linear unit (ReLU) activation function. It is optimized using the Adam optimizer [27] in the Tensorflow package [28].

Whereas the open-loop procedure uses constant and uniform illumination over the whole image, the closed-loop input is determined using (2.46). Two realizations of the closed-loop algorithm for true hypotheses M_5 and M_7 are shown in Figure 2.9. The challenging noise conditions in the output y_k require multiple measurements in order to find the true hypothesis with high confidence. Taking previous measurements into account, the input energy is distributed efficiently in order to achieve this high confidence in a small number of measurements.

For a Monte-Carlo simulation, 100 realizations are generated for each class, making a total of 1000 realizations. With a desired confidence of $P_k(M_i) \geq 0.98$ for any hypothesis M_i, the distribution of number of measurements before decision is presented in Figure 2.10. From the left plot it can be seen that the closed-loop approach requires in general fewer measurements as compared to the open-loop approach. Moreover, on average only 3.22 measurements are required instead of 4.37. The error rates are with 3.6% for open-loop and 2.7% for closed-loop slightly higher than the desired 2%. This is probably due to inaccuracies in obtaining the probability density functions from the neural network outputs. Besides, there might be a dependence between measurements in different subimages, whereas independence was assumed. Interestingly, the error rate was for the open-loop approach higher, while it uses on average more measurements than the closed-loop approach. So in fact, the open-loop approach would require even more measurements to obtain an error rate equivalent to the closed-loop approach.

The right plot in Figure 2.10 confirms the decrease in average number of measurements for each hypothesis. The digits 0 and 1 are on average diagnosed in fewer measurements than the remaining digits, which is presumably due to their apparent uniqueness in graphical appearance.

2.6. CONCLUSION

This chapter improves the trade-off between the three factors high accuracy, small number of consecutive measurements and low computational effort, with respect to existing stochastic CLAFD methods such as [15]. The proposed approach considers the weighted sum of Bhattacharyya coefficients as bound on the error probability, which is shown to be concave in the case of close linear candidate models with significant Gaussian process and measurement noise. In addition, a quadratic Taylor approximation of the error bound is proposed for a further speedup of

the computations without significantly sacrificing the discrimination performance. Simulation results show that the newly proposed approaches require a smaller number of measurements than the open-loop approach, whereas the approach in [15] frequently fails to decide at all with the predefined confidence. By additionally considering a similar computational effort, it can be concluded that the newly proposed approaches have favorable trade-off with respect to the state-of-the-art closed-loop method in [15].

In order to further improve the online input design, future research is suggested to focus on minimizing the actual error probability instead of only the bound. The approach proposed in this chapter can be used to initialize this nonlinear optimization problem.
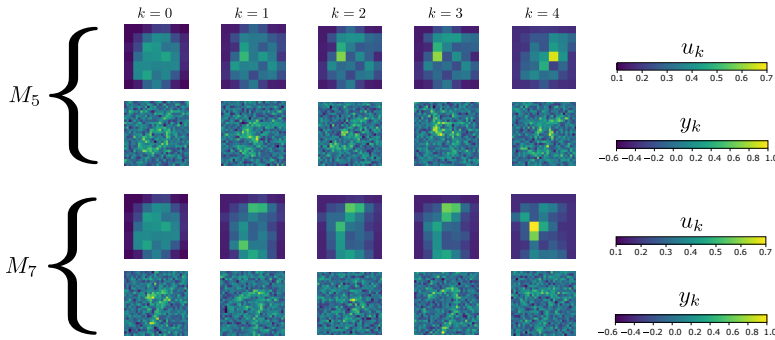
Figure 2.9:   Realizations of the closed-loop algorithm with true hypothesis M_5 (top) and M_7 (bottom).
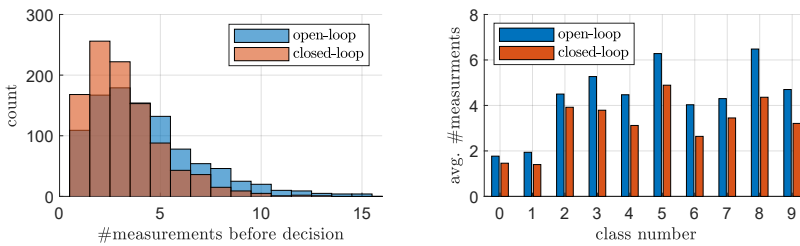

Figure 2.10:   Distribution of number of measurements before a decision with 98% desired confidence is taken, for open-loop (blue) and closed-loop solution (red). Overall distribution (left) and average number of measurements per hypothesis (right). The final error rates of the open- and closed-loop approaches were 3.6% and 2.7%, respectively.

2.A. APPLICABILITY FOR FEEDBACK CONTROLLED SYSTEMS

Consider the open-loop candidate models

$$M^{[i]} : \begin{cases} x_{k+1} &= \tilde{A}^{[i]} x_k + \tilde{B}^{[i]} \tilde{u}_k + \tilde{w}_k \\ y_k &= \tilde{C}^{[i]} x_k + \tilde{v}_k \end{cases} \tag{2.47}$$

with the joint covariance matrix of the noise sequences

$$\mathbb{E}\left[\begin{bmatrix} \tilde{v}_k \\ \tilde{w}_k \end{bmatrix} \begin{bmatrix} \tilde{v}_\ell^\top & \tilde{w}_\ell^\top \end{bmatrix}\right] = \begin{cases} \begin{bmatrix} \tilde{R} & \tilde{S}^\top \\ \tilde{S} & \tilde{Q} \end{bmatrix} & \text{if } k = \ell, \\ 0 & \text{otherwise.} \end{cases} \tag{2.48}$$

A feedback controller is constructed for the nominal model

$$\tilde{u}_k = -F^{[0]} \hat{x}_{k|k-1}^{[0]} + G^{[0]} u_k \tag{2.49}$$

with $F^{[0]}$ and $G^{[0]}$ the feedback and feedforward gains. The state estimate is given by

$$\hat{x}_{k+1|k}^{[0]} = \tilde{A}^{[0]} \hat{x}_{k|k-1}^{[0]} + \tilde{B}^{[0]} \tilde{u}(k) + K^{[0]}\left(y(k) - \tilde{C}^{[0]} \hat{x}_{k|k-1}^{[0]}\right) \tag{2.50}$$

with $K^{[0]}$ the observer gain. The resulting closed-loop dynamics of the candidate models are described by (2.1) and (2.2) with

$$\begin{aligned}
A^{[i]} &= \begin{bmatrix} \tilde{A}^{[i]} & -\tilde{B}^{[i]} F^{[0]} \\ K^{[0]} \tilde{C}^{[i]} & \tilde{A}^{[0]} - \tilde{B}^{[0]} F^{[0]} - K^{[0]} \tilde{C}^{[0]} \end{bmatrix}, \\
B^{[i]} &= \begin{bmatrix} \tilde{B}^{[i]} \\ \tilde{B}^{[0]} \end{bmatrix} G^{[0]}, \qquad C^{[i]} = \begin{bmatrix} \tilde{C}^{[i]} & 0 \end{bmatrix}, \\
Q &= \begin{bmatrix} \tilde{Q} & \tilde{S}(K^{[0]})^\top \\ K^{[0]} \tilde{S}^\top & K^{[0]} \tilde{R}(K^{[0]})^\top \end{bmatrix}, \\
S &= \begin{bmatrix} \tilde{S} \\ K^{[0]} \tilde{R} \end{bmatrix}, \qquad\qquad R = \tilde{R}.
\end{aligned} \tag{2.51}$$

2.B. DEFINITIONS FOR (2.12)

Whereas the definitions of $H^{[ij]}$ and $c^{[ij]}$ are given in (2.13), the variable $h^{[ij]}$ is defined as

$$\begin{aligned}
h^{[ij]} = {} & \frac{1}{4} (\zeta^{[ij]})^\top (\Omega^{[ij]})^{-1} \zeta^{[ij]} \\
& + \frac{1}{2} \log\left(\frac{\left|\frac{1}{2}\Omega^{[ij]}\right|}{\sqrt{\left|\Sigma_{k|k}^{[i]}\right|\left|\Sigma_{k|k}^{[j]}\right|}} \right)
\end{aligned} \tag{2.52}$$

with $|\cdot|$ indicating the determinant operator.

The boldface matrices and Toeplitz matrix in (2.14) are given by the state-space matrices in (2.1) as (with indices i omitted for clarity)

$$\mathbf{A} = \begin{bmatrix} I \\ A \\ \vdots \\ A^{N-1} \end{bmatrix}, \qquad \mathbf{B} = I_N \otimes B, \qquad \mathbf{C} = I_N \otimes C,$$

$$\mathscr{T}_A = \begin{bmatrix} 0 & 0 & \dots & 0 & 0 \\ I & 0 & \dots & 0 & 0 \\ A & I & \ddots & \vdots & \vdots \\ \vdots & \ddots & \ddots & 0 & 0 \\ A^{N-2} & \dots & A & I & 0 \end{bmatrix}$$

with I_N the N-by-N identity matrix and $\otimes$ the Kronecker product. Moreover, the equations for models (2.1) can be expanded to

$$\begin{aligned} \mathbf{x}_k &= \mathbf{A}x_{k+1} + \mathscr{T}_A\mathbf{B}u_k + \mathscr{T}_A\mathbf{w}_k \\ \mathbf{y}_k &= \mathbf{C}\mathbf{x}_k + \mathbf{v}_k \end{aligned} \tag{2.53}$$

with $\mathbf{w}_k \sim \mathcal{N}(0,\mathbf{Q})$ and $\mathbf{v}_k \sim \mathcal{N}(0,\mathbf{R})$. Given the joint covariance matrix in (2.2), the extended covariance matrices are defined as

$$\mathbf{Q} = I_N \otimes Q, \quad \mathbf{R} = I_N \otimes R,$$

$$\mathbf{S} = \mathbb{E}\left[\mathbf{w}_k\mathbf{v}_{k+1}^\top\right] = \begin{bmatrix} 0 & 0 & \dots & 0 \\ S & 0 & \dots & 0 \\ \vdots & \ddots & \ddots & \vdots \\ 0 & \dots & S & 0 \end{bmatrix}. \tag{2.54}$$

The predicted output sequence with corresponding covariance matrix is

$$\begin{aligned} \hat{\mathbf{y}}_{k|k} &= \mathbf{C}\mathbf{A}\hat{x}_{k+1|k} + \mathbf{C}\mathscr{T}_A\mathbf{B}u_k \\ \Sigma_{k|k} &= \mathbf{C}\mathbf{A}\Xi_{k+1|k}\mathbf{A}^\top\mathbf{C}^\top + \mathbf{C}\mathscr{T}_A\mathbf{Q}\mathscr{T}_A^\top\mathbf{C}^\top \\ &\quad + \mathbf{C}\mathscr{T}_A\mathbf{S} + \mathbf{S}^\top\mathscr{T}_A^\top\mathbf{C}^\top + \mathbf{R} \end{aligned} \tag{2.55}$$

with $\Xi_{k+1|k}$ the state-error covariance matrix corresponding to state estimate $\hat{x}_{k+1|k}$. The covariance matrix $\Sigma_{k|k}$ is then used in (2.14) and (2.52) to determine the Bhattacharyya distance in (2.12).

2.C. SOLUTION OF (2.24)

With the definitions in (2.22), optimization (2.24) can be rewritten as

$$g^* = \underset{g}{\arg\min}\ g^\top \Lambda_1^{-1} g - c^\top U_1 \Lambda_1^{-\frac{3}{2}} g \tag{2.56}$$

$$\text{s.t. } g^\top g = \frac{1}{2},$$

which in turn is equivalent to

$$q^* = \arg\min_q q^\top \Lambda_1^{-1} q + b^\top q$$

$$\text{s.t. } q^\top q = \frac{1}{2},$$

$$(2.57)$$

with Λ_1 a diagonal matrix with elements $\lambda_1 \geq \lambda_2 \geq \ldots \geq \lambda_n > 0$ and $b \geq 0$. The Lagrangian of (2.57) equals

$$\mathscr{L}(q,\tau) = q^\top \Lambda_1^{-1} q + b^\top q - \tau \left(q^\top q - \frac{1}{2} \right). \tag{2.58}$$

The solution is given by the stationary point of the Lagrangian and should therefore satisfy

$$\begin{cases} q_1 = \dfrac{b_1}{2\left(\tau - \lambda_1^{-1}\right)} \\ \quad\vdots \\ q_n = \dfrac{b_n}{2\left(\tau - \lambda_n^{-1}\right)} \\ q^\top q = \dfrac{1}{2} \end{cases} . \tag{2.59}$$

with b_i, q_i the ith element in b or q, respectively. This system of equation can be seen as intersection of a parametrically defined critical curve $q(\tau)$ defined by its first n equations with the sphere $\mathscr{B}$ of radius $1/\sqrt{2}$. On the other hand, it can be rewritten into one polynomial equation in variable τ of degree $2n$, and there exist no more than $2n$ intersection points corresponding to the polynomial roots, which can be found numerically by root-finding methods. For each of the intersection points, the objective function of (2.57) can be calculated and the point giving the minimal value provides the solution of (2.57). The searching range of τ for the root-finding methods can be reduced significantly by using the following considerations.

Due to the symmetry of the constraints of (2.57) and b being non-negative, the solution of (2.57) lies in the negative orthant, and therefore $\tau \in (-\infty, \lambda_1^{-1})$. On this interval, each of the first n equations of (2.59) is negative, continuous, and monotonically decreasing, and thus the point $q(\tau)$ on the critical curve goes out of the origin (at $\tau = -\infty$) with continuously and monotonically increasing distance to the origin, with $|q(\lambda_1^{-1})| = \infty$. Therefore, the range of τ can be reduced to that part of the curve which lies outside the inscribed hypercube in $\mathscr{B}$ and inside the circumscribed hypercube around $\mathscr{B}$. The inscribed hypercube is given by conditions $\{|q_i| \leq 1/\sqrt{2n}, \ i = 1, \ldots n\}$, and thus for

$$\tau \leq \tau_- \overset{\text{def}}{=} \min_i \lambda_i^{-1} - \sqrt{\frac{n}{2}} b_i,$$

the critical curve is still inside the inscribed hypercube. Similarly, the circumscribed hypercube is given by $\{|q_i| \leq 1/\sqrt{2}, \ i = 1, \ldots n\}$ and the curve is still inside it for

$$\tau \leq \tau_+ \overset{\text{def}}{=} \min_i \lambda_i^{-1} - \frac{1}{\sqrt{2}} b_i.$$

The root-searching method can be thus reduced to the interval $[\tau_-, \tau_+]$. Finally, because $|q(\tau)|$ is continuous and monotone on this interval, the solution exists and is unique.

2

REFERENCES

[1]   J. Noom, O. Soloviev, C. Smith, and M. Verhaegen. *Online input design for discrimination of linear models using concave minimization*. 2024. arXiv: 2401.05782 [eess.SY].

[2]   J. Noom, O. Soloviev, C. Smith, and M. Verhaegen. "Closed-loop active object recognition with constrained illumination power". In: *Real-Time Image Processing and Deep Learning 2022*. Ed. by N. Kehtarnavaz and M. F. Carlsohn. Vol. 12102. International Society for Optics and Photonics. SPIE, 2022, pp. 9–14. DOI: 10.1117/12.2618750.

[3]   J. Noom. *Matlab code for online input design for discrimination of linear models using concave minimisation*. 2024. DOI: 10.5281/zenodo.6642321.

[4]   Z. Gao, C. Cecati, and S. X. Ding. "A survey of fault diagnosis and fault-tolerant techniques-part I: Fault diagnosis with model-based and signal-based approaches". In: *IEEE Transactions on Industrial Electronics* 62.6 (2015), pp. 3757–3767. DOI: 10.1109/TIE.2015.2417501.

[5]   W. Rawat and Z. Wang. "Deep Convolutional Neural Networks for Image Classification: A Comprehensive Review". In: *Neural Computation* 29.9 (2017), pp. 2352–2449. DOI: 10.1162/neco_a_00990.

[6]   T. A. N. Heirung and A. Mesbah. "Input design for active fault diagnosis". In: *Annual Reviews in Control* 47 (2019), pp. 35–50. DOI: 10.1016/j.arcontrol.2019.03.002.

[7]   W. G. Hunter and A. M. Reiner. "Designs for Discriminating Between Two Rival Models". In: *Technometrics* 7.3 (1965), pp. 307–323. DOI: 10.1080/00401706.1965.10490265.

[8]   G. E. Box and W. J. Hill. "Discrimination Among Mechanistic Models". In: *Technometrics* 9.1 (1967), pp. 57–71. DOI: 10.1080/00401706.1967.10490441.

[9]   X. J. Zhang and M. B. Zarrop. "Auxiliary signals for improving on-line fault detection". In: *1988 International Conference on Control*. 1988, pp. 414–419.

[10] I. Punčochář and J. Škach. "A Survey of Active Fault Diagnosis Methods". In: *IFAC-PapersOnLine* 51.24 (2018), pp. 1091–1098. DOI: 10.1016/j.ifacol.2018.09.726.

[11] S. Yang, F. Xu, X. Wang, and B. Liang. "A Novel Online Active Fault Diagnosis Method Based on Invariant Sets". In: *IEEE Control Systems Letters* 5.2 (2021), pp. 457–462. DOI: 10.1109/LCSYS.2020.3003875.

[12] D. M. Raimondo, G. Roberto Marseglia, R. D. Braatz, and J. K. Scott. "Closed-loop input design for guaranteed fault diagnosis using set-valued observers". In: *Automatica* 74 (2016), pp. 107–117. DOI: 10.1016/j.automatica.2016.07.033.

[13] I. Punčochář, J. Škach, and M. Šimandl. "Infinite time horizon active fault diagnosis based on approximate dynamic programming". In: *2015 54th Proceedings of the IEEE Conference on Decision and Control*. 2015, pp. 4456–4461. DOI: 10.1109/CDC.2015.7402915.

[14] J. K. Scott, G. Roberto Marseglia, L. Magni, R. D. Braatz, and D. M. Raimondo. "A hybrid stochastic-deterministic input design method for active fault diagnosis". In: *52nd IEEE Conference on Decision and Control*. 2013, pp. 5656–5661. DOI: 10.1109/CDC.2013.6760780.

[15] J. A. Paulson, T. A. N. Heirung, R. D. Braatz, and A. Mesbah. "Closed-Loop Active Fault Diagnosis for Stochastic Linear Systems". In: *2018 Annual American Control Conference*. 2018, pp. 735–741. DOI: 10.23919/ACC.2018.8431031.

[16] J. Noom, N. H. Thao, O. Soloviev, and M. Verhaegen. "Closed-Loop Active Model Diagnosis Using Bhattacharyya Coefficient: Application to Automated Visual Inspection". In: *Intelligent Systems Design and Applications (ISDA 2020)*. Ed. by A. Abraham, V. Piuri, N. Gandhi, P. Siarry, A. Kaklauskas, and A. Madureira. Springer, Cham, 2021, pp. 657–667. DOI: 10.1007/978-3-030-71187-0_60.

[17] D. E. Boekee and J. C. van der Lubbe. "Some aspects of error bounds in feature selection". In: *Pattern Recognition* 11.5 (1979), pp. 353–360. DOI: 10.1016/0031-3203(79)90047-5.

[18] L. Blackmore and B. Williams. "Finite Horizon Control Design for Optimal Discrimination between Several Models". In: *45th IEEE Conference on Decision and Control*. 2006, pp. 1147–1152. DOI: 10.1109/CDC.2006.377045.

[19] X. Shen, S. Diamond, Y. Gu, and S. Boyd. "Disciplined Convex-Concave Programming". In: *55th Conference on Decision and Control*. 2016, pp. 1009–1014. DOI: 10.1109/CDC.2016.7798400.

[20] M. Verhaegen and V. Verdult. *Filtering and System Identification: A Least Squares Approach*. Cambridge: Cambridge University Press, 2007. ISBN: 978-1107405028.

[21] D. Bertsekas and S. Shreve. *Stochastic Optimal Control: The Discrete Time Case*. Mathematics in science and engineering. Academic Press, 1978. ISBN: 9780120932603.

[22] I. Rish. "An empirical study of the naive Bayes classifier". In: *IJCAI workshop on empirical methods in artificial intelligence*. 2001.

[23] D. Q. Mayne, J. B. Rawlings, C. V. Rao, and P. O. Scokaert. "Constrained model predictive control: Stability and optimality". In: *Automatica* 36.6 (2000), pp. 789–814. DOI: 10.1016/S0005-1098(99)00214-9.

[24] J. L. Hintze and R. D. Nelson. "Violin Plots: A Box Plot-Density Trace Synergism". In: *The American Statistician* 52.2 (1998), pp. 181–184. DOI: 10.1080/00031305.1998.10480559.

[25] B. Bechtold. *Violin Plots for Matlab*. Github project. 2016. URL: https:
      //github.com/bastibe/Violinplot-Matlab.

[26] Y. LeCun, L. Bottou, Y. Bengio, and P. Haffner. "Gradient-based learning
      applied to document recognition". In: *Proceedings of the IEEE* 86.11 (1998),
      pp. 2278–2324. DOI: 10.1109/5.726791.

[27] D. P. Kingma and J. L. Ba. "Adam: A method for stochastic optimization".
      In: *International Conference on Learning Representations (ICLR)*. 2015. DOI:
      10.48550/arXiv.1412.6980.

[28] *TensorFlow: Large-Scale Machine Learning on Heterogeneous Systems*. 2015.
      URL: https://www.tensorflow.org/.

2

3

SPARSE FAULT DIAGNOSIS FOR HIGH-SPEED ATOMIC FORCE MICROSCOPY

We propose to use the State Estimation by Sum-of-Norms Regularization (STATESON) algorithm for recovering the tip-sample interaction in high-speed tapping mode atomic force microscopy (AFM). This approach enables accurate sample height estimation for each independent cantilever oscillation period, provided that the tip-sample interaction dominates the noise. The entire course of the cantilever deflection signal is compared to a modeled counterpart in subsequent convex minimizations, such that the sparse tip-sample interaction can be recovered. Afterwards, the sample height is determined using the minimum smoothed cantilever deflection per cantilever oscillation period. Results from simulation experiments are in favor of the proposed approach as it consistently reveals sharp edges in sample height, as opposed to both the conventional and a closely related existing approach. However, the non-processed cantilever deflection provided most accurate sample height estimation. It is recommended to implement the STATESON-algorithm in the form of a filter to use it in feedback control of the scanner and cantilever excitation.

3.1. INTRODUCTION

The Atomic Force Microscope (AFM), invented by Binnig and Quate in 1986 [3], is a versatile instrument which can be used for imaging and manipulation of biological samples. High-Speed tapping mode AFM (HS-AFM) facilitates videos of living biological samples at molecular scale [4–7], enabling biologists to make new discoveries (e.g. [8]). A tiny cantilever with length of several micrometers oscillates above the sample, tapping the sample intermittently. Variations in cantilever oscillation amplitude enable controlling the scanner height. The sample height is determined directly from the control input. Both high scan speed and accuracy are required to produce a proper video with high frame rate. Considering that (living) biological samples are primarily imaged in liquid (e.g. [8–10]), a main limitation of conventional methods is the dependence on the Lock-In Amplifier (LIA) (or alternatively the phase-locked loop). Two drawbacks of the LIA are that (a) determination of the amplitude takes multiple cantilever oscillation periods, and (b) higher order cantilever dynamics containing important information of the tip-sample (t/s-) interaction are filtered out. This results in a shifted image with low sharpness at high scan speeds. Therefore, effort should be taken to process the available data more appropriately.

Sahoo and co-workers [11] used the entire course of the cantilever deflection signal to determine the presence of t/s-interaction at specific locations above the sample. The detection was based on the Willsky-Jones generalized likelihood ratio method [12], in which the impulsive disturbances are detected one by one in chronological order. An adaptive filtering scheme [12] provided estimates of the t/s-interaction. However, future estimates are corrupted by past (fixed) estimates and the procedure could only detect the presence of the sample, but not its height. In [13], the detection was extended for providing images by calculating the power of the innovation signal, which was presumably used as scaled sample height estimate.

More approaches for recovering the t/s-interaction in HS-AFM have been developed in [14–17]. In contrast to the former two methods [14, 15], Karvinen *et al.* [16] employ the impulsive nature of the interaction, making the recovery less sensitive to noise. Although the time instances of the pulses are fixed in [16], the magnitudes of previously estimated pulses are more flexible than in [11], such that future estimates of the t/s-interaction are less influenced by previous estimates. Nevertheless, the assumptions in [16] involving fixed time instances of pulses is too restrictive. In [17], (semi-)periodicity of t/s-interaction is still assumed, requiring a cumbersome system augmentation involving *a priori* modeling of a chosen number of harmonics above the noise level.

In this chapter, the complete t/s-interaction is estimated based on its sparsity by the State Estimation by Sum-of-Norms Regularization (STATESON-)algorithm [18]. This pragmatic algorithm is a convex relaxation of the problem for recovering abrupt disturbances [18] in any linear dynamical system and therefore likely to be applicable to postprocess HS-AFM data for recovering the t/s-interaction. For this, the exclusive assumption is made that the t/s-interaction is pulse-like. As opposed to [16, 17] where the idea was to use the estimated t/s-interaction as input for the controller, our final goal is to estimate the sample height as accurate as possible. After applying

an equivalent extension for reconstructing the sample height to the method in [16], the results will be compared. In the analysis an additional approach has emerged which is also taken into account in the comparison.

The chapter starts with presenting a state-space description [19] of the cantilever, which will be used in the evaluation of both the algorithm presented in [16] and the one presented in this chapter based on the STATESON-algorithm. After describing the two algorithms in Sect. 3.2, the experimental design of the simulation study and corresponding results are presented in Sect. 3.3 and 3.4, respectively. The results are discussed in Sect. 3.5. Lastly, Sect. 3.6 states the conclusions.

3.2. METHODOLOGY

The AFM is shown schematically in Fig. 3.1(a). The cantilever deflection is measured through a reflected laser beam on a photodetector. This signal y_c is in a conventional manner fed to a lock-in amplifier (LIA), after which its oscillation amplitude A_c is used for control u_z of the scanner height z. In this section the conversion from cantilever input u_c and output y_c to t/s-interaction $\hat{F}$ and estimated deflection $\hat{y}$ will be elaborated. This will (together with estimated table height $\hat{z}$) eventually lead to estimates of the sample height $\hat{h}$.

The cantilever dynamics can be approximated by the linear time-invariant (LTI-) system [19]

$$x(k+1) = Ax(k) + B\bar{u}(k) + H\eta(k)$$
$$y_c(k) = Cx(k) + v(k),$$

(3.1)

with A, B, H and C the (known) system matrices; $y_c(k)$ the measured cantilever deflection at time step k; $\bar{u}(k) = u_c(k) + F(k)$ consists of the known input signal $u_c(k)$ (driving force) and the unknown t/s-interaction $F(k)$; $x(k)$ is the state; and $\eta(k)$ and $v(k)$ are the (approximately white) process and measurement noise with variances R_η and R_v. With $u_c(k)$ and $y_c(k)$ measured for $k = \{1, 2, \ldots, N\}$ the first task is to recover $F(k)$ for $k = \{1, 2, \ldots, N-1\}$.

Due to sinusoidal actuation of the cantilever, the tip makes intermittently contact with the sample. This implies that $F(k)$ can be approximated with a sparse signal. The following two methods reconstruct $F(k)$ based on this assumption.

3.2.1. KALMAN FILTER FORMULATION

The method in Karvinen *et al.* [16] involves two assumptions in order to cast it in the so-called Kalman Filter Formulation (KFF). Firstly, the pulses occur regularly at specific time instances:

$$F(k) = \begin{cases} F(k) & \text{if } k = k_F T / T_s \\ 0 & \text{otherwise} \end{cases}$$

(3.2)

with T the cantilever oscillation period in seconds, T_s the sampling time and $k_F \in \mathbb{N}_0$ is a non-negative integer. Secondly, the impulse response of system (3.1) becomes negligible after T_d seconds.
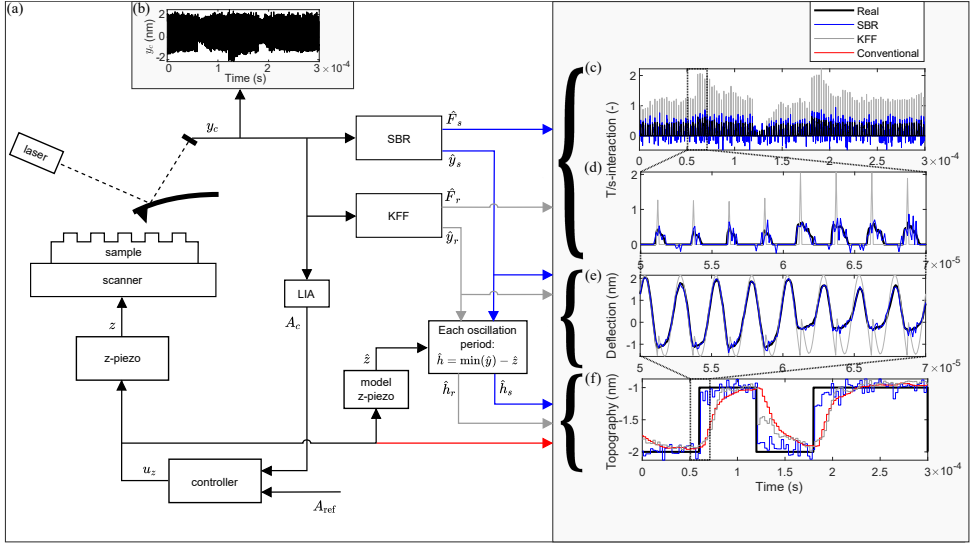
Figure 3.1: (a) Illustration of AFM-operation with additional processing (the four blocks on the right-hand side). Directly measured output data y_c is captured and fed to SBR (see Sect. 3.2.2) and KFF (from [16], summarized in Sect. 3.2.1), which recover the tip-sample interaction and smooth (or filter) the output resulting in $\hat{F}$ and $\hat{y}$. The LIA extracts the oscillation amplitude A_c from y_c, which serves as input for the controller, which in turn determines the control input to the scanner u_z for adjusting the table height z. As the signal z cannot be measured, a model for the z-piezo is used to form an estimate $\hat{z}$, which can be used for the two new methods for estimating the sample height h with $\hat{h}$. (b)-(f) Simulation of the algorithms from measured cantilever deflection to estimates of the sample height. (b) The measured cantilever deflection. (c) The real t/s-interaction (black) with estimates using KFF (gray) and SBR (blue). (d) t/s-interactions and estimates enlarged. (e) The (smoothed) cantilever deflection corresponding to zoomed t/s-interactions. (f) The actual and estimated topographies in original time frame including the conventional estimate (red). © 2023 IEEE.

The KFF-approach is based on a new state-space representation with the state consisting of the magnitudes of the relevant past pulses:

$$\theta(k) = \begin{bmatrix} F(\ell_1(k)) & F(\ell_1(k) - \lfloor T/T_s \rfloor) & \dots & F(\ell_2(k)) \end{bmatrix}^\top$$

and

$$\ell_1(k) = \left\lfloor \left\lfloor \frac{kT_s}{T} \right\rfloor \frac{T}{T_s} \right\rfloor,$$
$$\ell_2(k) = \left\lfloor \left\lceil \frac{kT_s - T_d}{T} \right\rceil \frac{T}{T_s} \right\rfloor.$$

with $\lfloor \bullet \rfloor$, $\lceil \bullet \rceil$, $\lfloor \bullet \rceil$ representing the floor, ceiling and nearest integer function. Note that the length of $\theta(k)$ can vary over time as T_d is not necessarily an integer multiple of T. The state-space equation becomes

$$\theta(k+1) = \mathscr{A}(k)\theta(k) + \mu(k)$$
$$y_2(k) = \mathscr{C}(k)\theta(k) + \gamma(k) \tag{3.3}$$

with

$$\mathscr{C}(k) = \begin{bmatrix} \begin{cases} 0 & \text{if } k-\ell_1 = 0 \\ CA^{(k-\ell_1-1)}B & \text{if } k-\ell_1 > 0 \end{cases} \\ CA^{(k-\ell_1-1+T/T_s)}B \\ \vdots \\ CA^{(k-\ell_2-1)}B \end{bmatrix}^\top,$$

$$\mu(k) = \begin{cases} \begin{bmatrix} \delta(k) & 0 & \dots & 0 \end{bmatrix}^\top & \text{if } k = (k_F T + \Delta)/T_s \\ \begin{bmatrix} 0 & 0 & \dots & 0 \end{bmatrix}^\top & \text{otherwise.} \end{cases}$$

The matrix $\mathscr{A}(k)$ is usually identity, except for the case when a new pulse appears in $\theta(k)$ (i.e. $\ell_1(k) \neq \ell_1(k-1)$) or if an old pulse disappears beyond the T_d-limit (i.e. $\ell_2(k) \neq \ell_2(k-1)$). See [[16], Appendix A] for more details on updating $\mathscr{A}(k)$. The variable $\delta(k)$ is a white noise sequence with variance R_δ. On the contrary, $\gamma(k)$ is a result of both $\eta(\{1,2,\dots,k\})$ and $\nu(k)$, from which the former introduces colored noise according to (3.1). Yet, a Kalman Filter (which is designed for systems with white noise) is applied in [16] to estimate $\theta(k)$.

The Kalman Filter equations for system (3.3) read as:

$$K(k) = P(k|k-1)\mathscr{C}(k)^\top$$
$$\times \left(R_\gamma + \mathscr{C}(k)P(k|k-1)\mathscr{C}(k)^\top \right)^{-1} \tag{3.4a}$$
$$\hat{\theta}(k|k) = \hat{\theta}(k|k-1)$$
$$+ K(k)\left(y_2(k) - \mathscr{C}(k)\hat{\theta}(k|k-1) \right) \tag{3.4b}$$
$$P(k|k) = \left(I - K(k)\mathscr{C}(k) \right)P(k|k-1) \tag{3.4c}$$
$$\hat{\theta}(k+1|k) = \mathscr{A}(k)\hat{\theta}(k|k) \tag{3.4d}$$
$$P(k+1|k) = \mathscr{A}(k)P(k|k)\mathscr{A}(k)^\top + Q(k) \tag{3.4e}$$

with R_γ the variance of sequence $\gamma(k)$. Furthermore, note that initial guesses $P(1|0)$ and $\hat{\theta}(1|0)$ are required for execution. Similarly to the matrix $\mathscr{A}$, the matrix $Q(k)$ usually consists of zeros, except for the case when a new pulse appears in $\theta(k)$, which results in the upper-left element of $Q(k)$ being equal to R_δ. The last entry of $\hat{\theta}(k|k)$ is expected to contain the most accurate estimate of $F(k)$ and is therefore used as final estimate $\hat{F}(k)$.

Choosing R_δ is nontrivial, for the definition of $\delta(k)$ in combination with updating rules of $\mathscr{A}(k)$ result in the nonzero elements in $F(k)$ being modeled as a Gaussian random walk (with mean zero), which is disputable. Besides, the choice of R_γ may be nontrivial due to the nonphysical definition of $\gamma(k)$, as opposed to $\eta(k)$ and $\nu(k)$.

The cantilever deflection can be reconstructed using

$$\hat{x}(k+1) = A\hat{x}(k) + B\hat{u}(k)$$
$$\hat{y}_{\text{KFF}}(k) = C\hat{x}(k)$$

(3.5)

with $\hat{u}(k) = u_c(k) + \hat{F}(k)$.

3.2.2. The proposed approach: sparsity-based reconstruction

The proposed approach entitled Sparsity-Based Reconstruction (SBR) employs the STATESON-algorithm presented in [18]. This algorithm is aimed at finding state estimates $\hat{x}(k)$ under additive pulse-like disturbances to the state equation. Sparsity of the t/s-interaction $F(k)$ is the only assumption. The algorithm starts with iterating the following two steps to find the time instances k at which a pulse occurred:

1. Minimize

$$[\hat{x}_l(1), \hat{F}_l(k), \hat{\eta}_l(k)] =$$

$$\underset{\substack{x(1), F(i), \eta(i) \\ 1 \le i \le N-1}}{\arg\min} \sum_{k=1}^{N} \left\| R_v^{-1/2}\big(y_c(k) - Cx(k)\big) \right\|_2^2$$

$$+ \lambda \sum_{k=1}^{N-1} \alpha_l(k) \left\| R_F^{-1/2} F(k) \right\|_1$$

$$+ \sum_{k=1}^{N-1} \left\| R_\eta^{-1/2} \eta(k) \right\|_2^2$$

(3.6)

s.t. $x(k+1) = Ax(k) + Bu_c(k) + BF(k) + H\eta(k)$.

2. Set

$$\alpha_{l+1}(k) = \big(\epsilon + \left\| R_F^{-1/2} \hat{F}_l(k) \right\|_1\big)^{-1}$$

(3.7)

where ϵ is a positive tuning parameter. Increase the iteration number $l = l + 1$ and return to step 1.

After convergence, a final estimate of the magnitude of the pulses can be found using

$$[\hat{x}_{l+1}(1), \hat{F}_{l+1}(k), \hat{\eta}_{l+1}(k)] =$$

$$\underset{\substack{x(1), F(i), \eta(i) \\ 1 \le i \le N-1}}{\arg\min} \sum_{k=1}^{N} \left\| R_v^{-1/2}\big(y_c(k) - Cx(k)\big) \right\|_2^2$$

$$+ \sum_{k=1}^{N-1} \left\| R_\eta^{-1/2} \eta(k) \right\|_2^2$$

(3.8)

s.t. $x(k+1) = Ax(k) + Bu_c(k) + BF(k) + H\eta(k)$
$$F(k) = 0 \ \text{ if } \ k \notin \mathcal{T}$$

with $\mathcal{T} = \{k | \hat{F}_l(k) \ne 0\}$.

The new parameters introduced in (3.6) have the following definitions. The quantity λ is a tuning parameter, $\alpha_l(k)$ is a variable weighting vector to enhance convergence and R_F is the estimated variance of $F(k|F(k) \neq 0)$. The 1-norm in (3.6) and (3.7) is used to enhance sparsity. Ohlsson *et al.* described a non-iterative procedure for finding an appropriate λ [[18], eqs. (25)-(28)], though we found in the simulation experiments that additional tuning is useful.

Although the minimization in (3.6) is convex due to the use of the 1-norm instead of the 0-norm, the disadvantage is estimates $\hat{F}_l(k)$ being biased towards zero. The concluding convex minimization (3.8) corrects this bias using the time instances at which the estimates of $\hat{F}_l(k)$ in (3.6) of the latest iteration are nonzero[1]. Thus, the STATESON-algorithm utilizes only convex minimizations, which makes it computationally attractive.

Furthermore, optimization problem (3.6) can be rewritten to a general 'lasso' form [20] by substituting $\eta(k)$ in the objective function and rearranging it to

$$\hat{\psi}_l = \arg\min_{\psi} \|\Phi^{-1}(\Gamma\psi - \varphi)\|_2^2 + \lambda\|\Xi_l\psi\|_1 \tag{3.9}$$

where

$$\Phi^{-1} = \begin{bmatrix} R_v^{-1/2} & 0 & 0 & \cdots \\ 0 & R_\eta^{-1/2} & 0 & \cdots \\ 0 & 0 & R_v^{-1/2} & \\ \vdots & \vdots & & \ddots \end{bmatrix},$$

$$\Gamma = \begin{bmatrix} C & 0 & 0 & 0 & 0 & \cdots \\ -A & -B & I & 0 & 0 & \cdots \\ 0 & 0 & C & 0 & 0 & \\ 0 & 0 & -A & -B & I & \\ \vdots & \vdots & & & & \ddots \end{bmatrix},$$

$$\Xi_l = \begin{bmatrix} 0 & R_F^{-1/2}\alpha_l(1) & 0 & 0 & \cdots \\ 0 & 0 & 0 & R_F^{-1/2}\alpha_l(2) & \\ \vdots & \vdots & & & \ddots \end{bmatrix},$$

$$\psi = \begin{bmatrix} x(1) \\ F(1) \\ x(2) \\ F(2) \\ \vdots \end{bmatrix}, \text{ and } \varphi = \begin{bmatrix} y_c(1) \\ Bu_c(1) \\ y_c(2) \\ Bu_c(2) \\ \vdots \end{bmatrix}.$$

Optimization problems in the 'lasso' form as in (3.9) can be solved efficiently, for instance using FISTA [21].

Likewise, optimization problem (3.8) can be rewritten to an unconstrained least-squares problem

$$\hat{\psi}_{\text{LS}} = \arg\min_{\psi_{\text{LS}}} \|\Phi^{-1}(\Gamma_{\text{LS}}\psi_{\text{LS}} - \varphi)\|_2^2 \tag{3.10}$$

---

[1]In practice, the set $\mathcal{T} = \{k|\hat{F}_l(k) > \varepsilon\}$ will be used, with ε a small number, so that very small values in $\hat{F}_l(k)$ are set to zero.

where Γ_{LS} and ψ_{LS} are constructed similarly to those in (3.9), though omitting the columns of Γ and rows of ψ corresponding to the zero estimated t/s-interactions $\hat{F}_l(k|\hat{F}_l(k) = 0)$. The solution to this problem can be found analytically [22].

The cantilever deflection can be reconstructed using

$$\hat{y}_{\text{SBR}}(k) = C\hat{x}(k). \tag{3.11}$$

Note that the smoothed states are directly available as outcome of the optimization problem (3.10), as opposed to (3.5) in which the states need to be reconstructed using previous states and estimates of the t/s-interaction.

3.2.3. FROM T/S-INTERACTION TO SAMPLE HEIGHT

The idea in [16] was to use the estimated t/s-interaction as input for the controller. In this chapter, the goal is to estimate the sample height as accurate as possible at high scan speeds, rather than only the t/s-interaction. Moreover, the sample height is in our perspective the most appropriate input signal to the controller and the ultimate information to be obtained. Various models exist for converting the t/s-interaction to distance between tip and sample, such as the Hertzian, the Derjaguin-Müller-Toporov and the Johnson-Kendall-Roberts model [23]. Unfortunately, each model requires knowledge of several parameters of both tip and sample [23, 24], which are in addition likely to vary spatially for biological samples. Hence, those models will not be used.

To make the height reconstruction generally applicable, it is estimated for each oscillation period

$$\left(i - \frac{1}{2}\right) T \le kT_s < \left(i + \frac{1}{2}\right) T$$

using the minimum of the estimated cantilever deflection:

$$\hat{h}(i) = \min_k \left(\hat{y}(k)\right) - \hat{z}(i). \tag{3.12}$$

Naturally, the estimated table height $\hat{z}(i)$ is subtracted from the minimum cantilever deflection in order to arrive at the sample height. Accordingly, the estimated table height captures the coarse height profile and the minimum cantilever deflection term captures the finer variations in height.

3.3. EXPERIMENTAL DESIGN

The discussed methods will be tested in two simulation studies. A first simulation tests the methods for a one-dimensional scan with two steps of height 1 nm. The second simulation experiment comprises a scan of a 24-nm×24-nm-sized grating consisting of discrete steps of height 1 nm. The sample is scanned with a cantilever tip radius of 1 nm, from left to right in 20 scan lines with scan speeds varying from 2 to 200 μm/s.

Signals A_c, u_z, z, $\hat{z}$ and $\hat{h}$ in Fig. 3.1(a) are sampled for each cantilever oscillation period $1/T = 400$ kHz, whereas the other signals are sampled with rate $1/T_s = 10$ MHz.

A piece-wise linear force-distance curve is used to simulate the tip-sample interaction. If the distance between tip and sample is smaller than 0 (*i.e.* the tip is intruding the sample), then the interaction is proportional to the depth of the tip in the sample with factor 1.6 nm^{-1}, otherwise there is no interaction.

For the cantilever immersed in liquid, a second-order model is used, identified from experimental data obtained from an SS-NEX Ando model AFM. The cantilever dynamics are identified by processing its thermal motion ($y_c(k)$ with input $u_c(k) = 0$) in a subspace identification algorithm [22, 25]. This yielded a resonance frequency of 552 kHz, quality factor 1.59 and steady-state gain 6.59 dB. The input of the cantilever $u_c(k)$ is a sinusoid with frequency $1/T = 400$ kHz such that the cantilever's free oscillation amplitude is ca. 2.15 nm. The thermal noise and measurement noise are inspected from measurement data and valued as $R_\eta = 0.0033$ and $R_v = 0.0151$.

The LIA is simulated using [[26], eq. (2), (3), (8)]. The input $y_c(k)$ is mixed with reference signals $\cos(2\pi k T_s/T)$ and $\sin(2\pi k T_s/T)$. The resulting signals are fed to a fourth-order Butterworth low-pass filter. As the output of the LIA is sampled each oscillation period of the cantilever T, the Butterworth filter should filter out all frequencies higher than the Nyquist frequency $1/(2T)$ Hz and therefore, the cutoff frequency of the filter is chosen as $2/(5T)$ Hz.

The z-piezo is modeled as an all-pole second-order transfer function with resonance frequency $\omega_z = 40000 \times 2\pi$ and damping coefficient $\zeta_z = 0.5$. For simplicity, the steady-state gain of this model is unity, such that scaling of u_z in Fig. 3.1(a) is unnecessary before combining it with A_{ref}. A PI-controller regulating the table height is empirically designed with proportional and integral gains $k_p = 0.1$ and $k_i = 7.5 \times 10^4$. The setpoint oscillation amplitude of the cantilever is $A_{\text{ref}} = 1.6$ nm.

The parameters of the KFF-approach are chosen as follows. The variance $R_\delta = 30$: lower values result in a slower transient of the nonzero elements in $F(k)$ whereas higher values do not affect the solution significantly. The variance of $\gamma(k)$ is chosen to be $R_\gamma = 0.0012$ and the length of vector $\theta(k)$ is chosen as constant 5 (implying $T_d = 5T - T_s$). A smaller length of $\theta(k)$ results in a nonconverged estimate, whereas the choice of a larger vector does not affect the solution significantly. The initial conditions are chosen as $P(1|0) = I_5$ and $\hat{\theta}(1|0) = \begin{bmatrix} 0 & 0 & 0 & 0 & 0 \end{bmatrix}^\top$. Since T is in our case not necessarily an integer multiple of T_s, the pulse occurrences are chosen to be a fixed number of time steps before the input crosses 0 with positive derivative.

The SBR-approach is implemented with the following parameters. The variance of the t/s-interaction is $R_F = 10^{-2}$, tuning parameter $\lambda = 1$, the weighing factor $\alpha_1(k) = 1$ $\forall k$ and the threshold value is $\varepsilon = 0.01$. In the simulation we restricted the algorithm to the first step (3.6) followed by (3.8) only. The overall problem is split into parts of 300 data points to prevent computational overload, and solved using FISTA [21, 27].

3.4. RESULTS

Fig. 3.1(b-f) presents the results of the first simulation experiment. From the noisy measured cantilever deflection in Fig. 3.1(b), the tip-sample interaction is reconstructed in Fig. 3.1(b,c). Fig. 3.1(c) reveals the difference between KFF and SBR. The KFF-approach is restricted to $\hat{F}(k)$ to be nonzero for one single value of k within

one cantilever oscillation period. On the contrary, $\hat{F}(k)$ determined in SBR may be nonzero at more time instances. This results in Fig. 3.1(e) in better reconstruction of the cantilever deflection using SBR than using KFF, which is confirmed by the residuals in Table 3.1.

Note that the residual of measured cantilever deflection $\text{Var}(y_{\text{real}} - y_c)$ (approximated by R_v) has a magnitude in between that of SBR and KFF. This gives rise to the idea to apply (3.12) with $\hat{y}(k)$ replaced by the raw measurement data $y_c(k)$, meaning that in Fig. 3.1(a) the blocks "SBR" and "KFF" are bypassed to directly advance to the height estimation block representing (3.12). This additional approach will be evaluated in the second simulation experiment under the name Minimum of Raw Measurements (MRM).

Fig. 3.2 presents images resulting from the second simulation experiment. In a slow scan, all methods are able to recover the sample height accurately up to the effect of nonzero tip radius, with SBR and MRM slightly more noisy than the conventional method and KFF. For higher scan speeds, the proposed methods seem to increase only in noise, whereas the existing two methods show image artifacts due to slow response of LIA and controller. The computational time of the SBR method to evaluate all t/s-interactions in Fig. 3.2 with scan speed 200 μm/s (consisting of 48 000 data points), was 7.50 seconds using Matlab R2021a on an Intel i7-9750H CPU. This is slightly larger than that of KFF, but improves the performance significantly. Fig. 3.3 shows the sample height reconstruction performances for increasing scan speeds quantitatively.
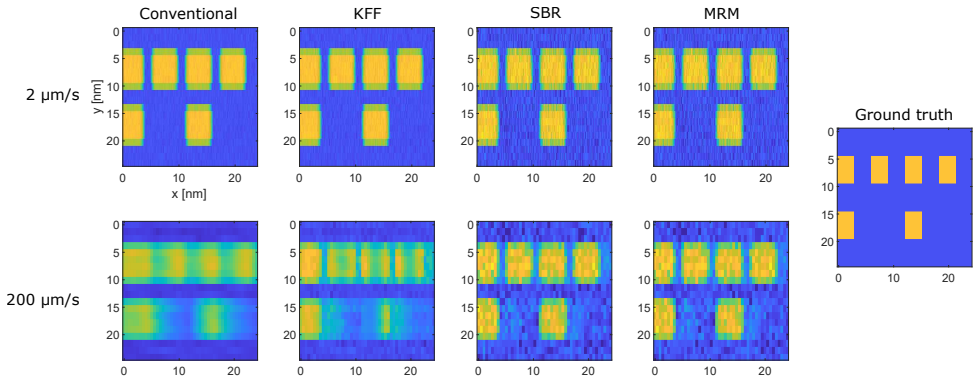
Figure 3.2: Simulations of a 24 nm×24 nm sample scan with steps in height of 1 nm, using a drive frequency of the cantilever of 400 kHz and 20 scan lines. The columns from left to right: the ground truth, the conventional approach ($-u_z$), KFF, SBR, and MRM. A slow scan of 2 μm/s (top) and a fast scan of 200 μm/s (bottom). © 2023 IEEE.

Table 3.1: Residuals of estimated cantilever deflection at scan speed 200 μm/s. © 2023 IEEE.

Approximation method	Var($y_{\text{real}} - \hat{y}$)	Comp. time (s)
KFF ($\hat{y} = \hat{y}_{\text{KFF}}$)	0.0944	1.87
SBR ($\hat{y} = \hat{y}_{\text{SBR}}$)	0.0089	7.50
Raw measurements ($\hat{y} = y_c$)	0.0150	-
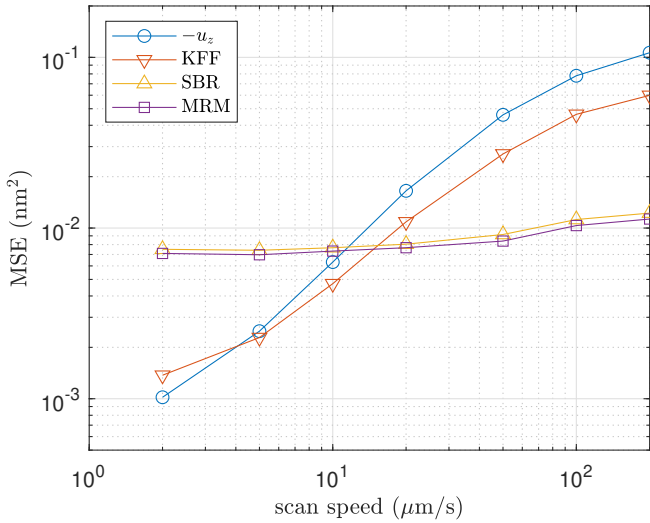
Figure 3.3: Mean-Squared Errors (MSEs) of sample height reconstruction against scan speed. The conventional method (blue circle), KFF (red, down-pointing triangle), SBR (yellow, up-pointing triangle) and the MRM (purple, square). © 2023 IEEE.

Table 3.2: Significance between SBR and MRM by Mann–Whitney–Wilcoxon approximated p-values. © 2023 IEEE.

Scan speed (μm/s)	p-value
2	0.0965
5	0.2108
10	0.4359
20	0.2437
50	0.1682
100	0.6114
200	0.2678

3.5. DISCUSSION

The results in Fig. 3.3 confirm the observation from Fig. 3.2 that the conventional method and KFF perform better for lower scan speeds. As expected, for higher scan speeds the SBR-method and MRM produce a lower mean-squared error (MSE). The KFF-approach has a performance curve similar to that of the conventional approach for the reason that it has large dependency on the scanner height, as can be seen in Fig. 3.1(e,f). It performs slightly better than the conventional approach for being able to reconstruct sharper edges in the sample, as seen in the fast scan in Fig. 3.2. The SBR-method and MRM also have a similar curve. Moreover, the Mann-Whitney-Wilcoxon approximated p-values between these methods in Table 3.2 (calculated over the squared errors in sample height estimation) show weak significance with $p > 0.05$, whereas other approaches differ with stronger significance with p-value < 0.05. Remarkably, MRM and SBR produce similar MSE for sample height reconstruction, whereas SBR has lower residual in cantilever deflection reconstruction as was shown in Table 3.1. The reason for this contradiction could be that the minimum cantilever deflection typically occurs at time instances at which $\hat{F}(k)$ is nonzero. As subsequent elements in $\hat{F}(k)$ can be nonzero, it can fully compensate the measurement noise $v(k)$ at time instances around the minimum deflection, or even worse: it compensates the noise with errors. It is expected that the last-mentioned scenario occurred in this simulation. As the minimum estimated cantilever deflection determines the sample height, the image degrades in this scenario. This effect will be smaller for sparser t/s-interactions, which can be realized using a larger reference amplitude A_{ref} for gentler tapping or a higher quality factor of the cantilever.

3.6. CONCLUSION

The proposed novel approach for sample height reconstruction for high-speed AFM demonstrates accurate recovery of tip-sample interaction and practically eliminates unwanted artifacts. Using the STATESON-algorithm, the SBR approach outperforms the most promising algorithm previously used in high-speed tapping mode AFM. Moreover, the STATESON-algorithm is a convex relaxation for recovering abrupt disturbances and not restricted to fixed time instances for identifying impulses. After recovering the tip-sample interaction, the sample height is determined using minimum smoothed cantilever deflection per cantilever oscillation period. Simulations show the ability to recover sharp edges in the sample, unlike the conventional approach.

In current simulation settings, the minimum of the raw cantilever deflection measurements provided unexpectedly a sample height reconstruction performance similar to that of SBR. Therefore we advise to use non-processed cantilever deflection for estimating the sample height. Additionally, the SBR is pragmatic for providing insight in interactions during operation.

Future research should focus on implementing SBR as a filter, such that real-time sample height and interaction estimates form a reference for the scanner or can be used to control the cantilever excitation signal. Besides, it is recommended

to find a procedure to tune the parameters involved in SBR automatically. This may for instance be done by optimizing the image resolution using Fourier ring correlation [28]. The computational time may be further decreased depending on the computing platform and code optimization, for instance by exploiting the sparsity and redundancy of the matrices involved in the optimization problems.

3

REFERENCES

[1] J. Noom, C. Smith, G. J. Verbiest, A. J. Katan, O. Soloviev, and M. Verhaegen. "High-Speed Tapping Mode AFM Utilizing Recovery of Tip-Sample Interaction". In: *IEEE Transactions on Nanotechnology* 22 (2023), pp. 273–279. DOI: 10.1109/TNANO.2023.3284654.

[2] J. Noom. *Matlab code for HS-AFM utilizing recovery of tip-sample interaction.* 2024. DOI: 10.5281/zenodo.10454091.

[3] G. Binnig, C. F. Quate, and C. Gerber. "Atomic Force Microscope". In: *Physical Review Letters* 56.9 (1986), pp. 930–933. DOI: 10.1103/PhysRevLett.56.930.

[4] N. Kodera, D. Yamamoto, R. Ishikawa, and T. Ando. "Video imaging of walking myosin V by high-speed atomic force microscopy". In: *Nature* 468.7320 (2010), pp. 72–76. DOI: 10.1038/nature09450.

[5] T. Uchihashi, N. Kodera, and T. Ando. "Guide to video recording of structure dynamics and dynamic processes of proteins by high-speed atomic force microscopy". In: *Nature Protocols* 7.6 (2012), pp. 1193–1206. DOI: 10.1038/nprot.2012.047.

[6] T. Ando. "High-speed atomic force microscopy coming of age". In: *Nanotechnology* 23.6 (2012), p. 062001. DOI: 10.1088/0957-4484/23/6/062001.

[7] Y. F. Dufrêne, T. Ando, R. Garcia, D. Alsteens, D. Martinez-Martin, A. Engel, C. Gerber, and D. J. Müller. "Imaging modes of atomic force microscopy for application in molecular and cell biology". In: *Nature Nanotechnology* 12.4 (2017), pp. 295–307. DOI: 10.1038/nnano.2017.45.

[8] J. M. Eeftens, A. J. Katan, M. Kschonsak, M. Hassler, L. de Wilde, E. M. Dief, C. H. Haering, and C. Dekker. "Condensin Smc2-Smc4 Dimers Are Flexible and Dynamic". In: *Cell Reports* 14.8 (2016), pp. 1813–1818. DOI: 10.1016/j.celrep.2016.01.063.

[9] F. Jiao, K. S. Cannon, Y.-C. Lin, A. S. Gladfelter, and S. Scheuring. "The hierarchical assembly of septins revealed by high-speed AFM". In: *Nature Communications* 11.1 (2020). DOI: 10.1038/s41467-020-18778-x.

[10] G. R. Heath, E. Kots, J. L. Robertson, S. Lansky, G. Khelashvili, H. Weinstein, and S. Scheuring. "Localization atomic force microscopy". In: *Nature* 594.7863 (2021), pp. 385–390. DOI: 10.1038/s41586-021-03551-x.

[11] D. R. Sahoo, A. Sebastian, and M. V. Salapaka. "Transient-signal-based sample-detection in atomic force microscopy". In: *Applied Physics Letters* 83.26 (2003), pp. 5521–5523. DOI: 10.1063/1.1633963.

[12]   A. Willsky and H. Jones. "A generalized likelihood ratio approach to the detection and estimation of jumps in linear systems". In: *IEEE Transactions on Automatic Control* 21.1 (1976), pp. 108–112. DOI: 10.1109/TAC.1976.1101146.

[13]   D. R. Sahoo, P. Agarwal, and M. V. Salapaka. "Transient Force Atomic Force Microscopy: A New Nano-Interrogation Method". In: *American Control Conference*. 2007, pp. 2135–2140. DOI: 10.1109/ACC.2007.4283047.

[14]   G. Mohan, C. Lee, and S. Salapaka. "Control techniques for high-speed dynamic mode imaging in atomic force microscopes". In: *50th IEEE Conference on Decision and Control and European Control Conference*. 2011, pp. 651–656. DOI: 10.1109/CDC.2011.6160734.

[15]   P. Huang and S. B. Andersson. "High speed atomic force microscopy enabled by a sample profile estimator". In: *Applied Physics Letters* 102.21 (2013), p. 213118. DOI: 10.1063/1.4808211.

[16]   K. S. Karvinen, M. G. Ruppert, K. Mahata, and S. O. R. Moheimani. "Direct Tip-Sample Force Estimation for High-Speed Dynamic Mode Atomic Force Microscopy". In: *IEEE Transactions on Nanotechnology* 13.6 (2014), pp. 1257–1265. DOI: 10.1109/TNANO.2014.2360878.

[17]   A. Keyvani, G. van der Veen, M. S. Tamer, H. Sadeghian, H. Goosen, and F. van Keulen. "Real-Time Estimation of the Tip-Sample Interactions in Tapping Mode Atomic Force Microscopy With a Regularized Kalman Filter". In: *IEEE Transactions on Nanotechnology* 19 (2020), pp. 274–283. DOI: 10.1109/TNANO.2020.2974177.

[18]   H. Ohlsson, F. Gustafsson, L. Ljung, and S. Boyd. "Smoothed state estimates under abrupt changes using sum-of-norms regularization". In: *Automatica* 48.4 (2012), pp. 595–605. DOI: 10.1016/j.automatica.2011.08.063.

[19]   K. J. Åström and B. Wittenmark. *Computer-controlled systems: Theory and design*. 3rd ed. Mineola, NY, USA: Dover Publications, 2011. ISBN: 978-0486486130.

[20]   R. Tibshirani. "Regression Shrinkage and Selection Via the Lasso". In: *Journal of the Royal Statistical Society: Series B (Methodological)* 58.1 (1996), pp. 267–288. DOI: 10.1111/j.2517-6161.1996.tb02080.x.

[21]   A. Beck and M. Teboulle. "A Fast Iterative Shrinkage-Thresholding Algorithm for Linear Inverse Problems". In: *SIAM Journal on Imaging Sciences* 2.1 (2009), pp. 183–202. DOI: 10.1137/080716542.

[22]   M. Verhaegen and V. Verdult. *Filtering and System Identification: A Least Squares Approach*. Cambridge: Cambridge University Press, 2007. ISBN: 978-1107405028.

[23]   M. Kopycinska-Müller, R. H. Geiss, and D. C. Hurley. "Contact mechanics and tip shape in AFM-based nanomechanical measurements". In: *Ultramicroscopy* 106.6 (2006), pp. 466–474. DOI: 10.1016/j.ultramic.2005.12.006.

[24]   R. García and A. San Paulo. "Attractive and repulsive tip-sample interaction regimes in tapping-mode atomic force microscopy". In: *Phys. Rev. B* 60.7 (1999), pp. 4961–4967. DOI: 10.1103/PhysRevB.60.4961.

[25] J. Noom. "Detection of Tip-Sample Interaction in Atomic Force Microscopy: Improving the Image Resolution". MA thesis. Delft University of Technology, 2019.

[26] S. DeVore, A. Gauthier, J. Levy, and C. Singh. "Development and evaluation of a tutorial to improve students' understanding of a lock-in amplifier". In: *Physical Review Physics Education Research* 12.2 (2016), p. 020127. DOI: 10.1103/PhysRevPhysEducRes.12.020127.

[27] T. Vu and P. State. *FISTA*. https://github.com/tiepvupsu/FISTA. 2016.

[28] N. Banterle, K. H. Bui, E. A. Lemke, and M. Beck. "Fourier ring correlation as a resolution criterion for super-resolution microscopy". In: *Journal of Structural Biology* 183.3 (2013), pp. 363–367. DOI: 10.1016/j.jsb.2013.05.004.

3

4

ONLINE MODEL-FREE DATA-DRIVEN FAULT DIAGNOSIS

We present a novel problem formulation for model-free data-driven fault diagnosis, in which possible faults are diagnosed simultaneously to identifying the linear time-invariant system. This problem is practically relevant for systems whose model cannot be identified reliably prior to diagnosing possible faults, for instance when operating conditions change over time, when a fault is already present before system identification is carried out, or when the system dynamics change due to the presence of the fault. A computationally attractive solution is proposed by solving the problem using unconstrained convex optimization, where the objective function consists of three terms of which two are non-differentiable. An additional recursive implementation based on a proximal algorithm is presented in order to solve the optimization problem online. The numerical results on a buck converter show the application of the proposed solution both offline and online.

4.1. INTRODUCTION

With the increase of complexity of automated systems, timely and accurate fault diagnosis is essential for preventing catastrophic failures. Accordingly, fault detection and identification has recently been considered within the top-three of control technologies with high future impact in industrial applications [4]. Whereas model-based and signal-based methods [5] require human expertise on modeling of the specific system or designing its characteristic signal shapes, knowledge-based methods rely on identifying the system and the possible faults from past data [6, 7]. This makes knowledge-based fault diagnosis attractive specifically for large-scale industrial systems for which modeling is burdensome.

For its use of large amounts of historical data, knowledge-based fault diagnosis is often referred to as *data-driven* [6, 8–11]. However, it can effectively be partitioned in a (data-based) model acquisition phase and a model-based fault diagnosis phase. Especially in the first phase reliable and often also labeled data is required. In complex industrial applications this is not always available, or it is desired to diagnose faults directly from the first operational run of the unidentified system. Moreover, the main limitation of existing fault diagnosis techniques is that predetermined features or predetermined models lack the capability of accommodating for changing input/output dynamics for example due to changes in the internal system dynamics or in the environment.

The main contribution of this chapter is threefold. First, a formulation for the problem of *model-free data-driven fault diagnosis* is presented. Different from existing categories for fault diagnosis which assume separate time periods for system modeling/identification and fault diagnosis, this novel formulation includes the goal of both retrieving the system dynamics and diagnosing the faults *simultaneously*. With a fixed data window, the diagnosis involves both the determination of the active faults from a set of hypothesized faults (fault isolation) and of their corresponding sizes (fault identification). The system dynamics are assumed to be Linear and Time-Invariant (LTI) over the considered data window. The proposed problem differs from the one formulated in [12], where only the presence of a fault in an unknown LTI system is to be detected. Instead, model-free data-driven fault diagnosis focuses on fault isolation and identification, simultaneously to retrieving an up-to-date model of the system.

The second contribution of this chapter proposes to use our earlier developed solution [13] to the problem of model-free data-driven fault diagnosis. By reformulating the problem as a convex optimization problem, the proposed solution is computationally attractive. As in [14] a dictionary of hypothesized faults is constructed, after which sparsity is employed by the natural assumption that only a few of the hypothesized faults are concurrently active. The model-based approach in [14] however assumes the availability of a predetermined model of the system. In the proposed solution for model-free data-driven fault diagnosis such a predetermined model is not required, but is identified simultaneously to diagnosing the faults. The simultaneous goal is achieved using results from the field of blind system identification [15], which aims for identifying a system with unknown inputs. Different from [15], the proposed solution in this chapter considers multiple

non-differentiable optimization terms in order to apply it to model-free data-driven fault diagnosis. Hereby this contribution establishes a link between blind system identification and model-free data-driven fault diagnosis. In addition to our earlier work [13], conditions are introduced on the identifiability and diagnosability of the system and faults, respectively.

The third contribution of this chapter is to propose a fast recursive implementation for solving the convex but non-differentiable optimization problem, enabling online monitoring including fault detection, isolation, fault identification and simultaneous system identification. The recursive implementation allows the unknown system dynamics and active faults to change over time, while being identified and diagnosed in real-time. Whereas the recursive approaches in [10] are limited to fault detection only and require an initial model of sufficient quality, our approach is fully model-free and is able to isolate and identify the faults in addition to detection. The proposed recursive implementation of model-free data-driven fault diagnosis relies on the proximal operators [16, 17] of the objective terms, of which closed-form solutions are available. Using efficient updates of the proximal operators, an established proximal algorithm [18] is implemented recursively. Different from recursive implementation of subgradient methods such as in [19], the proposed proximal-based implementation does not involve fragile restrictions on tuning parameters for guaranteeing convergence. Other recursive implementations of proximal algorithms [20, 21] are only able to cope with one non-differentiable objective term (or multiple terms only if the problem is block-separable), whereas the proposed approach can handle multiple non-differentiable objective terms even if the problem is not block-separable.

The chapter is organized as follows. Sect. 4.2 presents the novel problem formulation. Sect. 4.3 presents the methodology for model-free data-driven fault diagnosis, starting with Sect. 4.3.1 introducing the structured data matrices and Sect. 4.3.2 recapping the method of [14] for model-based fault diagnosis, neglecting the effect of the initial state. This negligence is based on developments in subspace identification [22, 23]. The proposed data-driven approach to fault diagnosis is presented in Sect. 4.3.3 with conditions on identifiability and diagnosability in Sect. 4.3.4. For the resulting convex optimization problem, Sect. 4.4 demonstrates the adoption of a proximal algorithm. Subsequently, Sect. 4.5 shows how the proximal algorithm can be implemented recursively in order to achieve online monitoring. The proposed methodology is tested numerically on a buck converter electronic circuit in Sect. 4.6 and conclusions are drawn in Sect. 4.7.

4.2. PROBLEM FORMULATION

Consider the following linear time-invariant system

$$
\begin{aligned}
x(k+1) &= Ax(k) + Bu(k) + Fd(k) + w(k) \\
y(k) &= Cx(k) + v(k)
\end{aligned}
\tag{4.1}
$$

with $x(k) \in \mathbb{R}^{n_x}$, $u(k) \in \mathbb{R}^{n_u}$, $d(k) \in \mathbb{R}^{n_d}$ and $y(k) \in \mathbb{R}^{n_y}$ the state, input, fault signal and output; A, B, C and F the state-space matrices; and $w(k)$ and $v(k)$ the process and

measurement noise, respectively. The fault signal

$$d(k) = \theta(k)z \tag{4.2}$$

is constructed from a known dictionary $\theta(k) \in \mathbb{R}^{n_d \times n_z}$ consisting of possible fault signal shapes and an unknown weighing vector $z = [z_1, \ldots, z_{n_z}]^\top \in \mathbb{R}^{n_z}$ which determines the active faults and their severity. Typically only a few faults out of the set of possible faults are active simultaneously.

With $\Phi = A - KC$, consider the observer [23] for system (4.1):

$$\begin{aligned} \hat{x}(k+1) &= \Phi\hat{x}(k) + Bu(k) + F\theta(k)z + Ky(k) \\ \hat{y}(k) &= C\hat{x}(k) \end{aligned} \tag{4.3}$$

with estimated state $\hat{x}(k)$ and estimated output $\hat{y}(k)$. Using this model, we can write the estimated output $\hat{y}(k)$ as:

$$\begin{aligned} \hat{y}(k) = {}& C\Phi^s \hat{x}(k-s) \\ &+ \sum_{i=1}^{s} C\Phi^{i-1} \Big(Bu(k-i) + F\theta(k-i)z + Ky(k-i) \Big) \end{aligned} \tag{4.4}$$

If the system is detectable and K is designed such that Φ is asymptotically stable, the effect of the state $\hat{x}(k-s)$ decreases to zero for increasing s. This leads to the following approximate Vector Auto-Regressive model with eXogenous input (VARX):

$$\hat{y}(k) \approx \sum_{i=1}^{s} B_i u(k-i) + F_i \theta(k-i)z + K_i y(k-i). \tag{4.5}$$

The matrices B_i, F_i and K_i of compatible size refer to the so-called observer Markov parameters [24]. The VARX model description covers a wide range of multiple-input multiple-output (MIMO) systems and is studied comprehensively in [22, 25]. It is identifiable in the sense that every unique set of VARX parameters leads to a unique output given that the input is persistently exciting [26].

First we formulate the problem for model-based Fault Diagnosis (FD).

Problem 4.1 (Model-based FD). *Given the VARX parameters B_i, F_i and K_i in (4.5), input $u(k)$ and output $y(k)$ sequences and the corresponding fault dictionary $\theta(k)$, isolate the faults as the nonzero elements in the unknown vector z, together with their corresponding sizes.*

The problem for model-based FD within this formulation has been widely studied both for time-invariant and time-varying systems (see e.g. [27–29]). Alternatively, knowledge-based (also called data-driven) FD consists of an extra preceding phase, formulated as follows.

Problem 4.2 (Data-driven FD). *Given the input $u(k)$ and output $y(k)$ sequences and the corresponding fault dictionary $\theta(k)$ with the true weights z, first identify the system characteristics in a training phase with known faults. Afterwards, diagnosis can be performed in a subsequent phase where the faults are unknown. Based on the*

identified system characteristics and given the input u(k) and output y(k) sequences and the corresponding fault dictionary θ(k), isolate the faults as the nonzero elements in the unknown vector z, together with their corresponding sizes.

Some well-known approaches for solving the data-driven FD problem for dynamical systems are summarized in [6, 9, 10]. These approaches require separate time periods for system identification prior to the fault diagnosis experiment. However, the system dynamics may already have changed in between the system identification and the fault diagnosis experiment, or for some applications it is not even possible to perform system identification due to costly data acquisition prior to productive system operation. In such cases it is desirable to perform fault diagnosis without requiring a previously identified model. This problem is formulated below.

Problem 4.3 (Model-free data-driven FD). *Given the input u(k) and output y(k) sequences and the corresponding fault dictionary θ(k), simultaneously identify the system characteristics and isolate the faults as the nonzero elements in the unknown vector z, together with their corresponding sizes.*

Problems 4.1, 4.2 and 4.3 are visualized in Fig. 4.1. Naturally, the problem for model-free data-driven FD imposes some assumptions on system observability, the input sequence and the fault dictionary. The assumptions on input sequence and the fault dictionary will be stipulated in Sect. 4.3.4.

a) Model-based FD

$d(k) = \theta(k)z$

$u(k)$ → Known system → $y(k)$

b) Data-driven FD

$d(k) = \theta(k)z$

$u(k)$ → Identified system → $y(k)$

Past data

c) Model-free data-driven FD

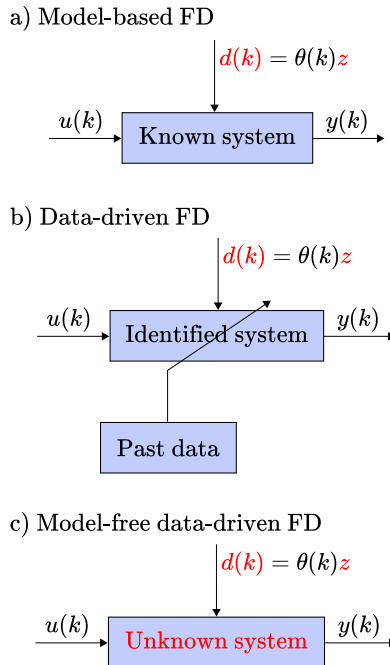$d(k) = \theta(k)z$

$u(k)$ → Unknown system → $y(k)$

Figure 4.1: a) Model-based, b) data-driven and c) model-free data-driven FD.

In the methodology we will make use of the following matrix norm notation. The Frobenius norm is defined as $\|X\|_F = \sqrt{\sum_{i,j} |x_{ij}|^2}$, the $(1,1)$-norm as $\|X\|_{1,1} = \sum_{i,j} |x_{ij}|$ and the nuclear norm as $\|X\|_* = \sum_i \sigma_i(X)$, where x_{ij} are the (i,j)th elements of the matrix X, and $\sigma_i(X)$ the ith singular value.

4.3. Model-free data-driven fault diagnosis

4.3.1. VARX model identification

To introduce the structured data matrices, we first consider the fault-free identification problem with $d(k) = 0$. It should be noted that this fault-free identification step is not required for the execution of the proposed approach introduced later, however essential for building up the relevant knowledge.

Regard the available information

$$\begin{bmatrix} u(k) & u(k+1) & \ldots & u(k+N-1) \end{bmatrix},$$
$$\begin{bmatrix} y(k) & y(k+1) & \ldots & y(k+N) \end{bmatrix}.$$

Then with

$$Y = \begin{bmatrix} y^\top(k+s) \\ y^\top(k+s+1) \\ \vdots \\ y^\top(k+N) \end{bmatrix}, \quad \mathbf{B} = \begin{bmatrix} B_1^\top \\ B_2^\top \\ \vdots \\ B_s^\top \end{bmatrix}, \quad \mathbf{K} = \begin{bmatrix} K_1^\top \\ K_2^\top \\ \vdots \\ K_s^\top \end{bmatrix}, \tag{4.6}$$

and the Toeplitz matrices

$$T_u = \begin{bmatrix} u^\top(k+s-1) & u^\top(k+s-2) & \ldots & u^\top(k) \\ u^\top(k+s) & u^\top(k+s-1) & \ldots & u^\top(k+1) \\ \vdots & \vdots & \ddots & \vdots \\ u^\top(k+N-1) & u^\top(k+N-2) & \ldots & u^\top(k+N-s) \end{bmatrix}$$

$$T_y = \begin{bmatrix} y^\top(k+s-1) & y^\top(k+s-2) & \ldots & y^\top(k) \\ y^\top(k+s) & y^\top(k+s-1) & \ldots & y^\top(k+1) \\ \vdots & \vdots & \ddots & \vdots \\ y^\top(k+N-1) & y^\top(k+N-2) & \ldots & y^\top(k+N-s) \end{bmatrix} \tag{4.7}$$

the following least-squares problem aims at finding the system parameters $\mathbf{B}$ and $\mathbf{K}$ for the 1-step ahead predictor:

$$\min_{\mathbf{B},\mathbf{K}} \left\| Y - \begin{bmatrix} T_u & T_y \end{bmatrix} \begin{bmatrix} \mathbf{B} \\ \mathbf{K} \end{bmatrix} \right\|_F^2. \tag{4.8}$$

The solution to this problem is unique if the matrix $\begin{bmatrix} T_u & T_y \end{bmatrix}$ has full column rank. This condition requires the input to be persistently exciting [23] and leads to identifiability of the system as in Definition 4.1.

4.3.2. MODEL-BASED FAULT DIAGNOSIS UNDER SPARSENESS ASSUMPTION

Suppose now that the fault signal $d(k)$ is nonzero and composed as in (4.2), and the system matrices A, B, C, F and K are known. Whereas [14] indicates for conventional approaches that "tractable solutions are only available when a small number of possible faults are assumed," recently he proposed a computationally efficient method to diagnose from a large set of possible faults. Neglecting the effects of initial condition (given the fact that Φ is asymptotically stable [22, 23]) the approach in [14] can be (accurately) approximated as follows.

Let $\mathbf{F}$ be constructed from F similarly to $\mathbf{B}$ from B in (4.6). Consider the Kronecker product

$$\mathbf{F}(z) = \mathbf{F} \otimes z \tag{4.9}$$

and the Toeplitz matrix T_θ constructed as T_u in (4.7) with all elements $u^\top(k)$ replaced by $\mathrm{vec}(\theta^\top(k))^\top$, such that the VARX approximation becomes

$$Y \approx \begin{bmatrix} T_u & T_\theta & T_y \end{bmatrix} \begin{bmatrix} \mathbf{B} \\ \mathbf{F}(z) \\ \mathbf{K} \end{bmatrix}. \tag{4.10}$$

With the sparseness assumption on z entailing only a small number of faults is active simultaneously, this results in a lasso optimization problem:

$$\min_z \left\| Y - \begin{bmatrix} T_u & T_y \end{bmatrix} \begin{bmatrix} \mathbf{B} \\ \mathbf{K} \end{bmatrix} - T_\theta \mathbf{F}(z) \right\|_F^2 + \lambda \|z\|_1 \tag{4.11}$$

with $\mathbf{F}(z)$ given in (4.9). In words, the output residual is minimized over the fault weighing variables z by subtracting their corresponding fault responses $T_\theta \mathbf{F}(z)$ from the data equation. The 1-norm is included to enhance sparsity on the weighing vector. This approach has shown good performance on both time-invariant and time-variant systems by [14], where also the (negligible) effect of the initial condition is taken into consideration.

4.3.3. MODEL-FREE DATA-DRIVEN APPROACH TO FAULT DIAGNOSIS

In our case of data-driven fault diagnosis the system matrices $\mathbf{B}$, $\mathbf{K}$ and $\mathbf{F}$ are unknown in addition to the fault(s). This implies (4.11) becomes a bilinear optimization problem, which is computationally expensive due to its nonconvexity. However, from the definition of $\mathbf{F}(z)$ it is possible to compose the matrix $\mathbf{F}^*(z)$ as

$$\mathbf{F}^*(z) := \mathrm{vec}\left(\mathbf{F}^\top\right) z^\top \tag{4.12}$$

which has rank one [15]. Besides, the variable $\mathbf{F}(z)$ has by construction in (4.9) a degree of sparsity (defined as the ratio of nonzero components) equal to that of z. As a result, the bilinear optimization problem can be replaced by the rank-constrained

minimization problem

$$
\min_{\mathbf{B},\mathbf{F}(z),\mathbf{K}} \left\| Y - \begin{bmatrix} T_u & T_\theta & T_y \end{bmatrix} \begin{bmatrix} \mathbf{B} \\ \mathbf{F}(z) \\ \mathbf{K} \end{bmatrix} \right\|_F^2 + \lambda \|\mathbf{F}(z)\|_{1,1} \tag{4.13}
$$

$$
\text{s.t. } \operatorname{rank}\!\big(\mathbf{F}^*(z)\big) = 1.
$$

Note that in contrast to (4.11) where z is the optimization variable, in (4.13) the quantity $\mathbf{F}(z)$ is an explicit optimization variable. The solution of $\mathbf{F}$ and z can be found up to a multiplicative scalar from singular value decomposition (SVD) of $\mathbf{F}^*(z)$. Since no model knowledge is assumed, the optimization problem relies on minimizing the output residuals, now with respect to both model parameters as well as fault parameters.

Problem (4.13) can be relaxed to a convex optimization problem by replacing the rank constraint with an additive weighted nuclear norm to the objective function. The eventual unconstrained convex optimization problem is then

$$
\min_{\mathbf{B},\mathbf{F}(z),\mathbf{K}} \left\| Y - \begin{bmatrix} T_u & T_\theta & T_y \end{bmatrix} \begin{bmatrix} \mathbf{B} \\ \mathbf{F}(z) \\ \mathbf{K} \end{bmatrix} \right\|_F^2 + \tau \left\| \mathbf{F}^*(z) \right\|_* \tag{4.14}
$$

$$
+ \lambda \|\mathbf{F}(z)\|_{1,1}.
$$

The faults can be isolated using (4.14) only, however their magnitudes will be biased toward zero due to the additional penalties to the least-squares term. Also, the identified VARX matrices $\mathbf{B}$ and $\mathbf{K}$ may be affected by the bias in $\mathbf{F}(z)$. For refined estimation of the fault magnitudes and system parameters, a second optimization without the 1-norm can be performed over the nonzero estimated elements $\hat{z}$ found in (4.14). In practice, this means that the components of the dictionary $\theta(k)$ and the weighing variables z in (4.2) are in the second optimization neglected according to the 'zero' (in practice below a threshold) elements of $\hat{z}$ found in the first optimization, and in the second optimization $\lambda = 0$.

The choice of the tuning parameters may be nontrivial. However, it can be deduced that a rank one solution is encouraged by increasing τ, and the sparsity of z by increasing λ. A possible tuning strategy is to set λ to zero first and tune τ such that the predictor performance of (4.5) (for instance calculated as Variance Accounted For (VAF)) with parameters found in (4.14) is optimized on a validation data set. While fixing τ to the value found in the first step, λ can be adapted gradually by optimizing the performance of (4.5) on validation data, with parameters found in (4.14) after refinement.

4.3.4. Identifiability & Diagnosability

The model-free data-driven approach to fault diagnosis requires both the system to be identifiable and the faults to be diagnosable.

Definition 4.1 (Identifiability of a system)**.** *A system is regarded to be identifiable if there exists an input sequence such that the variables* **B** *and* **K** *in* (4.14) *can be determined uniquely.*

A sufficient condition for the solution to **B**, **K** and also $\mathbf{F}(z)$ in (4.14) to be unique is that the matrix $\begin{bmatrix} T_u & T_\theta & T_y \end{bmatrix}$ has full column rank. This is now a condition on the persistency of excitation of the joint input $(u^\top(k), \text{vec}(\theta^\top(k))^\top)$. However, due to the regularization terms, full column rank of $\begin{bmatrix} T_u & T_\theta & T_y \end{bmatrix}$ is not a necessary condition for uniqueness of the solution to (4.14). Moreover, with $\begin{bmatrix} T_u & T_y \end{bmatrix}$ full column rank and $\tau = 0$, the solution may still be unique [30]. The fact that $\tau > 0$ in (4.14) further increases the probability of a unique solution. It must be noted that a unique solution does not guarantee diagnosability of each fault, and vice versa.

Definition 4.2 (Diagnosability of a fault)**.** *Given an input/output sequence $u(k)$ and $y(k)$ and a fault dictionary $\theta(k)$, a fault $z_j \neq 0$ is regarded to be diagnosable if all possible solutions to* (4.14) *satisfy $z_j \neq 0$.*

The following lemma states a condition necessary for a fault to be diagnosable.

Lemma 4.1 (Necessary condition for diagnosability)**.** *Consider a fault z_j with its corresponding dictionary signal $\theta_j(k)$. In order for the fault z_j to be diagnosable, it is necessary that at least one column of its corresponding dictionary signal*

$$\begin{bmatrix} \text{vec}(\theta_j^\top(k))^\top \\ \text{vec}(\theta_j^\top(k+1))^\top \\ \vdots \\ \text{vec}(\theta_j^\top(k+N-1))^\top \end{bmatrix}$$

is linearly independent of the columns of

$$\begin{bmatrix} u^\top(k) & y^\top(k) \\ u^\top(k+1) & y^\top(k+1) \\ \vdots & \vdots \\ u^\top(k+N-1) & y^\top(k+N-1) \end{bmatrix}.$$

Proof. In the case of linear dependence, the dictionary signal can be written as

$$\text{vec}(\theta_j^\top(k)) = L_u u(k) + L_y y(k) \tag{4.15}$$

with L_u and L_y time-invariant matrices representing the linear dependence. Then,

$$\left\| Y - \begin{bmatrix} T_u & T_\theta & T_y \end{bmatrix} \begin{bmatrix} \mathbf{B} \\ \mathbf{F}(z) \\ \mathbf{K} \end{bmatrix} \right\|_F^2 =$$

$$\left\| Y - \begin{bmatrix} T_u & T_\theta & T_y \end{bmatrix} \begin{bmatrix} \tilde{\mathbf{B}} \\ \tilde{\mathbf{F}}(z) \\ \tilde{\mathbf{K}} \end{bmatrix} \right\|_F^2 \tag{4.16}$$

where

$$\tilde{\mathbf{B}} = \mathbf{B} + \begin{bmatrix} L_u^\top F_1^\top \\ \vdots \\ L_u^\top F_s^\top \end{bmatrix} z_j, \qquad \tilde{\mathbf{F}}(z) = \mathbf{F} \otimes \begin{bmatrix} z_1 \\ \vdots \\ \tilde{z}_j = 0 \\ \vdots \\ z_{n_z} \end{bmatrix}$$

$$\tilde{\mathbf{K}} = \mathbf{K} + \begin{bmatrix} L_y^\top F_1^\top \\ \vdots \\ L_y^\top F_s^\top \end{bmatrix} z_j,$$

and $(\mathbf{B}, \mathbf{F}(z), \mathbf{K})$ the actual situation with $z_j \neq 0$. With optimization problem (4.14) regularizing on $\mathbf{F}(z)$ but not on $\mathbf{B}$ and $\mathbf{K}$, the global optimum is achieved with $\tilde{z}_j = 0$. Following Definition 4.2, this fault is not diagnosable. ☐

Lemma 4.1 stresses the importance of designing a healthy combination of the fault dictionary, system inputs and outputs. As long as it satisfies Lemma 4.1, possible dictionary signals include sinusoidal, triangular or square waveforms with various frequencies, random Fourier expansions as in [31], unit steps with various starting points, user-defined fault progressions and nonlinear relations of $u(k)$ and/or $y(k)$. Practical examples of hypothesized fault patterns include varying load resistances in a buck converter (as illustrated in Sect. 6) and blockage of air data sensors modeled as additive sinusoidal pressure changes [32].

4.4. ADOPTION OF PROXIMAL ALGORITHM

The data-driven fault diagnosis problem can be recast to a batch optimization problem consisting of $m = 3$ convex but possibly non-differentiable functions f_i:

$$\min_{\mathbf{x}} f(\mathbf{x}) = \min_{\mathbf{x}} \sum_{i=1}^{m} f_i(\mathbf{x}) \tag{4.17}$$

$$= \min_{\mathbf{x}} \frac{1}{2} \|\mathbf{y} - H\mathbf{x}\|_2^2 + \tau \|\mathbf{x}_L\|_* + \lambda \|\mathbf{x}_S\|_1, \tag{4.18}$$

where $\mathbf{y} \in \mathbb{R}^{n_y}$ are the vectorized measurements, $\mathbf{x} \in \mathbb{R}^{n_x}$ the optimization variables with $\mathbf{x}_L$ and $\mathbf{x}_S$ constructed from $\mathbf{x}$ by selecting and rearranging its elements to a low-rank matrix and sparse vector, respectively. For the data-driven fault diagnosis problem, identical elements from $\mathbf{x}$ are selected for constructing both $\mathbf{x}_L$ and $\mathbf{x}_S$.

Problem (4.18) is convex but non-differentiable due to both the nuclear norm and the 1-norm. Therefore, conventional gradient-based algorithms provide limited convergence properties. Alternatively, proximal algorithms have recently shown their potential for solving large-scale non-smooth problems [16, 17].

A proximal algorithm uses proximal operators of the objective terms iteratively in order to solve a convex optimization problem [17]. The proximal operator of a function g is defined as

$$\text{prox}_g(\mathbf{v}) = \arg\min_{\mathbf{x}} \left(g(\mathbf{x}) + \frac{1}{2} \|\mathbf{x} - \mathbf{v}\|_2^2 \right). \tag{4.19}$$

For several specific functions g a closed-form expression for the proximal operator can be derived [16], enabling fast evaluation.

For optimization problems involving a sum of two terms f_i, established proximal algorithms include forward-backward splitting [33], Douglas-Rachford splitting [34] and FISTA [35]. However, the data-driven fault diagnosis problem encompasses three terms of which two are non-differentiable, which in general cannot be handled efficiently by these algorithms. Alternatively, minimization of (4.18) is enabled by multiple-operator splitting schemes, such as the Parallel ProXimal Algorithm (PPXA) [18], generalized forward-backward splitting [36] or the Davis-Yin algorithm [37]. For the small number of tuning parameters, and the convergence being robust against the choice of these tuning parameters, we select PPXA for solving the data-driven fault diagnosis problem. It is reproduced in Algorithm 1.

Algorithm 1 Parallel ProXimal Algorithm (PPXA) [18] for solving (4.17)

Initialization
    $0 < \rho < \infty$ ▷ Scalar step size
    $0 < \omega = [\omega_1, \ldots, \omega_m] \leq 1$ satisfying $\sum_{i=1}^m \omega_i = 1$
    $\Gamma = [\gamma_1, \ldots, \gamma_m] = \rho\omega$
    $\mathbf{x}_0$ ▷ Initial condition
function PPXA($\Gamma, \omega, \mathbf{x}_0$)
    $v_0 : (v_{i,0})_{1 \leq i \leq m} = \mathbf{x}_0$ ▷ Auxiliary variables
    for $j = 0, 1, \ldots, n_p - 1$ **do**   ▷ For n_p iterations
        for $i = 1, \ldots, m$ **do**
            $p_{i,j} = \text{prox}_{\gamma_i f_i}(v_{i,j}) + \varepsilon_{i,j}$ ▷ Error $\varepsilon_{i,j}$
        end for
        $p_j = \sum_{i=1}^m \omega_i p_{i,j}$
        $\xi_j \in]0, 2[$ ▷ Tuning parameter
        for $i = 1, \ldots, m$ **do**
            $v_{i,j+1} = v_{i,j} + \xi_j(2p_j - \mathbf{x}_j - p_{i,j})$
        end for
        $\mathbf{x}_{j+1} = \mathbf{x}_j + \xi_j(p_j - \mathbf{x}_j)$
    end for
end function

In words, PPXA evaluates the proximal operator for the individual terms f_i in parallel, after which the outcomes are averaged and employed in next iteration. Convergence is ensured under the following conditions [18]:

- $\lim_{\|\mathbf{x}\| \to \infty} f(\mathbf{x}) = +\infty$

- $\cap_{i=1}^m \text{ri dom} f_i \neq \emptyset$ (the intersection of the relative interiors of the domains of f_i is nonempty)

- $\lim_{n_p \to \infty} \sum_{j=0}^{n_p} \xi_j(2 - \xi_j) = +\infty$

- $\forall i \in \{1, \ldots, m\} \lim_{n_p \to \infty} \sum_{j=0}^{n_p} \xi_j \|\varepsilon_{i,j}\| < +\infty$ (the possible error $\varepsilon_{i,j}$ in the computation of the ith proximal operator decreases to zero)

For the data-driven fault diagnosis problem (4.18) the first two conditions are naturally satisfied and the third condition by the straightforward choice $\xi_j = 1 \, \forall j$. Assuming the ability for precise evaluation of the proximal operators (for instance by closed-form computation) and by assigning trivial values to the weights $\omega_i = 1/m$, the only remaining tuning parameter γ affects the speed of convergence. A small step size γ will lead to slow initial convergence, whereas a large step size decelerates convergence close to the optimum.

With the soft-thresholding operator defined entrywise as

$$[\mathscr{S}_\gamma(\mathbf{v})]_n = \text{sign}(\mathbf{v}_n)[|\mathbf{v}_n| - \gamma]_+ \tag{4.20}$$

closed-form expressions for the proximal operators of the objective terms in optimization problem (4.18) are presented in Table 4.1. The evaluation of $\text{prox}_{\gamma f_1}$ is relatively computationally expensive due to the inverse $(\gamma H^\top H + I)^{-1}$, which would require $O(n_\mathbf{x}^3)$ flops for each iteration of the proximal algorithm. However, given that PPXA allows some small errors $\varepsilon_{i,j}$ in the calculation of the proximal operators, there are several possibilities to ease the evaluation of $\text{prox}_{\gamma f_1}(\mathbf{v})$. Some of these possibilities are specified in the next section.

4.4.1. OPPORTUNITIES FOR ACCELERATED IMPLEMENTATION

Since the inverse $(\gamma H^\top H + I)^{-1}$ and $\gamma H^\top \mathbf{y}$ remain invariable over the iterations of the proximal algorithm for the batch problem (4.18), a first option is to cache and reuse it in subsequent iterations of the proximal algorithm. This would require $O(n_\mathbf{x}^3)$ flops for the first iteration, however only $O(n_\mathbf{x}^2)$ flops for subsequent iterations, without introducing approximation errors.

A second option is to replace the proximal operator with a step in the direction of the negative gradient, as elaborated in the following lemma.

Lemma 4.2. *If γ is small enough such that*

$$\lim_{n \to \infty} (-\gamma H^\top H)^n = 0, \tag{4.21}$$

the proximal operator for γf_1 can be approximated by a step in the direction of its negative gradient:

$$\text{prox}_{\gamma f_1}(\mathbf{v}) \approx \mathbf{v} - \gamma H^\top H \mathbf{v} + \gamma H^\top \mathbf{y} = \mathbf{v} - \gamma \nabla f_1(\mathbf{v}). \tag{4.22}$$

Proof. Under condition (4.21), by the Neumann series:

$$(\gamma H^\top H + I)^{-1} = \sum_{n=0}^{\infty} (-\gamma H^\top H)^n$$
$$= I - \gamma H^\top H + \sum_{n=2}^{\infty} (-\gamma H^\top H)^n$$
$$= I - \gamma H^\top H + e(\gamma, H)$$

Table 4.1: Proximal operators for objective terms in (4.18) with step size γ.

Function $g(\mathbf{x})$	Proximal operator $\text{prox}_{\gamma g}(\mathbf{v})$
$f_1(\mathbf{x}) = \frac{1}{2}\|\mathbf{y} - H\mathbf{x}\|_2^2$	$(\gamma H^\top H + I)^{-1}(\mathbf{v} + \gamma H^\top \mathbf{y})$
$f_2(\mathbf{x}) = \tau\|\mathbf{x}_L\|_*$ [38]	$U\mathscr{S}_{\gamma\tau}(\Sigma)V^\top$
	with SVD $\mathbf{v}_L = U\Sigma V^\top$
$f_3(\mathbf{x}) = \lambda\|\mathbf{x}_S\|_1$	$\mathscr{S}_{\gamma\lambda}(\mathbf{v}_S)$

This approximation is substituted in the proximal operator for f_1 in Table 4.1:

$$\text{prox}_{\gamma f_1}(\mathbf{v}) = \big(I - \gamma H^\top H + e(\gamma, H)\big)(\mathbf{v} + \gamma H^\top \mathbf{y})$$

$$= \mathbf{v} - \gamma(H^\top H\mathbf{v} - H^\top \mathbf{y}) - \gamma^2 H^\top H H^\top \mathbf{y}$$
$$+ e(\gamma, H)(\mathbf{v} + \gamma H^\top \mathbf{y})$$

$$= \mathbf{v} - \gamma\nabla f_1(\mathbf{v}) - \gamma^2 H^\top H H^\top \mathbf{y}$$
$$+ e(\gamma, H)(\mathbf{v} + \gamma H^\top \mathbf{y}),$$

which concludes the proof. □

The gradient step in (4.22) reduces the computational complexity to $O(n_{\mathbf{x}}^2)$ flops for each iteration. This goes at the expense of trading off γ for small approximation errors and fast convergence while guaranteeing (4.21).

A third possibility is to approximate it with an iterative method such as conjugate gradient, provided with a warm start from a previous solution [17]. The conjugate gradient method requires multiple iterations of $O(n_{\mathbf{x}}^2)$ flops in order to solve $\text{prox}_{\gamma f_1}(\mathbf{v})$. However, in contrast to approximation (4.22), the conjugate gradient method allows the tolerance (and thus the magnitude of the approximation error $\varepsilon_{i,j}$) to be predefined, providing more control on the convergence properties of Algorithm 1.

4.5. Proximal-based recursive implementation

Multiple variants are possible to solve (4.18) online in which each time step a new set of inputs and outputs become available. Let us consider (4.18) over an Infinite Window (IW), Finite moving Window (FW) or Exponentially Weighted (EW) window. These are all addressed by the following adapted cost function:

$$\hat{\mathbf{x}}_k = \arg\min_{\mathbf{x}} \frac{1}{2}\sum_{j=\ell}^{k} \beta_{k-j}\|y_j - H_j\mathbf{x}\|_2^2 + \tau\|\mathbf{x}_L\|_* + \lambda\|\mathbf{x}_S\|_1 \tag{4.23}$$

where $0 \le \beta_{k-j} \le 1$ is a forgetting factor and H_j is the regressor matrix corresponding to time instance j. The formulation (4.23) allows to make three different choices by the parameters ℓ and β_{k-j} as highlighted in Table 4.2. With the corresponding

Table 4.2: Basic instances of (4.23) by choices of ℓ and β_{k-j}, where $\mathscr{L}$ is a fixed window length and $0 \le \beta < 1$.

Window type	ℓ	β_{k-j}	$\mathbf{R}_k$	$\mathbf{r}_k$
Infinite Window (IW)	1	1	$\mathbf{R}_{k-1} + H_k^\top H_k$	$\mathbf{r}_{k-1} + H_k^\top y_k$
Finite Window (FW)	$k - \mathscr{L}$	1	$\mathbf{R}_{k-1} + H_k^\top H_k - H_\ell^\top H_\ell$	$\mathbf{r}_{k-1} + H_k^\top y_k - H_\ell^\top y_\ell$
Expon. Weighted (EW)	1	β^{k-j}	$\beta \mathbf{R}_{k-1} + H_k^\top H_k$	$\beta \mathbf{r}_{k-1} + H_k^\top y_k$

recursive definitions $\mathbf{R}_k$ and $\mathbf{r}_k$ in Table 4.2, the argument of optimization problem (4.23) can be found by

$$\begin{aligned}\hat{\mathbf{x}}_k &= \arg\min_{\mathbf{x}} \frac{1}{2}\mathbf{x}^\top \mathbf{R}_k \mathbf{x} - \mathbf{x}^\top \mathbf{r}_k + \tau \|\mathbf{x}_L\|_* + \lambda \|\mathbf{x}_S\|_1 \\ &= \arg\min_{\mathbf{x}} f_{r,k}(\mathbf{x}) + f_2(\mathbf{x}) + f_3(\mathbf{x}). \end{aligned} \tag{4.24}$$

Accordingly, the proximal operator for the least-squares term $f_{r,k}$ is

$$\text{prox}_{\gamma f_{r,k}}(\mathbf{v}) = (\gamma \mathbf{R}_k + I)^{-1}(\mathbf{v} + \gamma \mathbf{r}_k). \tag{4.25}$$

Together with the proximal operators for f_2 and f_3 in Table 4.1, PPXA in Algorithm 1 can be performed each time instance k with warm start $\mathbf{x}_0 = \hat{\mathbf{x}}_{k-1}$ in order to solve (4.24).

Section 4.4.1 provides three opportunities to accelerate the evaluation of the proximal operator for the least-squares term in the batch problem (4.18). These opportunities can be extended to the case when the cost function is recursive as in (4.24). The first opportunity of caching and reusing the inverse enables exact evaluation, however in the recursive problem the inverse $(\gamma \mathbf{R}_k + I)^{-1}$ should be updated each time step. This exact evaluation is handled in Section 4.5.1, whereas two approximations analogous to those in Section 4.4.1 are elaborated in Section 4.5.2.

4.5.1. EXACT RECURSIVE EVALUATION OF (4.25)

Depending on the window type, the evaluation of $\text{prox}_{\gamma f_{r,k}}$ can be accelerated using the matrix inversion lemma (for Infinite Window (IW) and Finite Window (FW)) or CG (for Exponentially Weighted (EW) window). First, we study the case of IW after which FW is studied in the following two lemmas, which are general results from recursive least-squares literature [39].

Lemma 4.3. *In the case of IW, $\mathbf{P}_k = (\gamma \mathbf{R}_k + I)^{-1}$ can be updated recursively by*

$$\mathbf{P}_k = \mathbf{P}_{k-1} - \gamma \mathbf{P}_{k-1} H_k^\top (I + \gamma H_k \mathbf{P}_{k-1} H_k^\top)^{-1} H_k \mathbf{P}_{k-1}. \tag{4.26}$$

Proof. The matrix inversion lemma is given by [23]:

$$(A + BCD)^{-1} = A^{-1} - A^{-1}B(C^{-1} + DA^{-1}B)^{-1}DA^{-1}. \tag{4.27}$$

In the case of IW (see Table 4.2),

$$(\gamma \mathbf{R}_k + I)^{-1} = \left((\gamma \mathbf{R}_{k-1} + I) + \gamma H_k^\top H_k \right)^{-1}.$$

By substituting the matrices in (4.27) with

$$A \leftarrow \mathbf{P}_{k-1}^{-1} = (\gamma \mathbf{R}_{k-1} + I), \qquad\qquad B \leftarrow \gamma H_k^\top,$$
$$C \leftarrow I, \qquad\qquad D \leftarrow H_k$$

one arrives at (4.26).   □

Lemma 4.4. *In the case of FW, $\mathbf{P}_k = (\gamma \mathbf{R}_k + I)^{-1}$ can be updated recursively by*

$$\mathbf{P}_k' = \mathbf{P}_{k-1} - \gamma \mathbf{P}_{k-1} H_k^\top (I + \gamma H_k \mathbf{P}_{k-1} H_k^\top)^{-1} H_k \mathbf{P}_{k-1}$$
$$\mathbf{P}_k = \mathbf{P}_k' - \gamma \mathbf{P}_k' H_\ell^\top (-I + \gamma H_\ell \mathbf{P}_k' H_\ell^\top)^{-1} H_\ell \mathbf{P}_k' \tag{4.28}$$

Proof. By defining

$$\mathbf{P}_k' = (\gamma \mathbf{R}_k' + I)^{-1} = \left((\gamma \mathbf{R}_{k-1} + I) + \gamma H_k^\top H_k \right)^{-1},$$

the first line in (4.28) is obtained using Lemma 4.3.

In the case of FW (see Table 4.2),

$$(\gamma \mathbf{R}_k + I)^{-1} = \left((\gamma \mathbf{R}_{k-1} + I + \gamma H_k^\top H_k) - \gamma H_\ell^\top H_\ell \right)^{-1}$$
$$= \left((\gamma \mathbf{R}_k' + I) - \gamma H_\ell^\top H_\ell \right)^{-1}.$$

By substituting the matrices in (4.27) with

$$A \leftarrow (\mathbf{P}_k')^{-1} = (\gamma \mathbf{R}_k' + I), \qquad\qquad B \leftarrow \gamma H_\ell^\top,$$
$$C \leftarrow -I, \qquad\qquad D \leftarrow H_\ell$$

one arrives at the second line in (4.28).   □

The computational complexity for evaluating the proximal operator (4.25) using (4.26) or (4.28) is $O(n_{\mathbf{x}}^2)$ flops for each iteration of the proximal algorithm.

4.5.2. APPROXIMATE EVALUATION OF (4.25)

An exact recursive update of $(\gamma \mathbf{R}_k + I)^{-1}$ is not for each window type available. For EW some possibilities for approximating this covariance matrix based on $(\gamma \mathbf{R}_{k-1} + I)^{-1}$ and $\gamma H_k^\top H_k$ are summarized in [40], in general at the cost of $O(n_{\mathbf{x}}^2)$ flops each time step k. However, such approximation induces the corresponding errors to propagate over time.

Following Lemma 4.2, the proximal operator in (4.25) can be approximated by a step in the direction of the negative gradient, for which evaluation of the matrix inversion is not required. Such gradient step involves a computational complexity of $O(n_{\mathbf{x}}^2)$ flops per iteration of the proximal algorithm. This is however at the expense

of inducing an upper bound on γ, which in the recursive variant cannot be verified prior to the experiment.

An alternative to the gradient step as introduced in Section 4.4.1, is to approximate the proximal operator in (4.25) using the conjugate gradient method provided with a warm start. This requires multiple evaluations of $O(n_{\mathbf{x}}^2)$ flops each iteration of the proximal algorithm and allows the approximation tolerance to be predefined. The warm start could for instance be provided from a previous solution of the proximal algorithm at no computational cost.

4.5.3. ALGORITHM OVERVIEW

The overview of the proximal-based implementation for model-free data driven fault diagnosis is presented in Algorithm 2. It should be noted that this scheme is applied straightforwardly to optimization problems in the form of (4.24), as well as recursive least-squares problems with convex regularization terms different from the nuclear norm and 1-norm, especially when closed-form expressions of their corresponding proximal operators are available. A list of functions with closed-form expressions for the proximal operators is for instance given in [16].

Algorithm 2 Proximal-based implementation for solving (4.24) recursively

---

Initialization

    $0 < \rho < \infty$ ▷ Scalar step size

    $0 < \omega = [\omega_1, \omega_2, \omega_3] \le 1$ satisfying $\sum_{i=1}^{3} \omega_i = 1$

    $\Gamma = [\gamma_1, \gamma_2, \gamma_3] = \rho \omega$

    $\hat{\mathbf{x}}_{s-1}$ ▷ Initial condition

for $k = s, \dots, N$ **do**

    Obtain measurement y_k with regressor H_k

    Update $\mathbf{R}_k$ and $\mathbf{r}_k$ in (4.25) using Table 4.2

    If applicable update $\mathbf{P}_k = (\gamma_1 \mathbf{R}_k + I)^{-1}$ using (4.26) or (4.28)

    $\hat{\mathbf{x}}_k = \text{PPXA}(\Gamma, \omega, \hat{\mathbf{x}}_{k-1})$ (Algorithm 1) using the updated $\text{prox}_{\gamma_1 f_{r,k}}$ in (4.25), and from Table 4.1 $\text{prox}_{\gamma_2 f_2}$ and $\text{prox}_{\gamma_3 f_3}$

end for

In order to solve (4.24), Algorithm 2 preserves the convergence properties of PPXA [18] summarized in Algorithm 1. The warm start from $\hat{\mathbf{x}}_{k-1}$ allows to perform only a small number of iterations n_p in PPXA, suppressing the computational effort per time instance k. The experimental demonstration of Algorithm 2 is presented in Sect. 4.6.3.

4.6. NUMERICAL RESULTS

Consider the buck converter in Fig. 4.2 as example for a DC-DC switch mode power supply. In [41] the issue is raised that contemporary system identification procedures for DC-DC switch mode power supplies cannot handle unknown rapidly

varying load resistances. However, when a set of possible load profiles is available
– for instance when multiple loads are connected but not necessarily activated –
the proposed data-driven fault diagnosis procedure can be implemented in order to
identify the system characteristics simultaneously to diagnosing the activated loads.
The assumptions are as follows:

- The voltage difference over the load resistance $V_R(k)$ is measured as output
  variable, corrupted with noise $y(k) = V_R(k) + v(k)$.

- The duty ratio of the switch is regarded as the known input variable
  $u(k) = S_B(k)$. These are typical input/output variables [41].

- The load resistance $R_B(k) = R_B + \Delta R_B(k)$ consists of a static part R_B and a
  time-varying part $\Delta R_B(k)$.

- For the time-varying load resistance $d(k) = \Delta R_B(k) = \theta(k)z$, a dictionary $\theta(k)$ of
  possible profiles (or: faults) is known, but not necessarily their magnitudes z.
  Only a small number of possible load resistance profiles from the dictionary is
  active.

- The variables L_B, C_B, V_B and R_B are unknown.

The simultaneous goals are:

- Identify the system (obtain an equivalent for the knowledge of L_B, C_B, V_B and
  R_B).

- Diagnose the time-varying load resistance $\Delta R_B(k)$.

In order to show that the dynamics of the buck converter can be captured in
(4.5), an averaged and linearized model of the buck converter is presented in
Appendix 4.A. The nominal numerical values are taken similar to those in [42],
namely $V_B = 10$ V, $L_B = 220$ μH, $C_B = 330$ μF and $R_B = 5$ Ω. The switching frequency
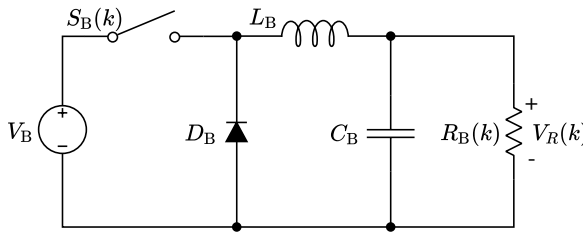

Figure 4.2: Buck converter circuit with inductance L_B, diode D_B, capacitance C_B,
switch with duty ratio $S_B(k)$, source voltage V_B and time-varying load
resistance $R_B(k)$. The voltage difference over the load resistance $V_R(k)$ is
measurable.

is 200 kHz and the sampling rate 20 kHz. The initial voltage $V_R(0) = 4.5$ V and initial inductor current $i_L(0) = 0.9$ A. The measurement noise is distributed as $v(k) \sim \mathcal{N}(0, 10^{-3})$. The duty ratio of the switch $S_B(k)$ takes the values 0.4 and 0.5 following a pseudo-random binary signal. The time-varying load resistance $\Delta R_B(k)$ is built up from the dictionary $\theta(k) \in \mathbb{R}^{1 \times 50}$ consisting of 50 square waves with linearly increasing frequencies between 1000 and 1900 Hz and amplitude 1 Ω. The fault parameter vector $z \in \mathbb{R}^{50}$ consists of zeros with randomly drawn entries set to one.

4.6.1. DATA-DRIVEN FAULT DIAGNOSIS

The simulation experiment tests the proposed approach to model-free data-driven fault diagnosis in (4.14) with number of data points $N = 1200$, VARX order $s = 3$ and $\tau = \lambda = 10$. It is solved using PPXA in Algorithm 1 with $\gamma = 10^{-3}$ and $n_p = 10^4$.

Fig. 4.3 shows a typical realization of the simulated buck converter in the case of three active faults. In the bottom figure it can be seen that the entries of z corresponding to the activated square waves are diagnosed correctly up to a multiplicative scalar. After applying the refinement step as elaborated in Section 4.3.3, the estimates of **B**, **K**, **F** and z are verified with a Variance Accounted For (VAF) [23] of 98.8%.

4.6.2. COMPARISON TO MODEL-BASED FAULT DIAGNOSIS

The proposed model-free approach with parameters as in Sect. 4.6.1 is compared to model-based fault diagnosis using an error-free and erroneous linearized model. The corresponding linear VARX-models required for the model-based approach are constructed as described in Appendix 4.A, after which an error of 0.4 is introduced in the $(2,1)$th element of the discretized A-matrix. Then, the observer poles for the discretized linear models are placed on 0.2 and 0.21 and a VARX model order of s=8 is chosen. These models are then used in the model-based approach (4.11) with $\lambda = 0.3$ and solved using CVX [43].

Based on 100 realizations, the rates of successful fault isolation against the number of data points are presented in Figs. 4.4 and 4.5 for three and four active faults, respectively. The isolation is regarded successful if each nonzero component of $\hat{z}$ satisfying $|\hat{z}| > \epsilon \|\hat{z}\|_\infty$ with $\epsilon = 0.1$ is diagnosed while the other components are not, i.e. no misdetection nor overdetection.

For three active faults, Fig. 4.4 shows that the model-free approach requires more data than the model-based approach in order to reach a high isolation rate. However, if the employed model is erroneous, the isolation rate of the model-based approach remains at a value around 80%, regardless of the increasing data size. For four active faults, Fig. 4.5 presents a different phenomenon, namely a decreasing isolation rate from a certain data size. Since the net load resistance $R_B(k)$ approaches zero at certain time instances, the buck converter starts showing non-negligible nonlinear behavior. Since the performance of the model-free approach decreases slower than the model-based approach, it appears that the model-free approach can better accommodate this nonlinearity.
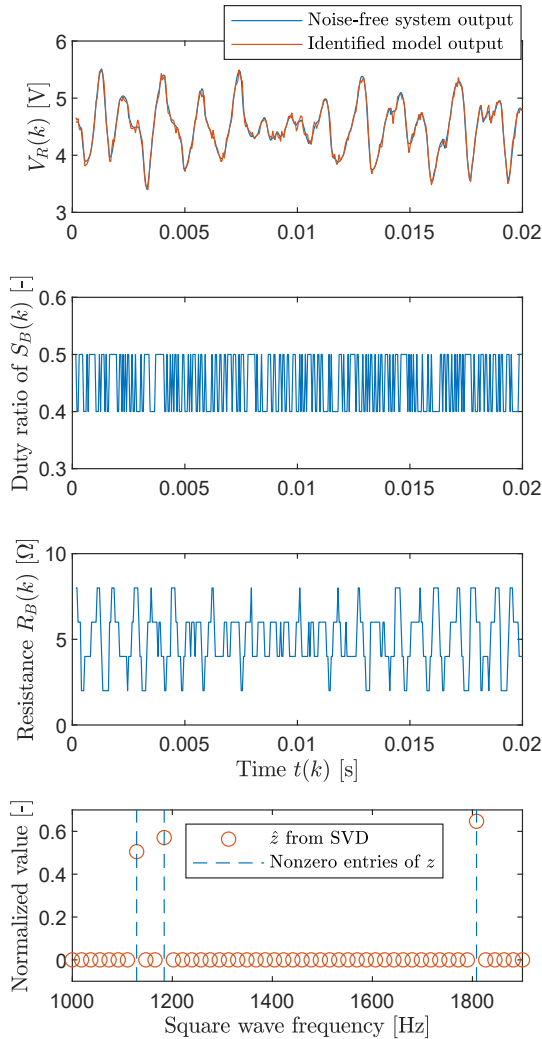
Figure 4.3: Part of a realization of the noise-free system output of the buck-converter with corresponding duty ratio as input and load resistance $R_B(k)$. A solution of the optimization problem (4.14) provides diagnosis of z (bottom, red circles) and a refinement step using (4.14) with $\lambda = 0$ provides system identification with VAF 98.8% (top, red) with respect to the noise-free system output.
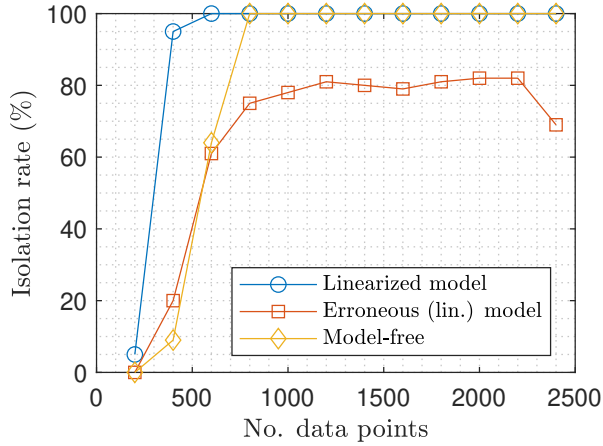
Figure 4.4: Successful isolation rate in case of three active faults using a linearized model (blue, ∘), an erroneous linearized model (red, □) and the proposed model-free approach (yellow, ◇).   More data leads to an increased isolation rate and the model-free approach outperforming the model-based approach with an erroneous model.
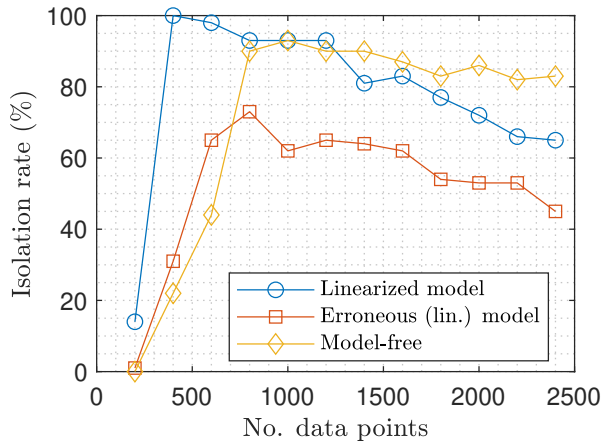

Figure 4.5: Successful isolation rate in case of four active faults using a linearized model (blue, ∘), an erroneous linearized model (red, □) and the proposed model-free approach (yellow, ◇). More data reveals the nonlinear nature of the buck converter in the condition of four active faults. The model-based approach decreases in performance more than the model-free approach.
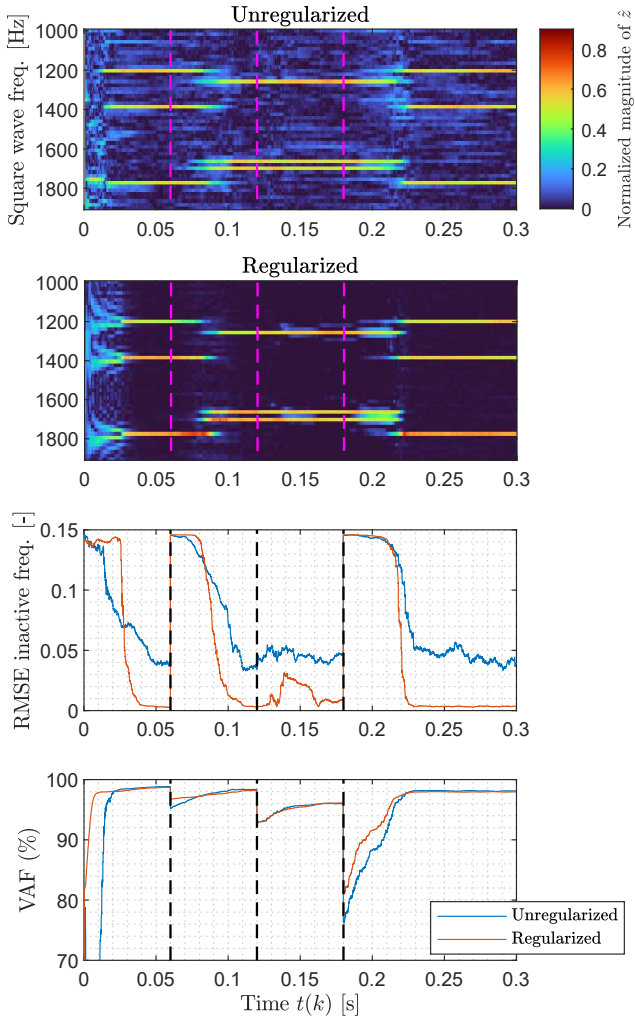
Figure 4.6: The diagnosed faults over time without regularization using recursive least squares ([39], FW with $\mathbf{R}_0 = I$, top) and with regularization using the recursive proximal algorithm ((4.23), FW with $\mathbf{R}_0 = 0$ solved using Algorithm 2, second), together with their corresponding Root Mean Square Error (RMSE) with respect to the inactive faults (third) and the VAF of the simultaneously identified model (bottom). The vertical dashed lines at $t = 0.06$, $t = 0.12$ and $t = 0.18$ s indicate a change in active faults, system characteristics and both, respectively. The average computational time per time instance k on an Intel i7-9750H CPU was 929 μs for Algorithm 2 versus 148 μs for unregularized recursive least squares.

4.6.3. PROXIMAL-BASED RECURSIVE IMPLEMENTATION

The second simulation experiment demonstrates the recursive implementation of the proximal algorithm as described in Algorithm 2. Here we consider optimization problem (4.23) with a finite window using $\mathcal{L} = 1000$ samples. Equivalently to Section 4.6.1, $s = 3$, $\tau = \lambda = 10$ and $\gamma = 10^{-3}$. Each time step, the PPXA algorithm performs $n_p = 10$ iterations initialized with a warm start from previous time step. The results are compared to those without regularization using recursive least squares [39].

The results are shown in Fig. 4.6. In the initial configuration ($0 \leq t < 0.06$ s) the VAF for system identification converges around $t = 0.01$ s and the faults can be diagnosed correctly from circa $t = 0.04$ s. In the second phase ($0.06 \leq t < 0.12$ s) the active faults have changed to different square wave frequencies. The VAF decreases slightly after which it slowly increases again. Simultaneously, the new faults can be diagnosed from circa $t = 0.11$ s. In the third phase ($0.12 \leq t < 0.18$ s) the system characteristics have changed by adjusting the nominal load resistance R_B from 5 Ω to 3.5 Ω. This results in a reduction in the VAF, after which it increases again. The diagnosed faults remain roughly constant. In the fourth phase ($0.18 \leq t < 0.3$ s) both the active faults and model change to their original configuration. Now the VAF shows a sharp drop, but again it recovers after some time and also the original faults are diagnosed again around $t = 0.23$ s. By the regularization on the nuclear norm and the 1-norm, the recursive proximal algorithm outperforms unregularized recursive least squares in identifying the system in a small number of measurements, and in highlighting the active faults while suppressing the entries of the non-active faults.

4.7. CONCLUSION

Model-free data-driven fault diagnosis aims at identifying the system and diagnosing the faults *simultaneously*, eliminating the necessity of an extensive identification phase prior to diagnosing faults. A proposed approach reformulates it as a convex optimization problem in order to make it computationally attractive. This approach is implemented online using a recursive implementation of a proximal algorithm.

The numerical results on a buck converter show how the faults are diagnosed simultaneous to system identification. A second simulation shows how the recursive implementation handles varying system parameters and (dis-)appearance of faults during operation.

The newly introduced methodology provides ample room for future research. A few examples are outlined as follows. First, the diagnosis performance trade-off with respect to the data size could be analyzed theoretically, including a comparison with model-based and state-of-the-art data-driven techniques. This is presumably dependent on the chosen input signal and the fault dictionary. The second is the evaluation of the uncertainty of the estimated quantities with respect to the number of active faults, the properties of the I/O-data and those of the dictionary. On the algorithmic side we mention a third area of future research related to competitive optimization algorithms able to handle more than two possibly non-smooth objective term. In line of that research objective the computational efficiency of the recursive implementation could be further improved exploiting possible structure in the

problem.

4.A. BUCK CONVERTER SYSTEM EQUATIONS

Regarding the continuous-time variables

$$x(t) = \begin{bmatrix} x_1(t) \\ x_2(t) \end{bmatrix} = \begin{bmatrix} i_L(t) \\ V_R(t) \end{bmatrix}$$

$$u(t) = S_{\mathrm{B}}(t)$$

(4.29)

where $i_L(t)$ is the current through the inductor, the averaged [44] continuous-time model for the buck converter is

$$\dot{x}(t) = \begin{bmatrix} 0 & \frac{-1}{L_{\mathrm{B}}} \\ \frac{1}{C_{\mathrm{B}}} & \frac{-1}{R_{\mathrm{B}}C_{\mathrm{B}}} \end{bmatrix} x(t) + \begin{bmatrix} \frac{V_{\mathrm{B}}}{L_{\mathrm{B}}} \\ 0 \end{bmatrix} u(t)$$

$$+ \begin{bmatrix} 0 \\ \frac{\Delta R_{\mathrm{B}}(t) V_R(t)}{(R_{\mathrm{B}} + \Delta R_{\mathrm{B}}(t)) R_{\mathrm{B}} C_{\mathrm{B}}} \end{bmatrix}$$

$$y(t) = \begin{bmatrix} 0 & 1 \end{bmatrix} x(t) + v(t)$$

(4.30)

Linearization around $\overline{\Delta R}_{\mathrm{B}} = 0$ and $\overline{V}_R$ yields

$$\dot{x}(t) = \begin{bmatrix} 0 & \frac{-1}{L_{\mathrm{B}}} \\ \frac{1}{C_{\mathrm{B}}} & \frac{-1}{R_{\mathrm{B}}C_{\mathrm{B}}} \end{bmatrix} x(t) + \begin{bmatrix} \frac{V_{\mathrm{B}}}{L_{\mathrm{B}}} \\ 0 \end{bmatrix} u(t) + \begin{bmatrix} 0 \\ \frac{\overline{V}_R}{R_{\mathrm{B}}^2 C_{\mathrm{B}}} \end{bmatrix} d(t)$$

$$y(t) = \begin{bmatrix} 0 & 1 \end{bmatrix} x(t) + v(t)$$

(4.31)

where $d(t) = \Delta R_{\mathrm{B}}(t)$. Assuming zero-order hold for $u(t)$ and $d(t)$, the discretized state-space representation is

$$x(k+1) = Ax(k) + Bu(k) + Fd(k)$$

$$y(k) = x(k) + v(k),$$

(4.32)

which can be approximated by the VARX model (4.5).

REFERENCES

[1] J. Noom, O. Soloviev, and M. Verhaegen. "Proximal-based recursive implementation for model-free data-driven fault diagnosis". Accepted for publication in Automatica.

[2] J. Noom, O. Soloviev, and M. Verhaegen. "Data-driven fault diagnosis under sparseness assumption for LTI systems". In: *IFAC-PapersOnLine* 56.2 (2023), pp. 7722–7727. DOI: 10.1016/j.ifacol.2023.10.1176.

[3] J. Noom. *Matlab code for model-free data-driven fault diagnosis*. 2024. DOI: 10.5281/zenodo.10454000.

[4] T. Samad, M. Bauer, S. Bortoff, S. Di Cairano, L. Fagiano, P. F. Odgaard, R. R. Rhinehart, R. Sánchez-Peña, A. Serbezov, F. Ankersen, P. Goupil, B. Grosman, M. Heertjes, I. Mareels, and R. Sosseh. "Industry engagement with control research: Perspective and messages". In: *Annual Reviews in Control* 49 (2020), pp. 1–14. ISSN: 1367-5788. DOI: 10.1016/j.arcontrol.2020.03.002.

[5] Z. Gao, C. Cecati, and S. X. Ding. "A survey of fault diagnosis and fault-tolerant techniques – Part I: Fault diagnosis with model-based and signal-based approaches". In: *IEEE Transactions on Industrial Electronics* 62.6 (2015), pp. 3757–3767. DOI: 10.1109/TIE.2015.2417501.

[6] Z. Gao, C. Cecati, and S. X. Ding. "A survey of fault diagnosis and fault-tolerant techniques – Part II: Fault diagnosis with knowledge-based and hybrid/active approaches". In: *IEEE Transactions on Industrial Electronics* 62.6 (2015), pp. 3768–3774. DOI: 10.1109/TIE.2015.2419013.

[7] V. Venkatasubramanian, R. Rengaswamy, S. N. Kavuri, and K. Yin. "A review of process fault detection and diagnosis – Part III: Process history based methods". In: *Computers & Chemical Engineering* 27.3 (2003), pp. 327–346. DOI: 10.1016/S0098-1354(02)00162-x.

[8] X. Dai and Z. Gao. "From Model, Signal to Knowledge: A Data-Driven Perspective of Fault Detection and Diagnosis". In: *IEEE Transactions on Industrial Informatics* 9.4 (2013), pp. 2226–2238. DOI: 10.1109/TII.2013.2243743.

[9] S. Yin, S. X. Ding, X. Xie, and H. Luo. "A Review on Basic Data-Driven Approaches for Industrial Process Monitoring". In: *IEEE Transactions on Industrial Electronics* 61.11 (2014), pp. 6418–6428. DOI: 10.1109/TIE.2014.2301773.

[10] S. X. Ding. *Data-driven design of fault diagnosis and fault-tolerant control systems*. Springer-Verlag London, 2014. DOI: 10.1007/978-1-4471-6410-4.

[11]   S. Simani. "Data-Driven Methods for Fault Diagnosis". In: *Diagnosis and Fault-tolerant Control 1: Data-driven and Model-based Fault Diagnosis Techniques.* Ed. by V. Puig and S. Simani. ISTE Ltd and John Wiley & Sons, Inc., 2021. Chap. 5, pp. 131–195. DOI: 10.1002/9781119882329.ch5.

[12]   Z. Chen. *Data-Driven Fault Detection for Industrial Processes.* Springer Fachmedien Wiesbaden, 2017. DOI: 10.1007/978-3-658-16756-1.

[13]   J. Noom, O. Soloviev, C. Smith, and M. Verhaegen. "Closed-loop active object recognition with constrained illumination power". In: *Real-Time Image Processing and Deep Learning 2022.* Ed. by N. Kehtarnavaz and M. F. Carlsohn. Vol. 12102. International Society for Optics and Photonics. SPIE, 2022, pp. 9–14. DOI: 10.1117/12.2618750.

[14]   Q. Zhang. "Dynamic System Fault Diagnosis Under Sparseness Assumption". In: *IEEE Transactions on Signal Processing* 69 (2021), pp. 2499–2508. DOI: 10.1109/TSP.2021.3072004.

[15]   D. Scobee, L. Ratliff, R. Dong, H. Ohlsson, M. Verhaegen, and S. S. Sastry. "Nuclear norm minimization for blind subspace identification (N2BSID)". In: *54th IEEE Conference on Decision and Control.* 2015, pp. 2127–2132. DOI: 10.1109/CDC.2015.7402521.

[16]   P. L. Combettes and J.-C. Pesquet. "Proximal Splitting Methods in Signal Processing". In: *Fixed-Point Algorithms for Inverse Problems in Science and Engineering.* Ed. by H. H. Bauschke, R. S. Burachik, P. L. Combettes, V. Elser, D. R. Luke, and H. Wolkowicz. Springer New York, 2011, pp. 185–212. DOI: 10.1007/978-1-4419-9569-8_10.

[17]   N. Parikh and S. Boyd. "Proximal Algorithms". In: *Foundations and Trends® in Optimization* 1.3 (2014), pp. 127–239. DOI: 10.1561/2400000003.

[18]   P. L. Combettes and J.-C. Pesquet. "A proximal decomposition method for solving convex variational inverse problems*". In: *Inverse Problems* 24.6 (2008), p. 065014. DOI: 10.1088/0266-5611/24/6/065014.

[19]   D. Angelosante and G. B. Giannakis. "RLS-weighted lasso for adaptive estimation of sparse signals". In: *2009 IEEE International Conference on Acoustics, Speech and Signal Processing.* 2009, pp. 3245–3248. DOI: 10.1109/ICASSP.2009.4960316.

[20]   R. Dixit, A. S. Bedi, R. Tripathi, and K. Rajawat. "Online Learning With Inexact Proximal Online Gradient Descent Algorithms". In: *IEEE Transactions on Signal Processing* 67.5 (2019), pp. 1338–1352. DOI: 10.1109/TSP.2018.2890368.

[21]   A. Ajalloeian, A. Simonetto, and E. Dall'Anese. "Inexact Online Proximal-gradient Method for Time-varying Convex Optimization". In: *2020 American Control Conference (ACC).* 2020, pp. 2850–2857. DOI: 10.23919/ACC45564.2020.9147467.

[22]   A. Chiuso. "The role of vector autoregressive modeling in predictor-based subspace identification". In: *Automatica* 43.6 (2007), pp. 1034–1048. DOI: 10.1016/j.automatica.2006.12.009.

[23] M. Verhaegen and V. Verdult. *Filtering and System Identification: A Least Squares Approach*. Cambridge: Cambridge University Press, 2007. ISBN: 978-1107405028.

[24] M. Q. Phan and R. W. Longman. "Relationship Between State-space And Input-output Models Via Observer Markov Parameters". In: *WIT Transactions on The Built Environment* 22 (1996), pp. 185–200.

[25] H. Lütkepohl. *New Introduction to Multiple Time Series Analysis*. Springer-Verlag Berlin Heidelberg, 2005. ISBN: 9783540277521.

[26] L. Ljung. *System Identification: Theory for the User*. Prentice Hall information and system sciences series. Prentice Hall PTR, 1999. ISBN: 9780136566953.

[27] M. Basseville and I. V. Nikiforov. *Detection of abrupt changes: theory and application*. Englewood Cliffs, New Jersey: Prentice-Hall, Inc., 1993. ISBN: 978-0131267800.

[28] M. Blanke, M. Kinnaert, J. Lunze, and M. Staroswieck. *Diagnosis and Fault-Tolerant Control*. 2nd. Springer-Verlag Berlin Heidelberg, 2006. DOI: 10.1007/978-3-540-35653-0.

[29] S. X. Ding. *Model-Based Fault Diagnosis Techniques*. 2nd. Springer-Verlag London, 2013. DOI: 10.1007/978-1-4471-4799-2.

[30] A. Ali and R. J. Tibshirani. "The Generalized Lasso Problem and Uniqueness". In: *Electronic Journal of Statistics* 13.2 (2019), pp. 2307–2347. DOI: 10.1214/19-EJS1569.

[31] L. Bliek, H. R. G. W. Verstraete, M. Verhaegen, and S. Wahls. "Online Optimization With Costly and Noisy Measurements Using Random Fourier Expansions". In: *IEEE Transactions on Neural Networks and Learning Systems* 29.1 (2018), pp. 167–182. DOI: 10.1109/TNNLS.2016.2615134.

[32] P. Freeman, P. Seiler, and G. J. Balas. "Air data system fault modeling and detection". In: *Control Engineering Practice* 21.10 (2013), pp. 1290–1301. DOI: 10.1016/j.conengprac.2013.05.007.

[33] P. L. Combettes and V. R. Wajs. "Signal Recovery by Proximal Forward-Backward Splitting". In: *Multiscale Modeling & Simulation* 4.4 (2005), pp. 1168–1200. DOI: 10.1137/050626090.

[34] P. L. Combettes and J.-C. Pesquet. "A Douglas–Rachford Splitting Approach to Nonsmooth Convex Variational Signal Recovery". In: *IEEE Journal of Selected Topics in Signal Processing* 1.4 (2007), pp. 564–574. DOI: 10.1109/JSTSP.2007.910264.

[35] A. Beck and M. Teboulle. "A Fast Iterative Shrinkage-Thresholding Algorithm for Linear Inverse Problems". In: *SIAM Journal on Imaging Sciences* 2.1 (2009), pp. 183–202. DOI: 10.1137/080716542.

[36] H. Raguet, J. Fadili, and G. Peyré. "A Generalized Forward-Backward Splitting". In: *SIAM Journal on Imaging Sciences* 6.3 (2013), pp. 1199–1226. DOI: 10.1137/120872802.

[37] D. Davis and W. Yin. "A Three-Operator Splitting Scheme and its Optimization Applications". In: *Set-Valued and Variational Analysis* 25.4 (2017), pp. 829–858. DOI: 10.1007/s11228-017-0421-z.

[38] J.-F. Cai, E. J. Candès, and Z. Shen. "A Singular Value Thresholding Algorithm for Matrix Completion". In: *SIAM Journal on Optimization* 20.4 (2010), pp. 1956–1982. DOI: 10.1137/080738970.

[39] A. Sayed. *Fundamentals of Adaptive Filtering*. Wiley, 2003. ISBN: 9780471461265.

[40] S. Gunnarsson. "Combining tracking and regularization in recursive least squares identification". In: *Proceedings of 35th IEEE Conference on Decision and Control*. Vol. 3. 1996, pp. 2551–2552. DOI: 10.1109/CDC.1996.573481.

[41] M. Al-Greer, M. Armstrong, M. Ahmeid, and D. Giaouris. "Advances on System Identification Techniques for DC–DC Switch Mode Power Converter Applications". In: *IEEE Transactions on Power Electronics* 34.7 (2019), pp. 6973–6990. DOI: 10.1109/TPEL.2018.2874997.

[42] M. Ahmeid, M. Armstrong, S. Gadoue, M. Al-Greer, and P. Missailidis. "Real-Time Parameter Estimation of DC–DC Converters Using a Self-Tuned Kalman Filter". In: *IEEE Transactions on Power Electronics* 32.7 (2017), pp. 5666–5674. DOI: 10.1109/TPEL.2016.2606417.

[43] M. Grant and S. Boyd. *CVX: Matlab Software for Disciplined Convex Programming, version 2.1*. 2014. URL: http://cvxr.com/cvx.

[44] R. H. Tan and L. Y. H. Hoo. "DC-DC converter modeling and simulation using state space approach". In: *2015 IEEE Conference on Energy Conversion (CENCON)*. 2015, pp. 42–47. DOI: 10.1109/CENCON.2015.7409511.

5

MODEL-FREE DATA-DRIVEN FAULT DIAGNOSIS FOR AIR DATA SENSORS

This chapter addresses the key question that when faults occur either the aircraft system dynamics changes due to the fault or these dynamics are unknown (precisely). This question is addressed for the important case of Air Data Sensor failures, due to e.g. icing, for fixed wing aircraft operating in a nominal flight condition. The solution to this question uses basic ideas from subspace identification to cast this problem in linear least squares problem with convex constraints (nuclear norm and 1-norm constraints). The latter are relaxations of a rank and cardinality constraint. The presented solution is validated using real-life flight test data.

5.1. Introduction

Fault Detection and Isolation (FDI) has been a key attention topic in control of high performance aircraft. See for its importance and its role in state-of-the-art in terms of fault tolerant control applicable to civil aircraft to the overview in [3]. In that book but also in many additional papers, different approaches have been presented for sensor or actuator FDI for Aerospace Systems, see e.g. [4] and the many references in it.

One crucial subset of faults in aircraft operation are faults with Air Data Sensors (ADS). These sensors make use of pitot tubes and wind vanes, mounted on the exterior of the airplane. From these measurements quantities like airspeed, angle of attack or sideslip angle are derived. These quantities provide essential information to the pilot on the state of the aircraft to safely conduct a flight [5]. Its exterior mounting make these sensors vulnerable to icing or water accumulation. These environmental effects may result in fault such as blocked pitot tubes [6]. The consequence of these faults may severely influence the information provided to the pilot, possibly even leading to catastrophic accidents. Examples are the faults in ADS in Austral Lineas Aeroeas Flight 2553 where an improper referenced airspeed led to structure failure due to exceeding the safe airspeed limits [7]. More recently the Air France 447 accident was due erroneous airspeed measurements by improper operation of the pitot probes [8]. In the period between 2003 and 2016, commercial aircraft have suffered more than 35 recorded incidents of multiple ADS faults [7].

This high relevance of FDI for ADS faults has triggered a lot of research in this area [6, 9]. Solutions have been sought in developing alternative hardware modification, such as (regular) flushing of the sensing system [9] or using redundant air data systems and majority sensor voting. Possible software extensions aim at developing virtual sensor capabilities derived from navigation sensors [10]. These virtual methods use analytical redundancy provided by mathematical models of the aircraft dynamics. In general a bottleneck in these analytical approaches is the reliance on model information of the aerodynamic forces and moments acting on the aircraft, which have to be estimated prior to the virtual sensor design methodology. That model information might be time consuming to obtain and/or may be inaccurate as a consequence of storing only a limited number of models for selected operation conditions. To overcome this shortcoming, alternative kinematic models have been proposed, such as in [11]. These kinematic models rely on the use of Inertial Measurement Units (IMU), to reconstruct the aircraft state. However that as well may suffer sensor limitations that introduce noise and biases [12].

In this chapter we take a radically new approach that aims at *simultaneous* identification of the aircraft system dynamics (in a particular operation (or trim) point) and the diagnosis of the ADS faults. For the system dynamics we assume that the aircraft dynamics in an operating point can be well described by an LTI (state space) model and for the fault diagnosis we assume the availability of a dictionary of different possible scenarios as represented by the "basis" signals in the dictionary. As in [13] such a dictionary is allowed to be too "rich" to model the (additive) fault scenario as well as does not require the magnitude of the faults to be known. Also the case of linear combinations of the "basis" signals should be allowed.

The chapter is outlined in the following way. We start in section 5.2 with a brief recap on the essential step of formulating a state space identification problem in the subspace identification framework [14]. Then we outline briefly in section 5.3 the modeling of ADS sensor faults as additive output failures with particular signatures. After that we are ready to formulate in the next section 5.4 the joint identification of the system dynamics and the diagnosis of the fault as a rank and cardinality constrained least squares problem. That problem is relaxed (convexified) by replacing these constraints resp. by a nuclear norm and a 1-norm constraint. This formulation is based on our recent contribution for "general" faults in [15]. However we now specialize this method to the isolation of ADS faults. In this formulation we are able to (automatically) deal with identifying the aircraft dynamics when flying through turbulence and we do not require the determination of the order of a state space model first, as that model is *never* explicitly identified. The goal in this chapter, for the sake of brevity, is to completely focus on the isolation of ADS faults. The validation of the new methodology in section 5.5, is demonstrated using flight test obtained models of the Cessna II Delft-NLR test aircraft operating in the longitudinal mode. On this real-life flight test data, we synthetically introduce certain fault scenarios inspired by the work in [11]. The chapter is concluded with some final remarks looking towards some future potentials.

5.2. REVIEW OF THE ESSENCE OF THE SUBSPACE PERSPECTIVE

We consider the Aircraft operating in single operation condition, possibly experiencing turbulence, to be modeled by the following Linear Time-Invariant (LTI) system:

$$
\begin{aligned}
x(k+1) &= Ax(k) + Bu(k) + w(k) \\
y(k) &= Cx(k) + v(k)
\end{aligned}
\tag{5.1}
$$

where $x(k) \in \mathbb{R}^{n_x}, u(k) \in \mathbb{R}^{n_u}, y(k) \in \mathbb{R}^{n_y}$ are resp. the state, input and output; A, B, C are the state space matrices; $w(k)$ and $v(k)$ are the process- and measurement noise. This model can therefore also accommodate the aircraft flying through turbulent media. This is an advantage over (kinematic) model based methods (such as the DMAE method [16] that was selected as benchmark reference to compare the new methodology later on in Section 5.5), as the latter requires (selective) reinitialization that does not assume process noise.

In Subspace identification we consider the *observer* form representation of the above LTI system, based on the assumption that the conditions hold for the existence of the following observer [14]:

$$
\begin{aligned}
\hat{x}(k+1) &= \underbrace{(A - KC)}_{\Phi} \hat{x}(k) + Bu(k) + Ky(k) \\
\hat{y}(k) &= C\hat{x}(k)
\end{aligned}
\tag{5.2}
$$

with $\hat{x}(k), \hat{y}(k)$ resp. the estimated state and output vectors. Using this observer form allows to write that output as:

$$
\hat{y}(k) = C\Phi^s \hat{x}(k-s) + \sum_{i=1}^{s} C\Phi^{i-1}\Big(Bu(k-i) + Ky(k-i)\Big)
\tag{5.3}
$$

If K is assumed to make Φ asymptotically stable, the effect of the (initial) state vector $\hat{x}(k-s)$ in (5.3) fades away as s increases. This is referred to as the *Subspace Trick*. This leads to the following approximate Vector Auto-Regressive model with eXogenous input (VARX):

$$\hat{y}(k) \approx \sum_{i=1}^{s} B_i u(k-i) + K_i y(k-i) \tag{5.4}$$

with matrices B_i, K_i of compatible dimensions approximating the observer Markov parameters.

5.3. MODELING ADS FAULTS

For the sake of brevity we restrict in this chapter to the modeling faults on the measurement of the aircraft's airspeed. This measurement is derived from a pitot-tube device illustrated in Figure 5.1. This device measures the total pressure at the inlet p_t and the static pressure p_s. Let p_d be the difference $p_t - p_s$, then using Bernoulli's equation (for compressible media), the True Airspeed (TAS) is given as [18]:

$$V_{TAS} = \sqrt{\frac{2\gamma}{\gamma-1} R_g T_s \left(\frac{p_d}{p_s}+1\right)^{\frac{\gamma-1}{\gamma}} - 1}, \tag{5.5}$$

where, γ is the specific heat ratio of air, R_g is the ideal gas constant and T_s is the static temperature.

   When treating anomalies (due to e.g. icing or clogging) as small deviations from the nominal values of p_t and p_s, these anomalies can be modeled as additive *faults* to the measured V_{TAS} [6]. A similar reasoning holds for the other air data sensor signals like the angle of attack α. Therefore when denoting $\begin{bmatrix} V_{TAS} \\ \alpha \end{bmatrix}$ as the output
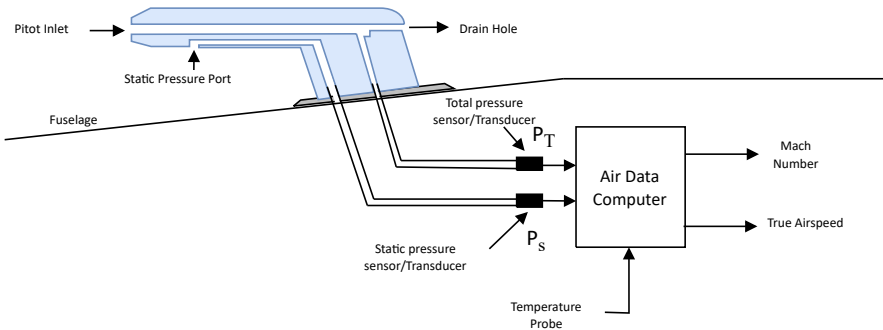

Figure 5.1: Schematic diagram of a Pitot Tube Air Data System (based on Fig. 7.1 in [17])

$y \in \mathbb{R}^2$, the measured (faulty) output is given as:

$$y_m(k) = y(k) + f(k) \tag{5.6}$$

Where these additive faults behave according to certain typical patterns as illustrated in Table 5.1 [6].

5.4. SIMULTANEOUSLY IDENTIFYING SYSTEM DYNAMICS AND FAULT DIAGNOSIS

5.4.1. PROBLEM FORMULATION

When substituting the (faulty) measurement into the VARX model (5.4) we get:

$$\hat{y}_m(k) \approx \sum_{i=1}^{s} \left(B_i u(k-i) + K_i y_m(k-i) - K_i f(k-i) \right) + f(k). \tag{5.7}$$

Making the key assumption as e.g. in [13, 15], and based on known patterns of the time evolution of the air data sensor faults, as indicated in Table 5.1, the sensor fault $f(k)$ can be modeled as:

$$f(k) = \omega(k)z, \tag{5.8}$$

where $\omega(k)$ are known signal patterns in the signal dictionary of faults. The actual fault (or fault combination) is determined by the unknown vector $z \in \mathbb{R}^{n_z}$. Based on this assumption and the VARX model representation of the output, allows to model the measured output $y_m(k)$ as:

$$
\begin{aligned}
\hat{y}_m(k) &\approx \sum_{i=1}^{s} \left(B_i u(k-i) + K_i y(k-i) - K_i f(k-i) \right) + f(k) \\
&= \sum_{i=1}^{s} \left(B_i u(k-i) + K_i y(k-i) - K_i \omega(k-i)z \right) + \omega(k)z \\
&= \sum_{i=1}^{s} \left(B_i u(k-i) + K_i y(k-i) - K_i (I_2 \otimes z^T) \text{vec}(\omega^T(k-i)) \right) \\
&\quad + \omega(k)z \\
&= \sum_{i=1}^{s} \left(B_i u(k-i) + K_i y(k-i) - M_i \text{vec}(\omega^T(k-i)) \right) + \omega(k)z
\end{aligned}
\tag{5.9}
$$

Fault	Mathematical Representation
Abrupt blockage	Bias
Gradual blockage	Drift
Partial water blockage	Sinusoidal

Table 5.1: Typical Patterns of the additive fault $f(k)$ in (5.6) to the measurement of V_{TAS} and α [6].

Now we are ready to define the rank, cardinality constrained least squares problem that is at the heart of this chapter. For that purpose, define the following quantities (assuming that we have the following input-output data $\{u(j), y_m(j)\}_{j=k}^{k+N}$ available):

$$
Y_m = \begin{bmatrix} y_m(k+s) \\ y_m(k+s+1) \\ \vdots \\ y_m(k+N) \end{bmatrix}; T_u = \begin{bmatrix} u(k+s-1) & \cdots & u(k) \\ u(k+s) & \cdots & u(k+1) \\ \vdots & \ddots & \vdots \\ u(k+N-1) & \cdots & u(k+N-s) \end{bmatrix}
$$

Like the (block-)Toeplitz matrix T_u we can define the matrices T_{y_m} and T_ω from the signals $y_m(k)$ and $\text{vec}(\omega^T(k))$. Let the products $K_i(I_2 \otimes z^T)$ be denoted as M_i and let the unknowns B_i be stored as follows:

$$
\mathbf{B} = \begin{bmatrix} B_1^T \\ B_2^T \\ \vdots \\ B_s^T \end{bmatrix}
$$

and similarly we define the matrices $\mathbf{K}, \mathbf{M}$ from the matrices K_i, M_i. Finally let the matrix Ω be defined as Y_m but now from the signal $\text{vec}(\omega^T(k))$, then we can define based on (5.9) the following constrained (linear) Least Squares problem:

$$
\min_{\mathbf{B},\mathbf{K},\mathbf{M},z} \left\| Y_m - \begin{bmatrix} T_u & T_{y_m} & -T_\omega & \Omega \end{bmatrix} \begin{bmatrix} \mathbf{B} \\ \mathbf{K} \\ \mathbf{M} \\ (I_2 \otimes z) \end{bmatrix} \right\|_F^2 \tag{5.10}
$$

subject to a cardinality (ℓ_0) constraint on the vector z and the following rank constraint:

$$
\text{rank} \begin{bmatrix} M_1 & K_1 \\ \vdots & \vdots \\ M_s & K_s \\ (I_2 \otimes z^T) & I_2 \end{bmatrix} = \text{rank}(P) = 2
$$

Using the nuclear norm (denoted as $\|.\|_\star$) and the 1-norm as convex relaxations of the above constraint, the simultaneous identification of the model dynamics and the isolation of the faults is formulated via the following convex optimization problem:

$$
\min_{\mathbf{B},\mathbf{K},\mathbf{M},z} \left\| Y_m - \begin{bmatrix} T_u & T_y & -T_\omega & \Omega \end{bmatrix} \begin{bmatrix} \mathbf{B} \\ \mathbf{K} \\ \mathbf{M} \\ (I_2 \otimes z) \end{bmatrix} \right\|_F^2 + \tau \|P\|_* + \lambda \|z\|_1 \tag{5.11}
$$

where τ, λ are hypertuning parameters. In this chapter we simply assume that the compound matrix $\begin{bmatrix} T_u & T_{y_m} & -T_\omega & \Omega \end{bmatrix}$ has full column rank. This in essence means that the joint input $\begin{bmatrix} u(k) \\ \text{vec}(\omega^T(k)) \end{bmatrix}$ is persistently exciting of at least order s, see [14].

5.4.2. A SOLUTION TO (5.11)

The convex problem (5.11) can be solved in a large number of different ways. Standard tools like cvx[1] can be readily applied. However more efficient implementations are available, like those based on proximal algorithms. For example for the optimization problem (5.11) that has three terms of which two are non-differentiable, can be handled by multiple-operator splitting schemes, such as the Parallel ProXimal Algorithm (PPXA) [19], generalized forward-backward splitting [20] or the Davis-Yin algorithm. In this chapter we use for prototyping the new idea the cvx toolbox. The new algorithmic approach based on solving (5.11) is indicated in this chapter as MF2D ("Model-Free Fault Diagnosis")

5.5. VALIDATION STUDY

5.5.1. ORGANIZATION OF THE EXPERIMENT

The newly presented data driven approach is bench-marked against the state of the art Double-Model Adaptive Estimation (DMAE) Approach for Air Data Sensor Fault detection and diagnosis presented in [16]. In this approach two Kalman filters are run in parallel: one using a fault-free model and the other a combination of the fault free model with its state augmented with the faults. The faults are modeled as random walk models and in [16] an extension is formulated to update the covariance matrices needed in the Kalman filter design.

When using (classical) sensor data for the longitudinal aircraft mode, the input (that is used by the MF2D) method) is the elevator angle (δ_e) and the output is the airdata sensor vector y_m. Use is made of real-life recorded flight test data with the Cessna II laboratory aircraft of the TU Delft and NLR. The recordings for a single flight condition that we used in this validation study are displayed in Figure 5.2.

When using this "standard" (limited) sensor data in a model based approach, like the multiple model based approach in [21], such model needs knowledge of the aerodynamic derivatives. This would make many of such model based approaches very ineffective as this would require dedicated flight testing and flight test data analysis methods for capturing these derivatives. And even then the models might never describe the actual operating conditions accurately. To overcome this major drawback the use of kinematic models was proposed in [16]. This one hand, frees the approach from requiring access to the aerodynamic derivatives, but on the other hand requires the aircraft to be equipped with (very accurate) Inertial Measurement units (IMUs). Such equipment is often present in navigation (and higher) grade IMUs where there is a redundancy in terms of triple or even quadruple sets of duplicates. Apart from the fact that even then special precaution is still needed to deal with operational bias and noise effects, the kinematic approach requires the aircraft to be *rigid*. The measurements used with kinematic models are listed in Table 5.2 (DMAE).

In the conducted experiments the data related to the flight condition from which the recorded data as in Figure 5.2 is derived, is used to simulate air-data sensors faults. As introducing such sensor faults in real-life might lead to endangering the

---

[1]http://cvxr.com/cvx

operators and aircraft, we opted for introducing these errors synthetically afterwards by adding errors to the measured data. Additive faults are introduced on the measured V_{TAS} and α as depicted in Figure 5.3 (under the label "True"). In this chapter the raw data (part of which shown in this figure) is used. This raw data was made to be recorded as a sample rate of 100 Hz. We note hereby that the air data sensor was recorded at 10 Hz, but upsampled (ZOH) to 100 Hz by the flight test instrumentation system.

5.5.2. SETTING OF THE ALGORITHMS

The DMAE kinematic model used is the one reported in [16]. This model has state dimension 6 containing $V_{\text{TAS}}, \alpha, \beta, \phi, \theta, \psi$, the input vector containing 3 accelerations A_x, A_y, A_z and angular velocities p, q, r in describing the nonlinear kinematic equations. The output vector in this case is the full state vector (plus the added faults and sensor noise).

The tuning parameters used for the DMAE algorithm are as follows:

- The process noise covariance matrix
$$Q_k = \begin{bmatrix} 10^{-4} I_3 & 0 \\ 0 & 3 \times 10^{-8} I_3 \end{bmatrix}$$

- The measurement noise covariance matrix
$$R_k = \begin{bmatrix} 10^{-2} & 0 & 0 \\ 0 & 3 \times 10^{-6} I_2 & 0 \\ 0 & 0 & 3 \times 10^{-8} I_3 \end{bmatrix}$$

- The initial state covariance matrix of the nominal (fault-free = ff) model $P_{x_0, ff} = I_6$

- The initial state covariance matrix of the augmented fault (=af) model $P_{x_0, af} = I_8$

- $N_Q = 40$ (width of moving window)

For the new algorithm MF2D the following settings have been used:

- $s = 4$

- $\tau = \lambda = 0.1$

- $\omega(k) \in \mathbb{R}^{2 \times 80}$ consisting of unit steps with 40 possible starting times for f_V, plus 40 possible starting times for f_α (evenly distributed).

- I/O data is detrended by subtracting the sample means.

- The two sensor outputs in y are normalized such that both outputs have a variance of 1.

5.5.3. Results

For the sake of brevity we focus only on the estimation of the additive faults. These are for both methods displayed in Figure 5.3. From this figure it is clearly observed that the new method MF2D outperforms the DMAE approach. The latter furthermore makes use of a much more elaborate sensors infrastructure (which are themselves prone to errors that need continuous calibration) and needs careful adaptation of the Kalman filter parameters, such as a careful reinitialization [16]. This especially for flying through turbulence might not be trivial. The performance of the DMAE approach is tested using the code available on github[2], with no efforts to finetune the defaults given. Figure 5.3 shows that this implementation is indeed able to *detect* that there is a fault in the ADS, but is not able to precisely *diagnose* the magnitude and the particular part of the ADS sensor failing.

On the other hand the new MF2D captured both faults very accurately in onset and shape. The magnitude is however not captured fully accurately due to the use of 1-norm as a convex relaxation of the 0-norm. This can however easily be improved by a re-estimation of that magnitude as outlined in [22]. In that re-estimating the support and shape of the fault is then used as pictured in Figure 5.3. One challenging element for the new MF2D is the design of the dictionary ω. However prior testing might provide useful information here, and the consideration of the cardinality (or 1-norm) constraint as in the current experiment enabled to correctly and accurate estimate faults that were not in the dictionary!

Table 5.2: Required sensors for the two approaches

	DMAE	MF2D	Description
V_{TAS}	✓	✓	true airspeed, m/s
α	✓	✓	angle of attack, rad
δ_e		✓	elevator deflection, rad
β	✓		sideslip angle, rad
p, q, r	✓		roll, pitch & yaw rates, rad/s
ϕ, θ, ψ	✓		roll, pitch & yaw angles, rad
A_x, A_y, A_z	✓		linear accelerations, m/s^2

5.6. Conclusion

This chapter has presented a new method to *simultaneously* identify the (LTI) system dynamics and additive faults on the Air Data Sensors for civil aircraft. The new methods, indicated as the MF2D (Model-Free Fault Diagnosis) extends basic ideas of subspace identification and models the fault via basis (time-)functions in a dictionary. The MF2D is presented here via convex relaxation as convex optimization problem. This can efficiently and reliably be solved. Its comparison with the state-of-the-art solution based on multiple Kalman filters that avoids accurate

---

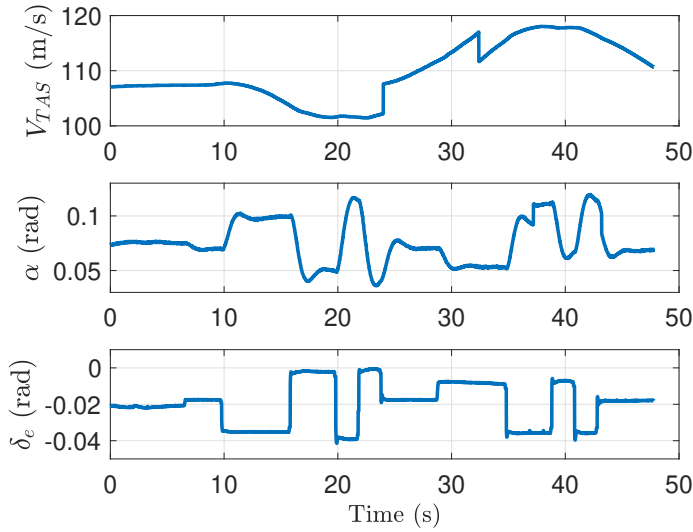[2]https:github.com/lplp8899/ADS_FDD_Turbulence

Figure 5.2: The flight data utilized in the MF2D approach: true airspeed V_{TAS} (top), angle of attack α (middle) and elevator deflection δ_e (bottom).
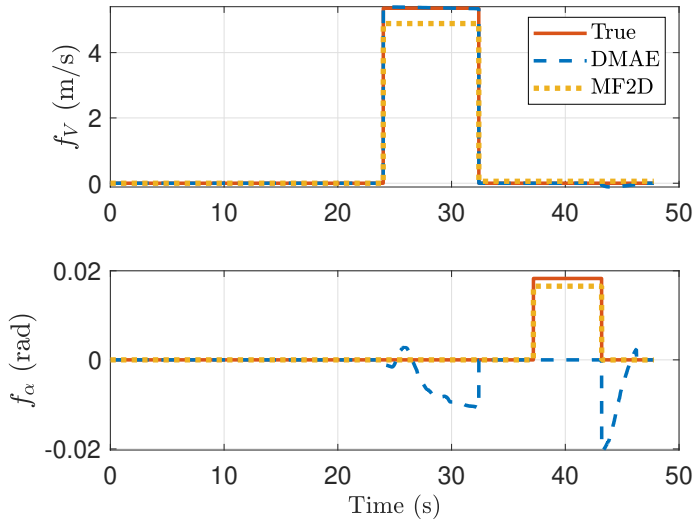

Figure 5.3: The faults f_V and f_α introduced in V_{TAS} and α, respectively: true faults (red, solid), estimation using the extended DMAE-approach (blue, dashed), and estimation using the MF2D approach (yellow, dotted).

knowledge of model information through the aerodynamic derivatives, as presented in [16] demonstrated the superiority of the newly developed methodology. This comparison makes use of real-life flight test data with the Cessna Citation II aircraft.

Though this comparison is preliminary, it shows the great potential of the new MF2D approach. It makes use of a minimal set of sensor devices that are standardly available on aircraft (and drones), it is able to deal with these flying objects flying through turbulence as well as laminar flow and can also deal with non-rigid flying devices. The difference in sensor configuration is highlighted for the current study in Table 5.2.

These encouraging results leave plenty of room for future extensions and validations of this approach. One is the design of the dictionary and making that dictionary adaptive by letting the basis functions move in a moving window. Also making the whole approach adaptive would enable extension to different flight conditions.

5

REFERENCES

[1] J. Noom, C. C. de Visser, N. S. Ramesh, and M. Verhaegen. "Simultaneously identifying the system dynamics and fault isolation for air data sensor failures: a convex approach". Accepted for presentation at IFAC Safe Process 2024.

[2] J. Noom. *Matlab code for simultaneous identification of the system dynamics and fault isolation for air data sensor failures*. 2024. DOI: 10.5281/zenodo.10454343.

[3] C. Edwards, T. Lombaerts, H. Smaili, M. Morari, and M. Thoma, eds. *Fault Tolerant Flight Control: A Benchmark Challenge*. Vol. 399. Lecture Notes in Control and Information Sciences. Berlin, Heidelberg: Springer, 2010. DOI: 10.1007/978-3-642-11690-2.

[4] J. Marzat, H. Piet-Lahanier, F. Damongeot, and E. Walter. "Model-based fault diagnosis for aerospace systems: a survey". In: *Proceedings of the Institution of Mechanical Engineers, Part G: Journal of Aerospace Engineering* 226.10 (Oct. 2012). Publisher: IMECHE, pp. 1329–1360. DOI: 10.1177/0954410011421717.

[5] D. Houck and L. Atlas. "Air data sensor failure detection". In: *17th DASC. AIAA/IEEE/SAE. Digital Avionics Systems Conference. Proceedings (Cat. No.98CH36267)*. 1998, pp. D17/1–D17/8. DOI: 10.1109/DASC.1998.741508.

[6] P. Freeman, P. Seiler, and G. J. Balas. "Air data system fault modeling and detection". In: *Control Engineering Practice* 21.10 (2013), pp. 1290–1301. DOI: 10.1016/j.conengprac.2013.05.007.

[7] R. Eubank, E. Atkins, and S. Ogura. "Fault Detection and Fail-Safe Operation with a Multiple-Redundancy Air-Data System". In: *AIAA Guidance, Navigation, and Control Conference*. Guidance, Navigation, and Control and Co-located Conferences. American Institute of Aeronautics and Astronautics, 2010. DOI: 10.2514/6.2010-7855.

[8] F. Balzano, M. L. Fravolini, M. R. Napolitano, S. d'Urso, M. Crispoltoni, and G. del Core. "Air Data Sensor Fault Detection with an Augmented Floating Limiter". In: *International Journal of Aerospace Engineering* 2018 (2018). Publisher: Hindawi, e1072056. DOI: 10.1155/2018/1072056.

[9] J. Ellsworth and S. Whitmore. "Reentry Air Data for a Sub-orbital Spacecraft Based on X-34 Design". In: *45th AIAA Aerospace Sciences Meeting and Exhibit*. Aerospace Sciences Meetings. American Institute of Aeronautics and Astronautics, 2007. DOI: 10.2514/6.2007-1200.

[10] G. Looye and H.-D. Joos. "Design of robust dynamic inversion control laws using multi-objective optimization". In: *AIAA Guidance, Navigation, and Control Conference and Exhibit*. Guidance, Navigation, and Control and Co-located Conferences. American Institute of Aeronautics and Astronautics, 2001. DOI: 10.2514/6.2001-4285.

[11] P. Lu, L. V. Eykeren, E. van Kampen, C. de Visser, and Q. Chu. "Adaptive Three-Step Kalman Filter for Air Data Sensor Fault Detection and Diagnosis". In: *J. of Guidance, Control and Dynamics* 39.3 (2016), pp. 590–604. DOI: 10.2514/1.G001313.

[12] M. A. Van Den Hoek, C. C. De Visser, and D. M. Pool. "Identification of a Cessna Citation II Model Based on Flight Test Data". In: *Advances in Aerospace Guidance, Navigation and Control*. Ed. by B. Dolega, R. Glebocki, D. Kordos, and M. Zugaj. Cham: Springer International Publishing, 2018, pp. 259–277. DOI: 10.1007/978-3-319-65283-2_14.

[13] Q. Zhang. "Dynamic System Fault Diagnosis Under Sparseness Assumption". In: *IEEE Transactions on Signal Processing* 69 (2021), pp. 2499–2508. DOI: 10.1109/TSP.2021.3072004.

[14] M. Verhaegen and V. Verdult. *Filtering and System Identification: A Least Squares Approach*. Cambridge: Cambridge University Press, 2007. ISBN: 978-1107405028.

[15] J. Noom, O. Soloviev, and M. Verhaegen. "Data-driven fault diagnosis under sparseness assumption for LTI systems". In: *IFAC-PapersOnLine* 56.2 (2023), pp. 7722–7727. DOI: 10.1016/j.ifacol.2023.10.1176.

[16] P. Lu, E.-J. van Kampen, C. de Visser, and Q. Chu. "Air Data Sensor Fault Detection and Diagnosis in the Presence of Atmospheric Turbulence: Theory and Experimental Validation With Real Flight Data". In: *IEEE Transactions on Control Systems Technology* 29.5 (2021), pp. 2255–2263. DOI: 10.1109/TCST.2020.3025725.

[17] R. Collinson. *Introduction to Avionics Systems*. Springer Netherlands, 2011. DOI: 10.1007/978-94-007-0708-5.

[18] H. Hu, F. Al-Masri, and H. Hu. "An Experimental Study on Ice Accretion and Anti-/De-Icing of a Pitot Tube". In: *AIAA SCITECH 2022 Forum*. American Institute of Aeronautics and Astronautics, 2022. DOI: 10.2514/6.2022-1913.

[19] P. L. Combettes and J.-C. Pesquet. "A proximal decomposition method for solving convex variational inverse problems*". In: *Inverse Problems* 24.6 (2008), p. 065014. DOI: 10.1088/0266-5611/24/6/065014.

[20] H. Raguet, J. Fadili, and G. Peyré. "A Generalized Forward-Backward Splitting". In: *SIAM Journal on Imaging Sciences* 6.3 (2013), pp. 1199–1226. DOI: 10.1137/120872802.

[21] R. Hallouzi, M. Verhaegen, and S. Kanev. "Multiple model estimation: A convex model formulation". In: *International Journal of Adaptive Control and Signal Processing* 23.3 (2009), pp. 217–240. DOI: 10.1002/acs.1034.

[22]   J. Noom, O. Soloviev, and M. Verhaegen. "Proximal-based recursive implementation for model-free data-driven fault diagnosis". Accepted for publication in Automatica.

5

6

CONCLUSIONS

As outcome of this dissertation, convex optimization has shown its relevance to fault diagnosis in order to develop novel approaches with low computational requirements. This chapter summarizes the main findings in this dissertation and provides directions for future research, both for the field of fault diagnosis and data-driven control.

This dissertation aimed at developing novel approaches to fault diagnosis of which the computational requirements remained low. In order to achieve this objective, the applicability of convex optimization was investigated in a variety of both state-of-the-art and newly presented concepts for fault diagnosis. The conclusions for each contribution can be summarized as follows.

Chapter 2 focused on online design of auxiliary inputs in order to improve the discrimination performance. The online input design problem faced a trade-off between three factors, namely a high accuracy of diagnosis, a small required number of consecutive measurements for diagnosis, and low computational effort. Due to the use of the Bhattacharyya coefficient as divergence measure and its favorable properties in challenging discrimination conditions, the computational effort remained low. Furthermore, the use of the Bhattacharyya coefficient preserved an analytical upper bound on the error probability, such that a high diagnosis performance was maintained. The optimal auxiliary input with respect to the upper bound was determined iteratively using convex optimization programs. It was shown that a quadratic Taylor approximation of the upper bound further sped up the computations without considerably sacrificing the other trade-off factors.

Chapter 3 applied a sparse estimation method to high-speed atomic force microscopy for diagnosing large numbers of tip-sample interactions, considered as faults. The problem was written in a convex 'lasso' form so that is could be solved with an efficient solver. After optimization, the diagnosed faults were employed to recover the sample height. In comparison with the conventional approach for high-speed atomic force microscopy, the proposed approach recovered the sample height at high scan speeds with higher accuracy.

Chapter 4 introduced a new problem formulation for simultaneously identifying the system and diagnosing the faults. Solutions to the so-called problem of model-free data-driven fault diagnosis should circumvent the requirement of large amounts of historical data usually required in state-of-the-art data-driven fault diagnosis. A proposed solution reformulated it as a convex optimization problem. Online evaluation was facilitated by a recursive implementation of a proximal algorithm.

Chapter 5 presented a solution to the model-free data-driven fault diagnosis problem for diagnosing air data sensor faults. Similarly to the solution proposed in Chapter 4, it resulted in a convex optimization problem with a least-squares term, a nuclear norm and a 1-norm. The methodology was demonstrated on real-life flight test data. Compared to a state-of-the-art method for diagnosis of air data sensor faults, the proposed solution required fewer (delicately calibrated and denoised) sensors, while still being able to diagnose the active faults.

6.1. Recommendations

Based on the research presented in this thesis on the application of convex optimization to fault diagnosis, future research is recommended to study on the following aspects.

Evaluation of the exact error probability for online input design   Due to the use of an analytical upper bound on the error probability, the method proposed in Chapter 2 performs better than state-of-the-art methods. The diagnosis performance can be even

further improved if the actual error probability is minimized rather than its upper bound. With the current state of developments, this however imposes a burden on the computational requirements. A way to alleviate these requirements is to use the method for minimizing the upper bound proposed in Chapter 2 for initializing the nonlinear minimization of the actual error probability. The implementation of this solution together with its possible implications is left open for further research.

Real-time estimation of tip-sample interaction in high-speed AFM   The method proposed in Chapter 3 is able to diagnose large numbers of tip-sample interactions as faults. Even though the proposed method is computationally efficient due to the use of the convex 'lasso' form and an efficient corresponding solver, it is only applied *a posteriori*. That is to say the data is first acquired before it is analyzed for diagnosing the faults, which requires the data to be of sufficient quality. High-speed AFM however also bears real-time control challenges for assuring this data quality. For instance, the well-known problem (in the AFM community) of parachuting remains to be challenging. The estimation of tip-sample interaction in real-time could help to rapidly detect loss of intermittent tip-sample interaction, such that appropriate control action can be taken. Such real-time implementation of the proposed method in Chapter 3 is not realized yet. One of the reasons for this is the typical high sampling rate required for high-speed AFM, regarding the contemporary cantilever oscillation frequencies of hundreds of kilohertz, imposing high required sampling rates and therefore short periods for real-time processing. Future research should focus on implementing the method in Chapter 3 recursively using a proximal algorithm. This could for instance be realized using the recursive implementation of a proximal algorithm presented in Chapter 4.

Construction of the dictionary for model-free fault diagnosis   The proposed approaches for model-free fault diagnosis in Chapters 4 and 5 utilize a dictionary in order to represent shapes of possible faults in the system. Chapter 4 provides a condition on the dictionary signals which must be satisfied in order to allow diagnosis of the faults. Compliance with this condition is however not a *guarantee* for diagnosability. The challenging problem of finding a *sufficient* condition for diagnosability is left open for future research. The study of a sufficient condition for diagnosability goes well with theoretical research on the diagnosis performance with respect to the I/O-data properties and on the evaluation of the uncertainty of the estimated system parameters and faults.

Data-driven control in the presence of disturbances   A currently trending research topic in the field of control science is on data-driven control (e.g. [1–4]). These techniques aim for designing a control law directly from past I/O-data, rather than explicitly identifying a system prior to designing the control law. With the methods presented in Chapters 4 and 5 the state-of-the-art of data-driven control can be complemented with disturbance rejection. For instance, if one of the methods in Chapter 4 or 5 diagnoses a periodic fault, then its effect can be suppressed in a predictive control law to be applied directly after the simultaneous system identification and fault diagnosis. Furthermore, the recursive formulation presented in Chapter 4 allows to update the (disturbance rejecting) control law in real-time after every measurement. This is particularly relevant for critical systems in unforeseen severe situations, such as breakage of aircraft components during flight. Whereas aircraft in such situations may not be modeled sufficiently, the model-free data-driven approaches in Chapters 4 and 5 may be able to identify the

6

altered dynamics and diagnose the faults, so that the control law is updated accordingly.

Recursive blind deconvolution of real-time image sequences   In Chapters 4 and 5 we used a so-called lifting technique to rewrite a bilinear least-squares problem to a rank-constrained least-squares problem. The rank constraint was then relaxed to an additional nuclear norm to the optimization problem. This concept for relaxation of bilinear problems has far-reaching applications beyond model-free fault diagnosis. One of these applications is blind multi-frame deconvolution of images, such as in [5]. The objective of blind multi-frame deconvolution is to recover both the object and the point spread functions of multiple images of the object from the same viewpoint, in order to obtain a high resolution reconstruction of the object. The application of the lifting technique to blind deconvolution has been presented for small images in [6]. With the recursive implementation of a proximal algorithm presented in Chapter 4, it may however be possible to blindly deconvolve larger images with acceptable computational effort and to process these images in real-time while they are being recorded sequentially.

Interpretability of data-driven control methodologies   From a broader perspective, two routes can be followed in the future. The first route improves the performance of black-box algorithms for data-driven control. A good performance however is not the only factor for algorithms to be *reliable*. There also needs to be some user's understanding of *how* the algorithms come to their results and how confident these are. The second possible route is therefore to further develop the interpretability of data-driven control methodologies. A first step to realize this for the methodologies in Chapters 4 and 5 can be to provide uncertainties to the estimated quantities. A good interpretability of the algorithms is crucial for the user to utilize these and to make well-informed decisions based on the outcomes.

6

REFERENCES

[1] F. Dörfler, J. Coulson, and I. Markovsky. "Bridging Direct and Indirect Data-Driven Control Formulations via Regularizations and Relaxations". In: *IEEE Transactions on Automatic Control* 68.2 (2023), pp. 883–897. DOI: 10.1109/TAC.2022.3148374.

[2] R. Dinkla, S. P. Mulders, J.-W. van Wingerden, and T. Oomen. "Closed-loop aspects of data-enabled predictive control". In: *IFAC-PapersOnLine* 56.2 (2023), pp. 1388–1393. ISSN: 2405-8963. DOI: 10.1016/j.ifacol.2023.10.1806.

[3] J.-W. van Wingerden, S. P. Mulders, R. Dinkla, T. Oomen, and M. Verhaegen. "Data-enabled predictive control with instrumental variables: the direct equivalence with subspace predictive control". In: *2022 IEEE 61st Conference on Decision and Control (CDC)*. 2022, pp. 2111–2116. DOI: 10.1109/CDC51059.2022.9992824.

[4] H. J. van Waarde, J. Eising, H. L. Trentelman, and M. K. Camlibel. "Data Informativity: A New Perspective on Data-Driven Analysis and Control". In: *IEEE Transactions on Automatic Control* 65.11 (2020), pp. 4753–4768. DOI: 10.1109/TAC.2020.2966717.

[5] D. Wilding, O. Soloviev, P. Pozzi, G. Vdovin, and M. Verhaegen. "Blind multi-frame deconvolution by tangential iterative projections (TIP)". In: *Opt. Express* 25.26 (Dec. 2017), pp. 32305–32322. DOI: 10.1364/OE.25.032305.

[6] C. Cheng and W. Dai. "Short-and-Sparse Deconvolution Via Rank-One Constrained Optimization (Roco)". In: *ICASSP 2022 - 2022 IEEE International Conference on Acoustics, Speech and Signal Processing (ICASSP)*. 2022, pp. 5882–5886. DOI: 10.1109/ICASSP43922.2022.9747176.

CURRICULUM VITÆ

Jacques NOOM

1996	Born in Beverwijk, The Netherlands
2014–2017	BSc Mechanical Engineering Delft University of Technology, The Netherlands
2017–2019	MSc Systems & Control Delft University of Technology, The Netherlands
2019–2024	PhD Systems & Control Delft University of Technology, The Netherlands

Thesis: Input design and data-driven approaches based on convex optimization for fault diagnosis in linear systems

Promotors: Dr. O. Soloviev
Dr. C.S. Smith
Prof.dr.ir. M. Verhaegen

LIST OF PUBLICATIONS

10. **J. Noom**, C. C. de Visser, N. S. Ramesh, and M. Verhaegen. "Simultaneously identifying the system dynamics and fault isolation for air data sensor failures: a convex approach". Accepted for presentation at IFAC Safe Process 2024.

9. **J. Noom**, O. Soloviev, and M. Verhaegen. "Proximal-based recursive implementation for model-free data-driven fault diagnosis". Accepted for publication in Automatica.

8. **J. Noom**, O. Soloviev, C. Smith, and M. Verhaegen. *Online input design for discrimination of linear models using concave minimization*. 2024. arXiv: 2401.05782 [eess.SY]

7. **J. Noom**, O. Soloviev, and M. Verhaegen. "Data-driven fault diagnosis under sparseness assumption for LTI systems". In: *IFAC-PapersOnLine* 56.2 (2023), pp. 7722–7727. DOI: 10.1016/j.ifacol.2023.10.1176

6. **J. Noom**, C. Smith, G. J. Verbiest, A. J. Katan, O. Soloviev, and M. Verhaegen. "High-Speed Tapping Mode AFM Utilizing Recovery of Tip-Sample Interaction". In: *IEEE Transactions on Nanotechnology* 22 (2023), pp. 273–279. DOI: 10.1109/TNANO.2023.3284654

5. **J. Noom**, O. Soloviev, C. Smith, and M. Verhaegen. "Closed-loop active object recognition with constrained illumination power". In: *Real-Time Image Processing and Deep Learning 2022*. Ed. by N. Kehtarnavaz and M. F. Carlsohn. Vol. 12102. International Society for Optics and Photonics. SPIE, 2022, pp. 9–14. DOI: 10.1117/12.2618750

4. O. Soloviev, H. T. Nguyen, **J. Noom**, and M. Verhaegen. "Increase of wafer inspection tool throughput with computational imaging". In: *Dimensional Optical Metrology and Inspection for Practical Applications XI*. ed. by K. G. Harding, S. Zhang, J.-S. Hyun, and B. Li. Vol. 12098. International Society for Optics and Photonics. SPIE, 2022, 120980G. DOI: 10.1117/12.2618736

3. **J. Noom**, O. Soloviev, C. Smith, H. T. Nguyen, and M. Verhaegen. "Particle detection using closed-loop active model diagnosis". In: *AI and Optical Data Sciences III*. ed. by B. Jalali and K.-i. Kitayama. Vol. 12019. International Society for Optics and Photonics. SPIE, 2022, 120190F. DOI: 10.1117/12.2605452

2. O. Soloviev, **J. Noom**, H. T. Nguyen, G. Vdovin, and M. Verhaegen. "Phase retrieval from overexposed PSF: a projection-based approach". In: *Quantitative Phase Imaging VIII*. ed. by Y. Liu, G. Popescu, and Y. Park. Vol. 11970. International Society for Optics and Photonics. SPIE, 2022, 119700K. DOI: 10.1117/12.2609697

1. **J. Noom**, N. H. Thao, O. Soloviev, and M. Verhaegen. "Closed-Loop Active Model Diagnosis Using Bhattacharyya Coefficient: Application to Automated Visual Inspection". In: *Intelligent Systems Design and Applications (ISDA 2020)*. Ed. by A. Abraham, V. Piuri, N. Gandhi, P. Siarry, A. Kaklauskas, and A. Madureira. Springer, Cham, 2021, pp. 657–667. DOI: 10.1007/978-3-030-71187-0_60